

AD-A119 947

MISSION RESEARCH CORP SANTA BARBARA CA

F/G 4/1

A MODEL FOR GRAVITY WAVES PRODUCED BY LOW ALTITUDE EXPLOSIONS F--ETC (U)

SEP 81 & D MCCARTON, W R WORTHMAN, W R FROLLI

DNA001-A1-C-0022

UNCLASSIFIED

MRC-R-659

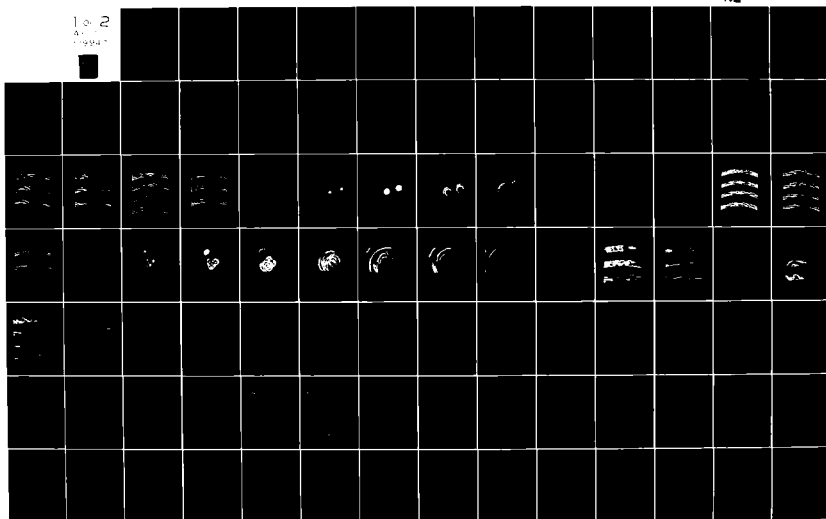
DNA-58857

NL

1-2

81

1994



AD-E 301 041

(12)

DNA 5885T

A MODEL FOR GRAVITY WAVES PRODUCED BY LOW ALTITUDE EXPLOSIONS FOR USE IN COMMUNICATIONS STUDIES

G. D. McCartor

W. R. Wortman

M. R. Frolli

Mission Research Corporation

P.O. Drawer 719

Santa Barbara, California 93102

1 September 1981

Topical Report for Period 1 May 1981-30 August 1981

CONTRACT No. DNA 001-80-C-0022

APPROVED FOR PUBLIC RELEASE;
DISTRIBUTION UNLIMITED.

THIS WORK SPONSORED BY THE DEFENSE NUCLEAR AGENCY
UNDER RDT&E RMSS CODE B322080464 S99QAXHB05312 H2590D.

Prepared for

Director

DEFENSE NUCLEAR AGENCY

Washington, D. C. 20305

DTIC
ELECTRONIC

OCT 0 6 1982

E

3 1 10 008

AD A119947

DTIC FILE COPY

Destroy this report when it is no longer
needed. Do not return to sender.

PLEASE NOTIFY THE DEFENSE NUCLEAR AGENCY,
ATTN: STTI, WASHINGTON, D.C. 20305, IF
YOUR ADDRESS IS INCORRECT, IF YOU WISH TO
BE DELETED FROM THE DISTRIBUTION LIST, OR
IF THE ADDRESSEE IS NO LONGER EMPLOYED BY
YOUR ORGANIZATION.



UNCLASSIFIED

SECURITY CLASSIFICATION OF THIS PAGE (When Data Entered)

REPORT DOCUMENTATION PAGE		READ INSTRUCTIONS BEFORE COMPLETING FORM
1. REPORT NUMBER DNA 5885T	2. GOVT ACCESSION NO. AD-2112-005	3. RECIPIENT'S CATALOG NUMBER
4. TITLE (and Subtitle) A MODEL FOR GRAVITY WAVES PRODUCED BY LOW ALTITUDE EXPLOSIONS FOR USE IN COMMUNICATIONS STUDIES		5. TYPE OF REPORT & PERIOD COVERED Topical Report for Period 1 May 81-30 Aug 81
		6. PERFORMING ORG. REPORT NUMBER MRC-R-659
7. AUTHOR(s) G. D. McCartor W. W. Wortman M. R. Frolli		8. CONTRACT OR GRANT NUMBER(s) DNA 001-81-C-0022
9. PERFORMING ORGANIZATION NAME AND ADDRESS Mission Research Corporation P.O. Drawer 719 Santa Barbara, California 93102		10. PROGRAM ELEMENT, PROJECT, TASK AREA & WORK UNIT NUMBERS Subtask S99QAXHB053-12
11. CONTROLLING OFFICE NAME AND ADDRESS Director Defense Nuclear Agency Washington, D.C. 20305		12. REPORT DATE 1 September 1981
		13. NUMBER OF PAGES 124
14. MONITORING AGENCY NAME & ADDRESS (if different from Controlling Office)		15. SECURITY CLASS (of this report) UNCLASSIFIED
		15a. DECLASSIFICATION DOWNGRADING SCHEDULE N/A since Unclassified
16. DISTRIBUTION STATEMENT (of this Report) Approved for public release; distribution unlimited.		
17. DISTRIBUTION STATEMENT (of the abstract entered in Block 20, if different from Report)		
18. SUPPLEMENTARY NOTES This work sponsored by the Defense Nuclear Agency under RDT&E RMSS Code B322080464 S99QAXHB05312 H2590D.		
19. KEY WORDS (Continue on reverse side if necessary and identify by block number) HF Gravity Wave Nuclear Explosion Ionosphere		
20. ABSTRACT (Continue on reverse side if necessary and identify by block number) A model of the ionospheric gravity wave produced by a low altitude explosion has been developed and installed in a ray trace computer code.		

DD FORM 1473
1 JAN 73

EDITION OF 1 NOV 65 IS OBSOLETE

UNCLASSIFIED

SECURITY CLASSIFICATION OF THIS PAGE (When Data Entered)

TABLE OF CONTENTS

LIST OF ILLUSTRATIONS	2
SECTION	
1 INTRODUCTION	3
2 THE MODEL FOR RANGES GREATER THAN 600 KILOMETERS	5
Introduction	5
General Features of AGW	5
The Model	7
3 THE MODEL FOR RANGES LESS THAN 600 KILOMETERS	13
4 EXAMPLES	23
5 CONCLUSIONS	60
REFERENCES	61
APPENDIX A - SHOCK WAVE IN THE ATMOSPHERE	A-1
APPENDIX B - THE CALCULATION OF LINEAR DISTURBANCES IN AN ISOTHERMAL ATMOSPHERE	B-1



Accession For	
NTIS GRA&I	<input checked="" type="checkbox"/>
DTIC TAB	<input type="checkbox"/>
Unannounced	<input type="checkbox"/>
Justification	
By	
Distribution/	
Availability Codes	
Dist	Avail and/or Special
A	

LIST OF ILLUSTRATIONS

<u>FIGURE</u>		<u>PAGE</u>
1	Burst geometry.	8
2	$\delta p/p_0$ as a function of time 300 km directly above a 1 MT explosion.	16
3	A comparison between the altitude dependence of the model and the CINT results.	20
4a	Contours of electron density in an artificial ionosphere along a north-south line following a 1 MT nuclear explosion at sea level.	24
4b	Contours of electron density in an artificial ionosphere (see text) along an east-west line.	26
5	Contours of electron density at 250 km altitude following two 10 MT explosions.	29
6	Contours of electron density for the event of Figure 5 along the line shown in Figure 5.	36
7	An HF link from Omaha, Nebraska to British Columbia and the location of explosions of 100 MT and 30 MT.	39
8	Contours of electron density (artificial ionosphere) at 250 km altitude following the attack.	40
9	Contours of electron density along the link (for the artificial ionosphere) following the attack.	48
10	Contours of critical frequency (realistic ionosphere) along the link following the attack.	51
11a	The landing points for a bundle of 25 MHz rays launched at about 2.70° elevation 60 minutes after the attack.	55
11b	The landing points for a bundle of 25 MHz rays launched at about 7.93° elevation angle 60 minutes after the attack.	56
11c	The landing points for the 2.70° ray bundle for the ambient atmosphere.	57
12	The range to which rays launched at elevation angle θ propagate for 15 MHz, two hops, for the 240 minute environment.	59

SECTION 1

INTRODUCTION

After the detonation of a low altitude nuclear weapon a strong blast wave moves out from the explosion, eventually (for all the weapons so far detonated) becoming weak and propagating as an acoustic pulse. As the pulse propagates into the decreasing density of the upper atmosphere the pulse strengthens (in terms of the relative overpressure) and forms a shock (more or less strong according to the weapon yield) which propagates through the ionosphere. After the passage of the strong pulse the atmosphere and ionosphere are left in motion, bobbing up and down due to the interaction of gravity with the stratified density of the atmosphere.

At distances of thousands of kilometers from a large, low altitude explosion, the ionosphere has been observed to be set in motion. This motion is universally attributed to some type of internal gravity wave. These ionospheric motions can be expected to produce substantial modifications to the propagation of HF radio waves which reflect off the ionosphere. In this report we describe a model for the ionospheric motions which has been programmed into a ray tracing computer code which will, in the future, be used to analyze implications of gravity wave phenomena for HF military systems.

For distances far from the burst we do not know, in detail, what mechanisms produce the gravity wave and cannot do a first principles calculation of the gravity wave effects. For this region we must rely on data combined with general theoretical knowledge of the properties of gravity waves to construct the model. The model created for distances from the burst greater than 600 km is described in Chapter 2.

For distances closer to the burst we believe that our understanding of the important phenomena is more complete and we can perform calculations of the effects to be expected. In Chapter 3 we describe the procedures by which we make these calculations and give the results. In this chapter we also describe a model which agrees reasonably well with both the long distance model and the results of the calculations for points closer in. This is the model we have put into the ray trace code.

In Chapter 4 we give the results of several examples using the model. We first give only the ionospheric disturbance calculated by the model for an increasingly complicated set of inputs. Then we show the results of tracing rays through the convoluted ionospheres given by the model. These calculations are not intended to analyze the systems implications of the gravity waves but are intended as a preliminary demonstration that the model works as expected. We hope to soon be able to use these tools to perform studies in sufficient detail to make statements about the systems implications.

SECTION 2

THE MODEL FOR RANGES GREATER THAN 600 KILOMETERS

INTRODUCTION

The linear response of the atmosphere to mild disturbances can be given in terms of acoustic gravity waves (AGW). Although the disturbance in the region of a nuclear burst is far from mild, once the disturbance propagates to large distances its amplitude will diminish and thus become describable in terms of AGW.

The general procedure for application of AGW theory requires that the source be decomposed onto all possible modes, both discrete and continuous. The time progression of the system is then obtained by advancing the time in the Fourier factor for the individual modes followed by a summation over the modes. This procedure can be reduced to simple terms in the event that a single AGW mode describes the disturbance adequately. We will use such simplifications. The approximations used in modeling ionospheric effects of AGW are based on both theoretical and experimental observations.

GENERAL FEATURES OF AGW

In terms of the problem at hand, that of effects on the distant ionosphere due to low-altitude bursts, there is a set of theoretical features of AGW which is useful to consider. Some of these are:

1. The atmosphere supports both freely propagating (continuous spectrum) and ducted (discrete spectrum) modes.¹ Both may

propagate to great distances but the ducted modes have their energy concentrated at altitudes above 50 km.

2. Long period, freely propagating gravity modes dominate the distant disturbances launched from low altitude sources.² These modes give a fairly constant period fluctuation at a fixed range.
3. The long period waves tend to bend around the earth's surface.³
4. The particle motion associated with long period modes tends to be nearly horizontal.
5. The intensity of the AGW disturbances changes with altitude. It tends to grow exponentially with altitude up to ~300 km (due to exponential decrease in density) and then decreases above 300 km due to viscous dissipation.
6. The ionospheric plasma driven by atmospheric motion is largely confined to motion along the magnetic field lines. There have been two large yield bursts which have produced significant ionospheric disturbances, the Pacific test Housatonic,⁴ and the USSR Novaya Zemlya test of 30 October 1961. For these events, several features were consistently seen by ionosonde observations:
 - a. The disturbance showed a nearly sinusoidal variation with one or two cycles.
 - b. These variations showed a nearly constant period for individual stations which increased with increasing distances from the burst.
 - c. The onset time for the disturbances was approximately $(\text{range})/(\text{sound speed})$ where the sound speed is that in the region of the ionosphere.

- d. The amplitude of the disturbances did not decrease with distance in any obvious manner.
- e. The initial motion of the ionosphere (up or down) seemed to be fixed by the magnetic field orientation.

THE MODEL

In order to form a simple model of distant ionospheric disturbances we first note that for sinusoidal variation in the velocity implied by a single mode, the continuity condition is given by

$$\frac{D}{Dt} (\ln N) = - \nabla \cdot \vec{V} \sim V/\lambda \quad (1)$$

so

$$\ln (N/N_0) \sim V/\lambda\omega \quad (2)$$

where N is the electron density and N_0 the unperturbed electron density. The position will be

$$\vec{X} - \vec{X}_0 = \int \vec{V} dt \sim V/\omega \quad (3)$$

where λ is a wavelength and ω the frequency. Therefore one expects the position and $\ln(N/N_0)$ to vary in a related way.

Due to the nearly horizontal stratification of the ambient ionosphere, chiefly the vertical (Z) motion will be detectable. Therefore given the magnetic field dip angle θ , and the azimuthal propagation angle ϕ , measured from magnetic north, purely horizontal (X) neutral motion will lend to a plasma velocity of

$$V_z^p = V \sin(2\theta) \cos(\phi)/2 \quad (4)$$

The compression implied by $\nabla \cdot \mathbf{V}$, again confining the plasma to motion along the field line, gives

$$\nabla \cdot \mathbf{V}^P = V \sin(2\theta) \cos(\phi) / 2\lambda_z \quad . \quad (5)$$

Here $\lambda_z \ll \lambda_x$ has been used. This is consistent with the properties of long-period gravity waves.

The period of distant, freely propagating gravity waves is

$$\tau_C \approx \tau_B / \tan(\alpha) \quad (6)$$

where τ_B is the Brunt period and α the takeoff angle in Figure 1. Thus, for small angles α ,

$$\tau_C \approx \tau_B X/Z \quad . \quad (7)$$

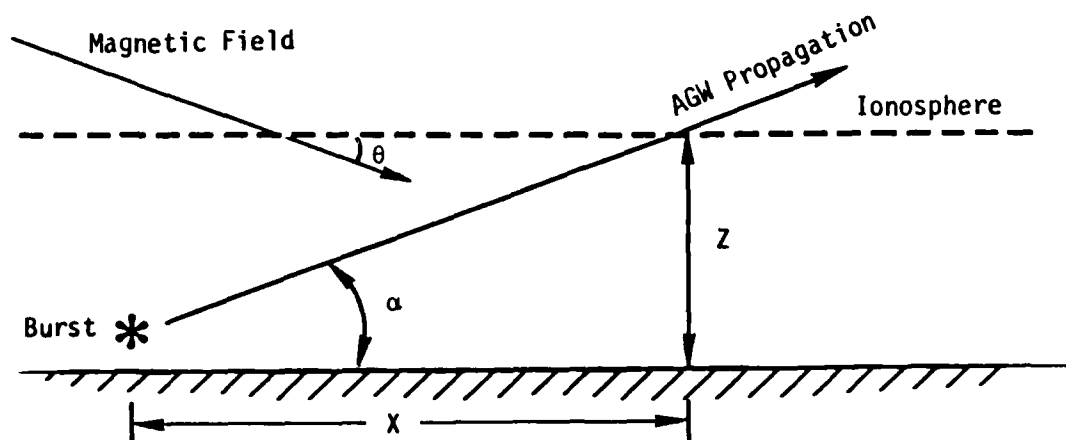


Figure 1. Burst geometry.

Therefore the argument of the sinusoidal function describing the variation can be taken as

$$\text{ARG} = \frac{2\pi Z}{\tau_B X} \left(t - \frac{X}{c} \right) \quad (8)$$

and this will satisfy Equation 7 at the time of onset of the disturbance,

$$t_0 = X/c, \quad (9)$$

where c is the speed of propagation.

Although not addressed specifically to this point, studies have indicated that the disturbance is nearly independent of the burst altitude⁵ provided the burst is below ~30 km. These studies also suggest that the effect goes like the square root of the yield^{5,6} and we will adopt this condition. This dependence is not well established.

The intensity of the disturbance varies with the altitude of observation, increasing up to ionospheric levels, and decreasing above the F-region due to dissipation from viscous effects. Based loosely on the work of Francis¹ we take the dependence of the fluid velocity on observation altitude to be

$$1 - \left(\frac{Z - Z_p}{Z_L - Z_p} \right)^2 \quad Z_L < Z < 2Z_p - Z_L$$

$$0 \quad \text{otherwise.} \quad (10)$$

Here Z_p is the altitude of peak effect (~300 km) and the Z_L is the lowest affected altitude (~100 km).

If we assume that the variation of Equation 10 is the largest contributor to $\nabla \cdot \mathbf{V}$ we can use Equation 1 to write

$$\frac{D}{Dt} \ln N = \frac{2(Z-Z_p)}{(Z_L-Z_p)^2} \frac{V_Z}{\left[1 - \frac{(Z-Z_p)^2}{(Z_L-Z_p)^2} \right]} \quad (11)$$

which integrates to give

$$N = N_0 \exp \frac{2(Z-Z_p)}{(Z_L-Z_p)^2} \left(\frac{\Delta Z}{\left[1 - \frac{(Z-Z_p)^2}{(Z_L-Z_p)^2} \right]} \right) \quad (12)$$

Experiment shows that gravity waves slowly decay in strength as they propagate away from the source. The nuclear data does not show this decay clearly, due chiefly to the fact that different modes (frequencies) with different amplitudes are observed at different distances from the bursts. We have therefore relied on typical results from ducted modes to estimate a spatial decay factor.

$$\exp (-4 X/C_E) \quad , \quad (13)$$

where C_E is the earth's circumference.

The model thus assembled gives values of ΔN and ΔZ as

$$\Delta N = \exp \frac{Q_3 \Delta Z}{Q_2}$$

and

$$\Delta Z = - C_Z \cdot Q_1 \cdot Q_2 \quad (14)$$

where ΔZ is the change in altitude of plasma initially at Z and ΔN is the factor by which the electron density initially at $Z - \Delta Z$ is multiplied to obtain the new electron density at Z .

The factors in Equation 14 are

$$Q_1 = (Y_{MT})^{1/2} \cos(\phi) \sin(2\theta) \sin \frac{2\pi Z}{\tau_B X} (t - \frac{x}{c}) ,$$

$$Q_2 = \left[1 - \left(\frac{Z - Z_P}{Z_P - Z_L} \right)^2 \right] \exp (-4X/C_E) ,$$

and

$$Q_3 = \frac{2(Z - Z_P)}{(Z_P - Z_L)^2} . \quad (15)$$

Our fit to the data requires

$$Z_P = 300 \text{ km} , \quad \tau_B = 540 \text{ sec},$$

$$Z_L = 100 \text{ km} , \quad c = .65 \text{ km/sec}$$

$$C_E = 4 \cdot 4^4 \text{ km} \quad C_N = .2 (MT)^{-1/2}$$

$$\text{and} \quad C_Z = 20 \text{ km/MT}^{1/2} . \quad (16)$$

In applying this model, a set of restrictions are required. First,

$$600 \text{ km} < X , \quad (17)$$

since the region nearly over the burst is not well described. Furthermore, given that only two oscillations of the function provide the complete response, there will be an effect for

$$\frac{\lambda}{c} < \tau < \frac{\lambda}{c} + \frac{2X\tau_B}{Z} \quad (18)$$

Also, the model will apply only for

$$100 \text{ km} < Z < 500 \text{ km} \quad (19)$$

and outside this region Equation 10 provides that there will be no effect.

SECTION 3

THE MODEL FOR RANGES LESS THAN 600 KILOMETERS

The model, described in detail in Chapter 2, for ranges greater than 600 km must be extended to include the region nearer the burst. The model for large ranges was based upon general properties of acoustic gravity waves and upon what data were available. We do not know in detail what physical processes are involved in generating and propagating the long period ionospheric signals which have been observed thousands of kilometers from the burst point so we are in no position to attempt a first principle calculation of the effects and must rely heavily on the data. For the region nearer the burst we believe we know what phenomena will be important and we can perform calculations of the expected effects. We have made these calculations for a set of yields and locations. Below we give the results of the calculations and present a model which fits these results well enough and matches smoothly to the previously described model for large ranges.

The processes we wish to calculate and model are briefly described as follows. The blast wave leaves the point of the explosion, assumes the shape of an N-wave, that is, a pulse which goes discontinuously to some positive value, decreases linearly to a negative value of equal magnitude, then goes discontinuously to zero (see Appendix A) and weakens sufficiently to allow for propagation in the acoustic limit. As the weak acoustic pulse propagates into the rapidly decreasing density of the higher atmosphere it restrengthens, forming a shock at high altitudes which can in some cases be quite strong. After the strong N-wave portion of the upwardly propagating pulse passes a given point there will remain a residual oscilla-

tion due to the buoyant interaction of the stratified atmosphere with the earth's gravitational field. In this report we will not attempt to model the N-wave itself (we hope to do so in the future) but will concentrate on the residual oscillations since it is these oscillations which form the "gravity wave" in the region close to the burst point.

In a previous report the authors have described a procedure for calculating the properties of the N-wave as it propagates upwardly through the atmosphere. This report was originally classified but has recently been declassified and we have appended a portion of the report, which describes the phenomenology of the N-wave pulse in some detail and specifies our procedures for calculating the properties of the pulse, to the present report as Appendix A. The computer code which calculates the properties of the N-wave by the procedures of Appendix A is called MODEL.

The propagation of the pulse to high altitudes is an essentially nonlinear process (the pulse stretches to become many times its original length). The residual oscillations which remain after the passage of the pulse will often be accurately described by the linearized equations of hydrodynamics. We assume this will always be the case. The linearized equations of hydrodynamics admit a solution by means of a Green's Function which has been given in closed form. We can use the Green's Function to represent the upward propagation of an N-wave pulse and the associated residual oscillations by a contour integral around a closed contour in complex frequency space. Since the propagation is controlled by linear equations the length of the N-wave will not change as it propagates. As with any linear system, the strength of the pulse is controlled by an overall multiplicative factor. As a part of a previous research effort we developed a computer program to calculate the necessary contour integral. The report of the research is unpublished, but the section deriving the equations and describing the program, called CINT, which performs the integration is appended to the present report as Appendix B.

The plan for the present calculation is as follows. We choose parameters for a burst and select a point in the ionosphere at which to calculate the gravity wave. We then run MODEL to determine the proper pulse length and amplitude for the N-wave at the point in question. We use the results from MODEL to set the pulse length and amplitude factor for CINT which will then calculate the parameters of the gravity wave at the point we wish to study.

As presently configured our computer codes calculate only the pressure. The current task requires that we have knowledge of velocities and displacements. In principle we could modify the codes to calculate the velocities but we have not yet done so. In both the acoustic limit and the low frequency limit for a single frequency we find the result that $v_z = \cos\theta \, c \, \delta p / \gamma p_0$ and $v_r = \sin\theta \, c \, \delta p / \gamma p_0$ where c is the speed of sound, δp the pressure perturbations, p_0 the ambient pressure, γ the adiabatic constant, and θ the angle, measured from the vertical, subtended by a line drawn from the burst point to the point for which we are performing the calculation. We believe that these relations will in general hold to within the accuracies required and we will use the codes to calculate the pressure fluctuations and then after the velocities using these relations.

The oscillations which follow the passage of the N-wave do not fall abruptly to zero after some time but die away more or less gradually as a function of time. We will not try to describe this process for our model, however, but will choose a simple sinusoidal function whose amplitude and period we will select to approach the results from CINT as best we can. To display for the reader what has actually been done we show an example in Figure 2. The graph shows the output from CINT which resulted from a run for 300 km altitude directly above a three megaton nuclear explosion at sea level. The results from the code MODEL indicate that the length of the N-wave should be 370 seconds and that the relative

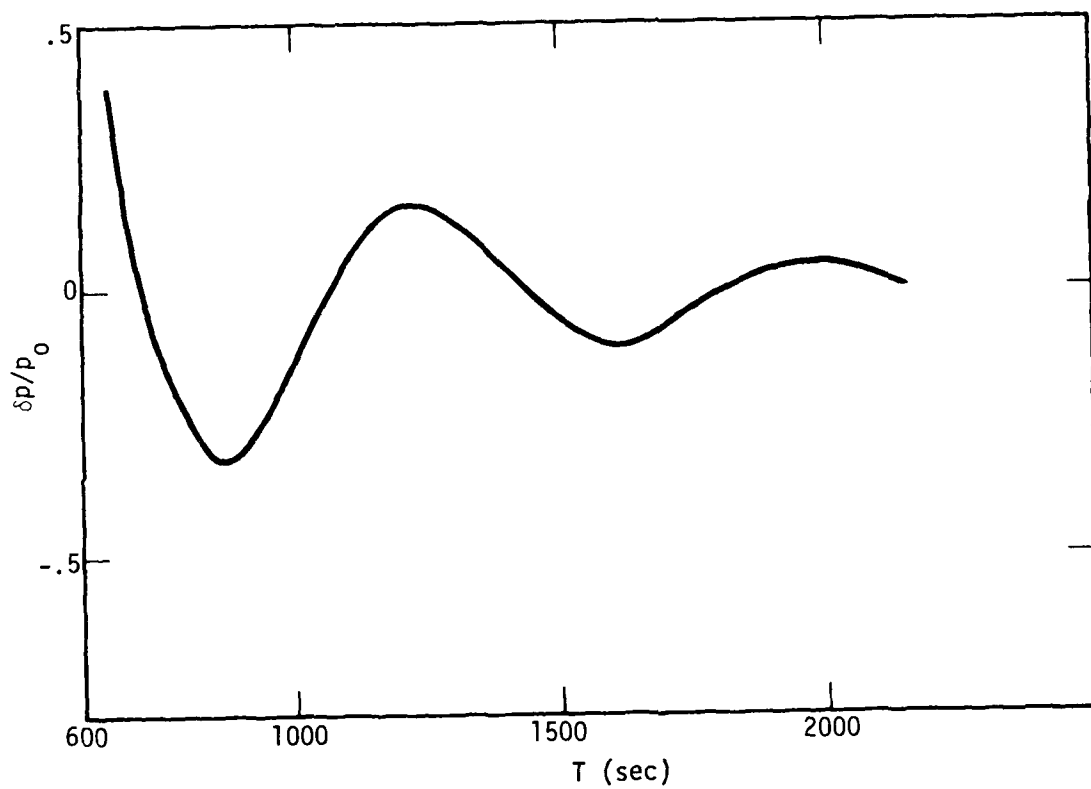


Figure 2. $\delta p / p_0$ as a function of time 300 km directly above a 1 MT explosion. The earlier N-wave phase is not shown.

overpressures at the shock should be 1.7. The time of arrival of the N-wave is 158 seconds so the residual oscillations which we call gravity wave, will occur after 600 seconds. The period is readily chosen from the graph to be 720 seconds but the choice of amplitude is not clearcut. We chose the amplitude to be .3 and the duration to be two periods.

Not all cases provide such an easily determined, constant period as that graphed in Figure 2. In Table 1 we have attempted to organize the information on the period of the gravity wave as a function of location and bomb yield. The entry, L , is the length of the N-wave portion of the pulse in seconds. τ_c is the natural period of freely propagating gravity waves defined in the previous chapter. The entries, ΔT , are the time (seconds) between successive zero crossings during the gravity wave phase, that is, after the N-wave has passed. We see that most often ΔT is reasonably close to $1/2 \tau_c$. In the worst cases the difference is a factor of two for the first ΔT and much less for later ones. The examples which show the greatest deviation of ΔT from $1/2 \tau_c$ are those for which $L \ll 1/2 \tau_c$. Since the model for ranges greater than 600 km has an oscillatory period of τ_c it is a matter of considerable convenience to choose τ_c for the period when the range is less than 600 km. The data in the table show that τ_c is probably the best simple choice we can make so we fix the period of the oscillations at all ranges to be τ_c and the duration of the effect at all ranges to be $2\tau_c$. Notice that the duration is greater at greater ranges.

We now attempt to study the altitude dependence of the gravity wave for ranges less than 600 km from the burst point. Having chosen τ_c for the period of the oscillations we have a model for which the maximum displacement will be A/τ_c where A is an amplitude factor which we chose from CINT output as discussed above. In Table 2 we show the resulting displacements for several altitudes at three different ranges from a 3 MT surface burst. In all cases the displacement is small at an altitude of

Table 1
(Entires are in seconds)

	$\begin{matrix} r \\ Z \end{matrix}$	0 km	300 km	600 km
Y=.3MT	300 km	$L=230; \frac{1}{2} \tau_c=396$	$L=264; \frac{1}{2} \tau_c=560$	$L=230; \frac{1}{2} \tau_c=884$
		$\Delta T=350; 362; 389$	$\Delta T=283; 402; 462$	$\Delta T=396; 663; 399$
	200 km	$L=171; \frac{1}{2} \tau_c=317$	$L=191; \frac{1}{2} \tau_c=572$	
		$\Delta T=278; 289; 294$	$\Delta T=400; 513; 545$	

	$\begin{matrix} r \\ Z \end{matrix}$	0 km	300 km	600 km
Y=3MT	300 km	$L=370; \frac{1}{2} \tau_c=396$	$L=436; \frac{1}{2} \tau_c=560$	$L=357; \frac{1}{2} \tau_c=884$
		$\Delta T=341; 359; 369$	$\Delta T=409; 471; 501$	$\Delta T=670; 809; 911$
	200 km	$L=254; \frac{1}{2} \tau_c=317$	$L=337; \frac{1}{2} \tau_c=572$	$L=400; \frac{1}{2} \tau_c=1003$
		$\Delta T=292; 290; 296$	$\Delta T=406; 515; 543$	$\Delta T=770; 964; 1041$

	$\begin{matrix} r \\ Z \end{matrix}$	0 km	300 km	600 km
Y=30MT	300 km	$L=460; \frac{1}{2} \tau_c=396$	$L=608; \frac{1}{2} \tau_c=560$	$L=850; \frac{1}{2} \tau_c=880$
		$\Delta T=328; 361; 362$	$\Delta T=464; 478; 497$	$\Delta T=677; 824; 879$
	200 km	$L=342; \frac{1}{2} \tau_c=317$	$L=514; \frac{1}{2} \tau_c=572$	$L=714; \frac{1}{2} \tau_c=1003$
		$\Delta T=289; 290; 295$	$\Delta T=431; 500; 546$	$\Delta T=804; 939; 984$

100 km. The displacements are seen to peak at about 300 km altitude for each of the three ranges. Recall that the model for ranges greater than 600 km also had a peak at 300 km altitude, the function being $[1-(z-300)^2/200^2]$. In Figure 3 we graph the curve showing the altitude dependence for the model for large ranges and show the points for the data given in the table where we have normalized the displacements for each range to be one at 300 km altitude. The points cannot be said to all lie on the curve, but given the crude nature of our method for arriving at the displacements and the need for as simple a model as will suffice, it is adequate and desirable to use the same altitude dependence for all ranges. We use the one given in Equation 15.

Table 2

	Z	r		
		0 km	300 km	600 km
Y=3MT	500	19	9	17
	400	21	29	39
	300	22	31	81
	200	21	29	43

The fact that the period and altitude dependence of the disturbance can be taken to be the same for ranges less than 600 km as for ranges greater than 600 km encourages us to try a fairly simple modification of Equation 15 as a model for all ranges. We take the horizontal neutral displacement to be

$$\Delta X_N = - (Y_{MT})^{1/2} \frac{X}{R} C_Z Q_2 \sin \left(\frac{2\pi Z}{T_B R} \left(t - \frac{R}{C} \right) \right) \quad (20)$$

where $R = (Z^2 + X^2)^{1/2}$ and C_Z and Q_2 are as in Equations 15 and 16. We choose the neutral displacement in the vertical direction to be

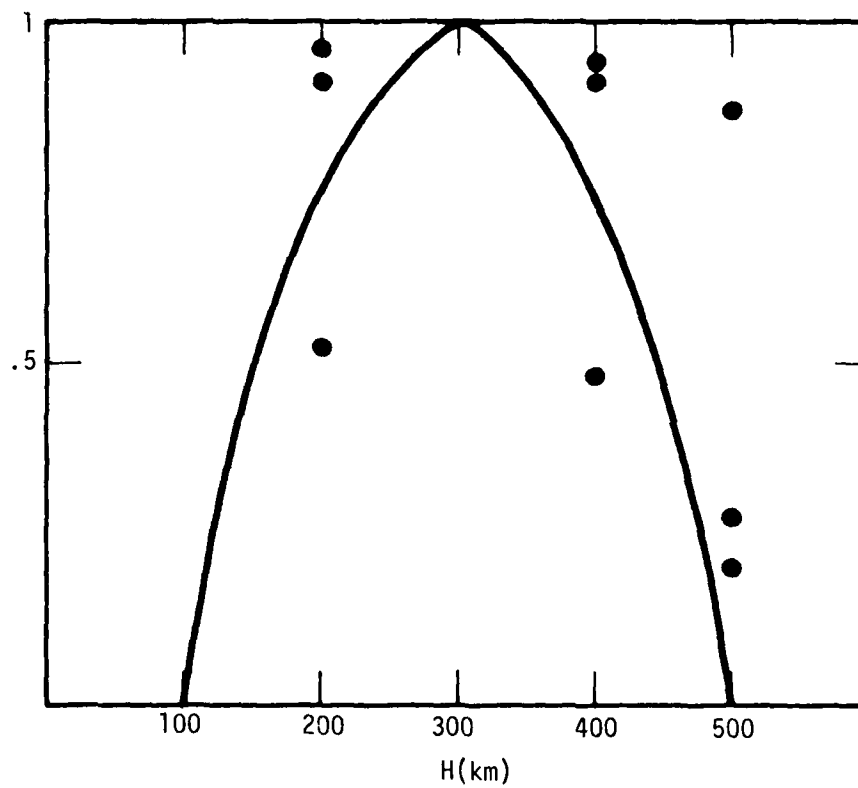


Figure 3. A comparison between the altitude dependence of the model (solid curve) and the CINT results (dots).

$$\Delta Z_N = (Y_{MT})^{1/2} \frac{x}{R} C_Z Q_2 \sin \left(\frac{2\pi Z}{\tau_B R} \left(t - \frac{R}{C} \right) \right) \quad (21)$$

In the limit of small z/x we find that ΔZ_N goes to zero while ΔX_N goes to the neutral motion on which the model for ranges greater than 600 km was based.

We have argued that the period and the altitude dependence of Equations 20 and 21 are appropriate for our model; we must now check to see whether the amplitude of the displacements given by Equations 20 and 21 agree well enough with those which result from our calculations. In Table 3 we give the maximum displacements which result from choosing an

Table 3.
(Entries are in km)

$Y \backslash r$	0 km	300 km	600 km	Results from the Model
30 MT	66	114	295	109
3 MT	22	31	81	35
0.3 MT	6	7	10	11

amplitude based on output from CINT. For each entry the altitude is 300 km, the altitude of maximum effect. The last column shows results given by Equations 20 and 21 (Q_2 changes by only a few percent in 600 km so the equations would predict a nearly constant amplitude). Considering the arbitrariness involved in choosing an amplitude from CINT output we feel that the agreement between Equations 20 and 21 and the calculations is satisfactory. The two very bad numbers are the results at 600 km range for yields of 3 and 30 MT. For these cases CINT is not really appropriate anyway for the disturbances are so strong that nonlinear effects will certainly play a role. The nonlinear effects will probably act to reduce the displacements. The displacements given by Equations 20 and 21 are

relatively simple. They agree with Equations 15 for large ranges and agree reasonably well with our calculations for the region near the burst. We will adopt them as the basis for the gravity wave model.

Equations 20 and 21 give the components of the neutral motion. We wish to model the vertical motion of the electrons. We define

$$\Delta Z = - C_z (Y_{MT})^{1/2} Q_2 \sin \left(\frac{2\pi Z}{\tau_B R} \left(t - \frac{R}{C} \right) \right) \left[\cos \phi \sin 2\theta \frac{X}{R} - 2 \sin^2 \theta \frac{Z}{R} \right]$$

$$\Delta N = \exp (Q_3 \Delta Z / Q_2)$$

where C_z , Q_2 , Q_3 , ϕ , and θ , are as in Equations 15 and 16. If the unperturbed electron density is $N(Z)$ we specify the perturbed density to be $\Delta N \cdot N (Z - \Delta Z)$.

The fact that the displacement due to the gravity wave scales like the square root of the yield has implications with regard to modeling multiburst effects. If a region is simultaneously affected by gravity waves from two bursts whose burst points are remote from one another we would expect that the displacements would simply add in a linear way while the compressions would multiply. If this rule were to remain true for very close bursts the gravity wave effects would scale like the first power of the yield. We do not know the precise resolution of this apparent paradox but we believe that bursts sufficiently close together such that the resulting blast waves interact before they become weak will produce results as a single burst with the combined yield (the square root scaling) while bursts further apart will produce effects which may be added linearly. In the model for the computer programs we add the effects from all the bursts in a linear way. If the bursts are expected to be very close together in space and time it would be a good idea to combine them into a single burst at the input stage.

SECTION 4

EXAMPLES

In this chapter we present the results of applying the model to specific cases. In Figure 4 we show the results of a one megaton explosion at sea level. The contours are contours of constant electron density but we have used a highly artificial ionosphere in which the electron density is set equal to the altitude. Thus the plots would show ΔZ except for the effects of compression. We may think of the plots as showing the effective ΔZ which would produce the same electron density in incompressible flow. Probably the most important point to notice about Figures 4a and 4b is the strong effect of the magnetic field. In Figure 4a we show the propagation of the gravity wave in the north-south direction (magnetic coordinates). The location of the burst is at the center tick mark of the figures. To the right of the burst is magnetic north and in that direction the horizontal velocity moves the electrons down when the vertical velocity moves them up. The tendency is to cancel and the gravity wave does not appear large in the figure. To the left of the bomb, magnetic south, the horizontal and vertical components of the neutral flow move the electrons up and down in phase and the result is a greatly enhanced wave. For points sufficiently far north or south of the burst the vertical velocity will become negligible and the gravity wave will exhibit north-south symmetry. We see clearly in Figure 4a that after three hours and at a distance at nearly 2000 km the asymmetry is still pronounced.

In Figure 4b we show the propagation of the gravity wave in the east-west direction. In this case the horizontal motion of the neutrals does not cause vertical motion of the electrons so only the vertical

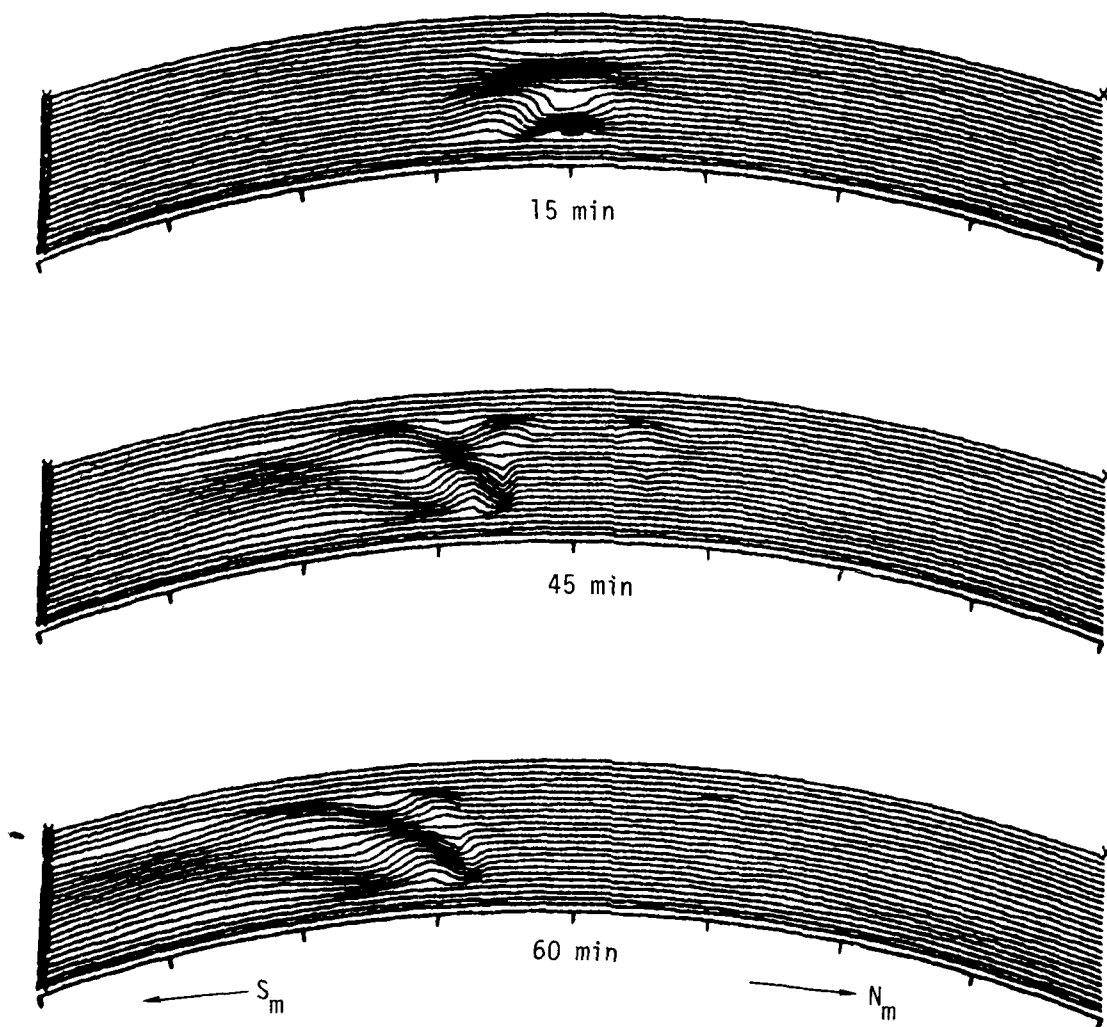


Figure 4a. Contours of electron density in an artificial ionosphere (see text) along a north-south line following a 1 MT nuclear explosion at sea level. The vertical tic marks are spaced 5° (~ 556 km) apart. The contour interval is 25 km.

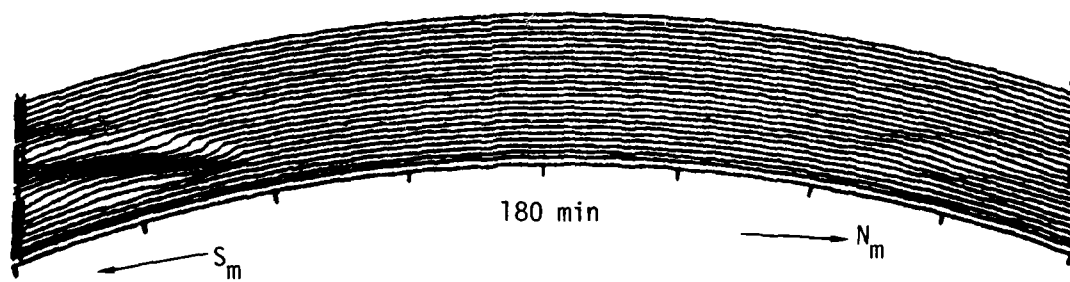
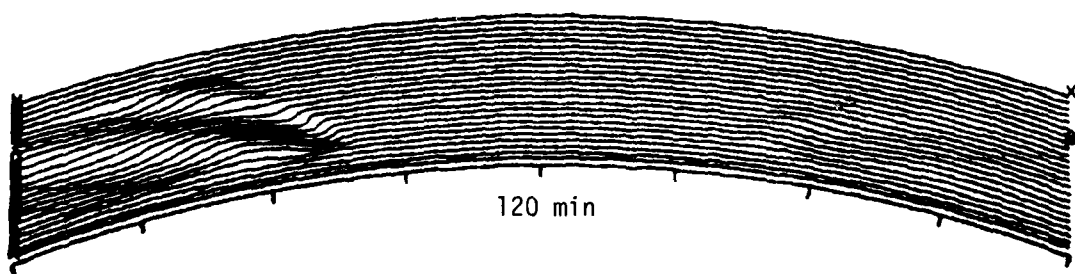
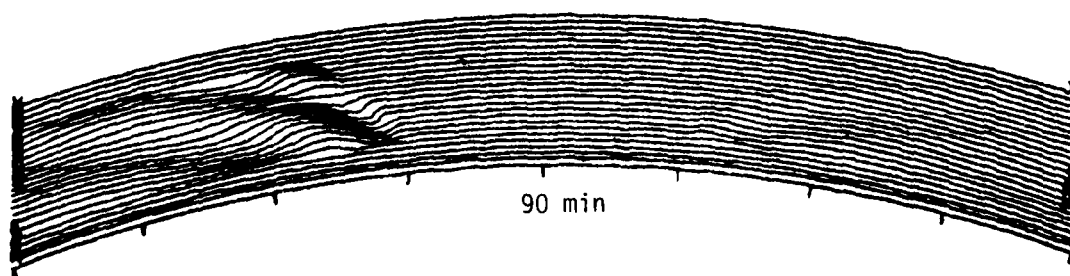


Figure 4a. (continued)

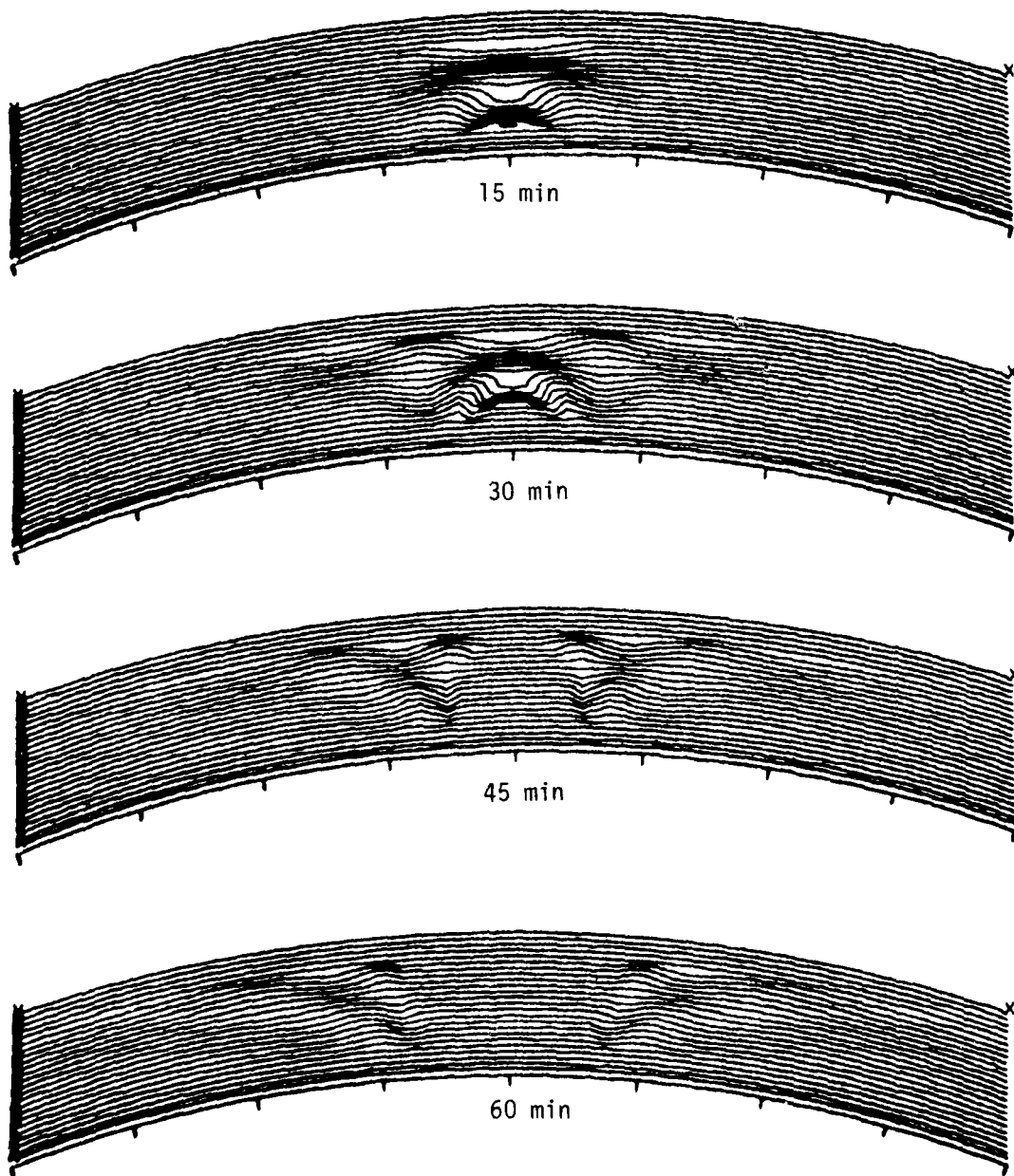


Figure 4b. Contours of electron density in an artificial ionosphere (see text) along an east-west line. The tic marks are 5° (~ 556 km) apart. The contour interval is 25 km.

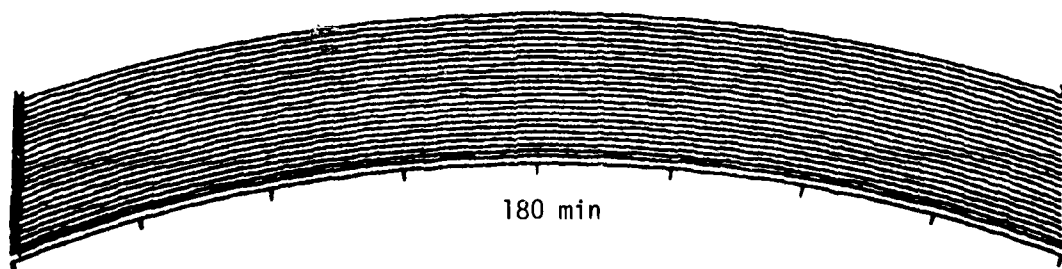
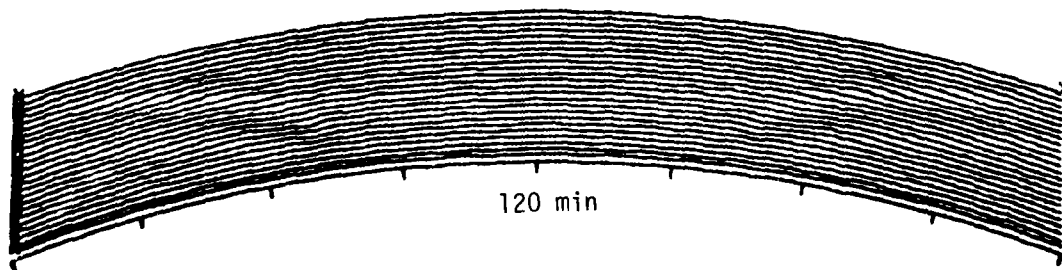
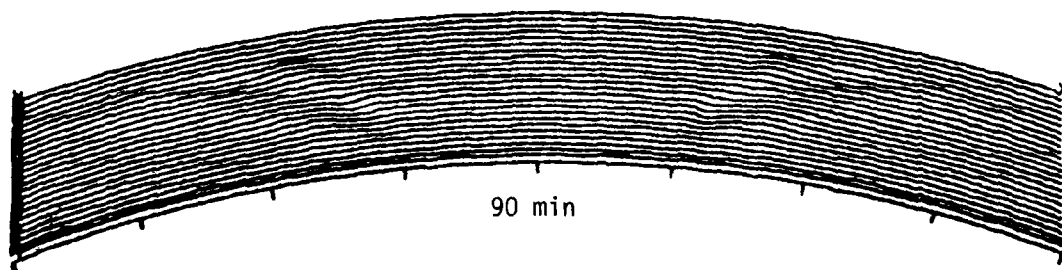


Figure 4b. (continued)

component of the neutral flow can move the electrons up and down. The effects of the gravity wave are therefore confined much more closely about the burst point and at a time of three hours and a distance of 1800 km the effects have nearly disappeared.

In Figure 5 we show contour plots of a somewhat different type. The lines are contours of constant electron density at an altitude of 250 km. Again we have used an ionosphere with the ambient electron density set equal to the altitude. The contours are shown in increments of 25 km starting with 25 km so the tenth, or J, contour is the ambient value for the horizontal plane we have chosen. For this figure there are two surface bursts, each 10 MT. Magnetic north is to the right and down in the figures. The field and the interaction of the two devices with one another produce a complex pattern of ionospheric disturbances even in this relatively simple case.

In Figure 6 we show another view of the same two bursts; in this case in a vertical plane located along the line which forms the X-axis for Figure 5. Along this line, which is close to the line joining the burst points, but slightly displaced, the ionosphere is seen to be severely disturbed for a period of hours.

We now wish to briefly consider effects on a realistic communications link from a portion of a large nuclear attack. The HF link, shown by the line in Figure 7, is from Omaha, Nebraska running some 2800 km northwest into British Columbia. We have considered 100 MT explosions at the starrrred points to represent attacks on Minuteman missile fields and a 30 MT explosion at the point marked by an asterisk. These events are presumed to be the total yield of many single bombs detonated close together at nearly the same time. In Figure 8 we show contours of the resulting disturbances in the same way as was shown in Figure 5. The ends of the HF link are marked on the figures by x's. Distance on the plots is distorted

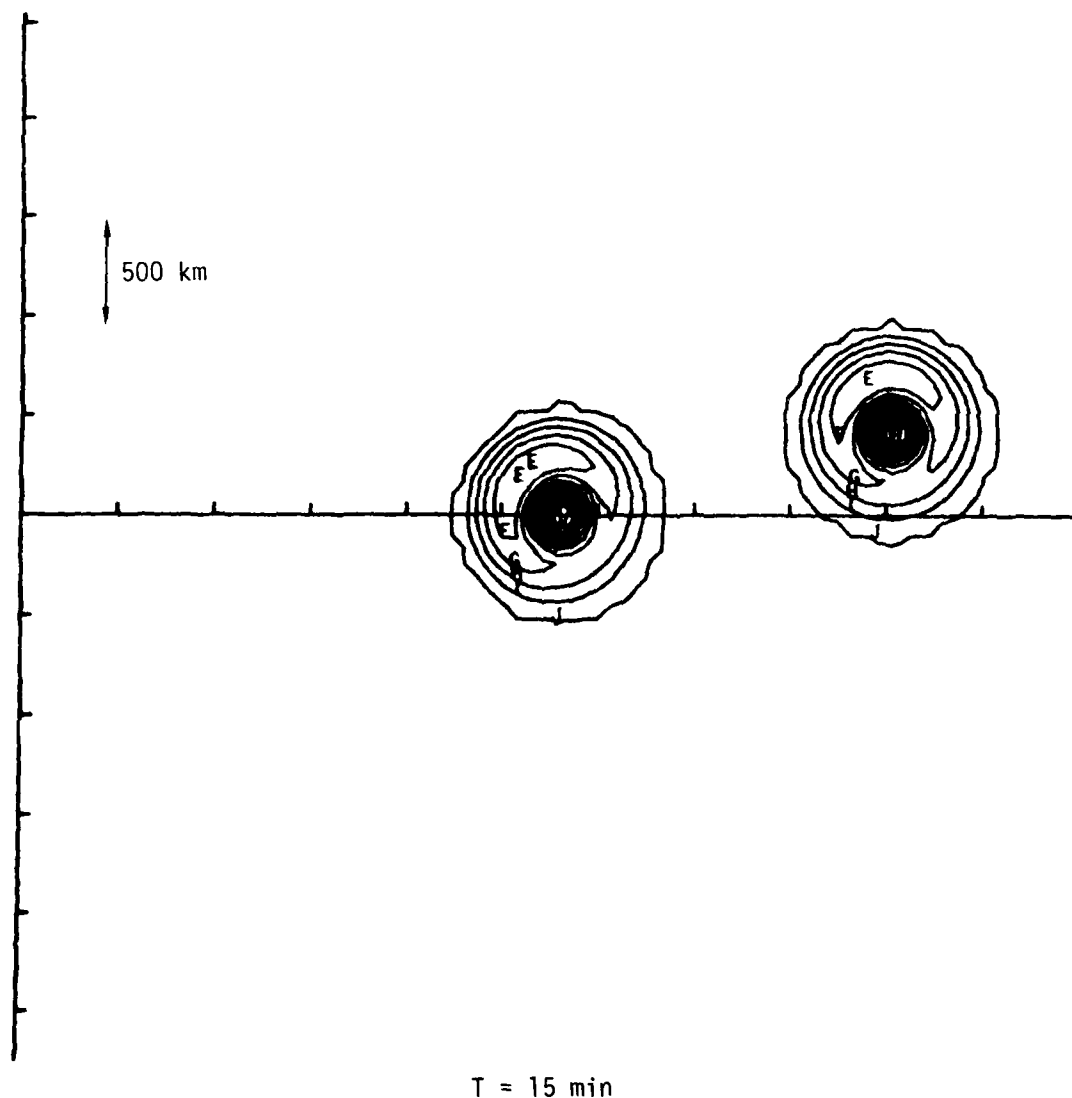
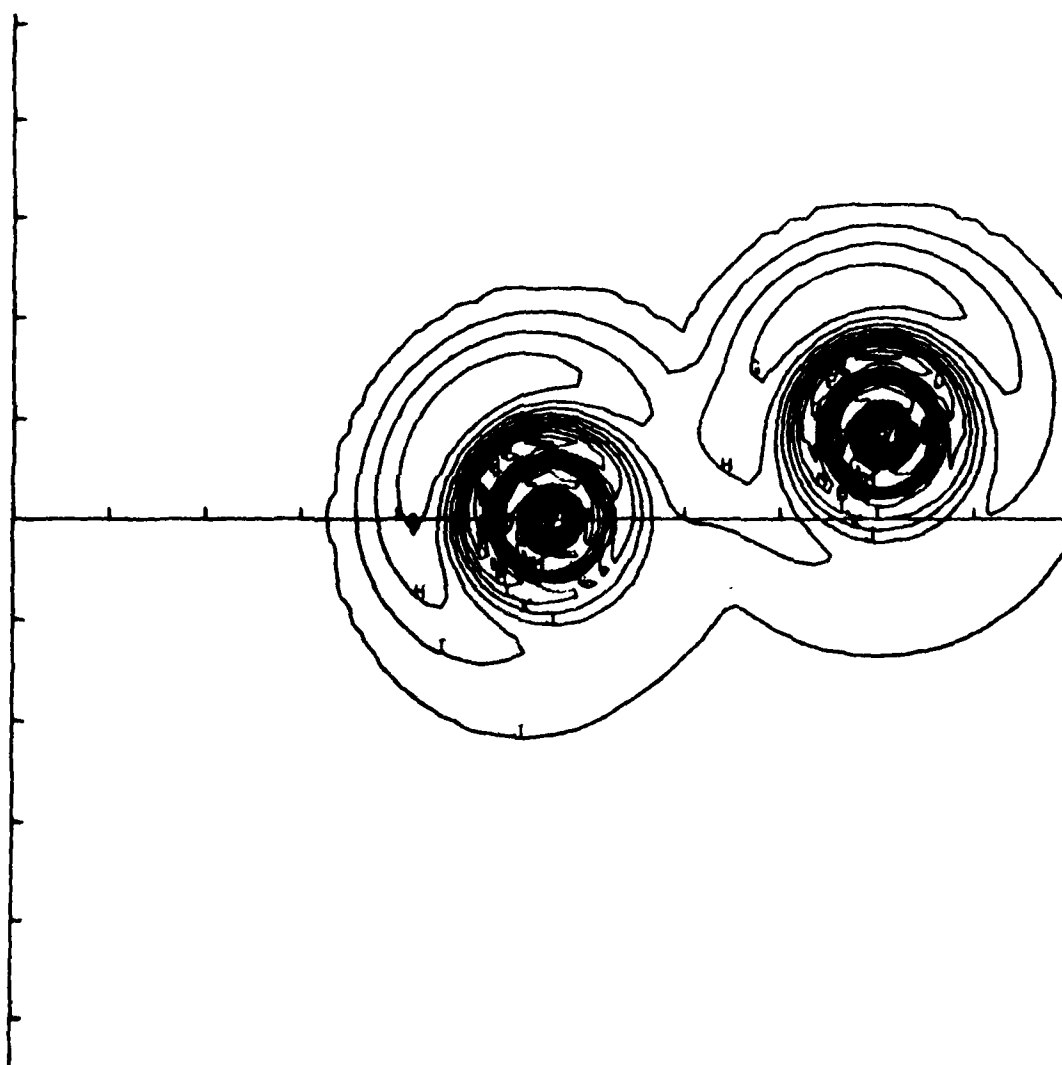
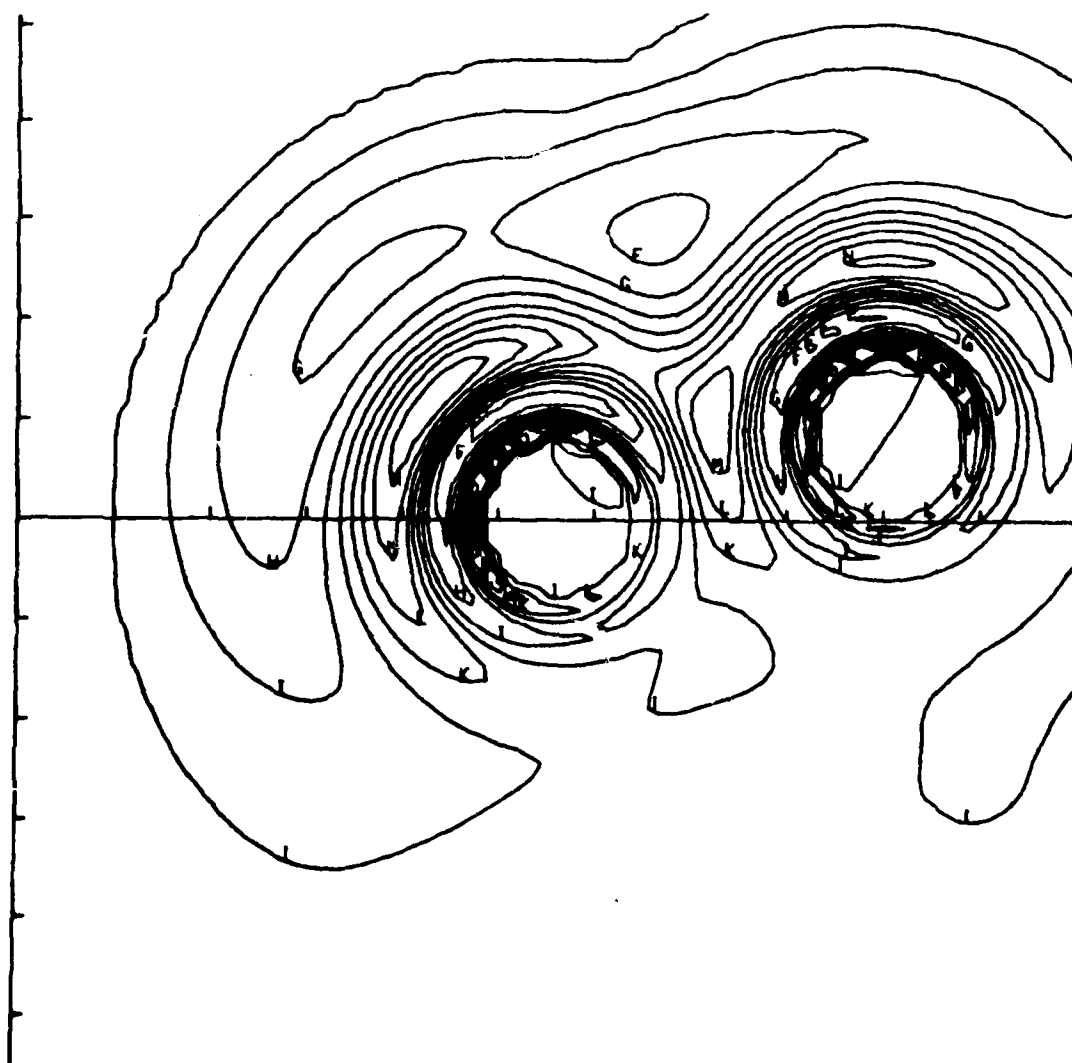


Figure 5. Contours of the electron density at 250 km altitude following two 10 MT explosions. An artificial ionosphere was used (see text). The tic marks are 500 km apart and the contour interval is 25 km.



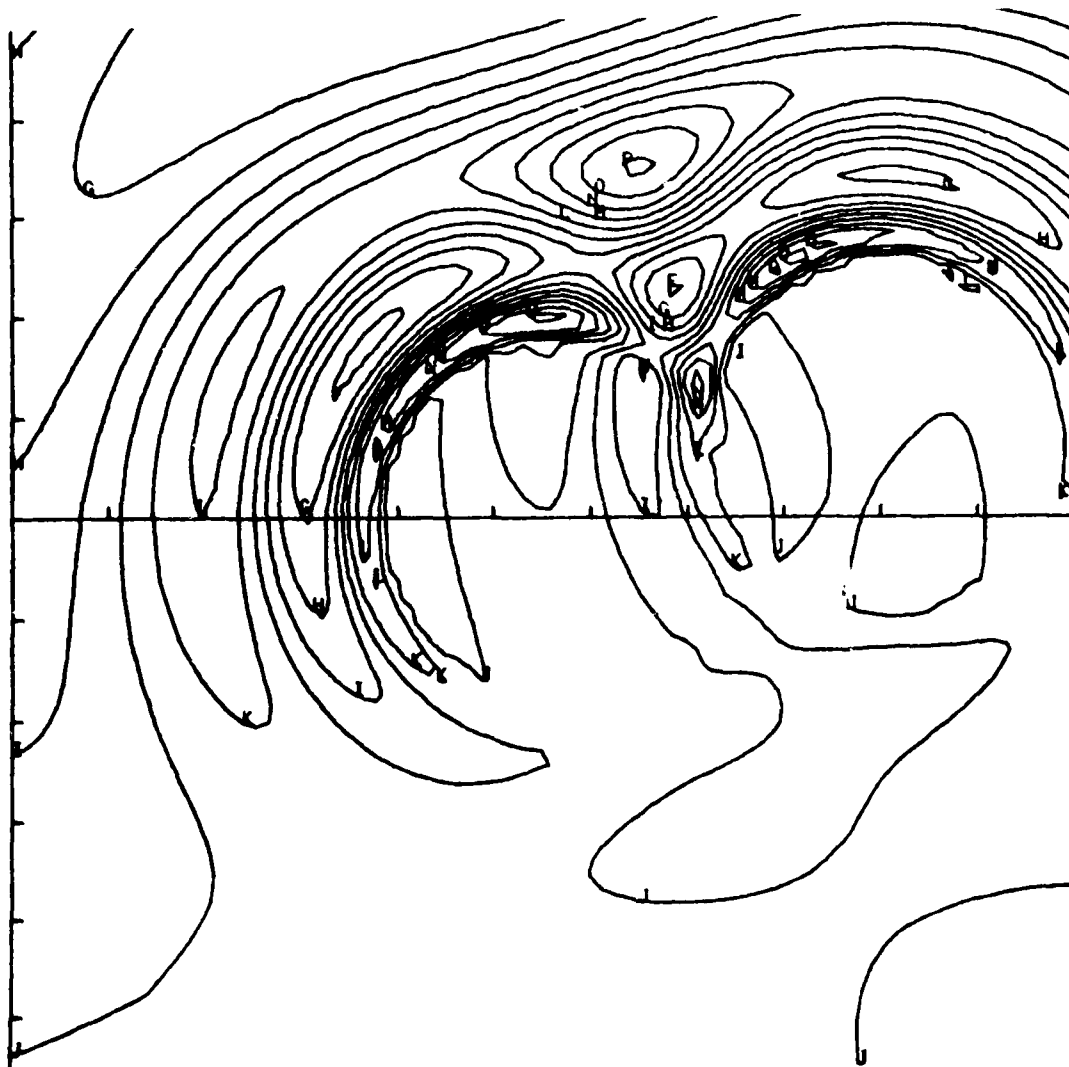
$\tau = 30 \text{ min}$

Figure 5. (continued)



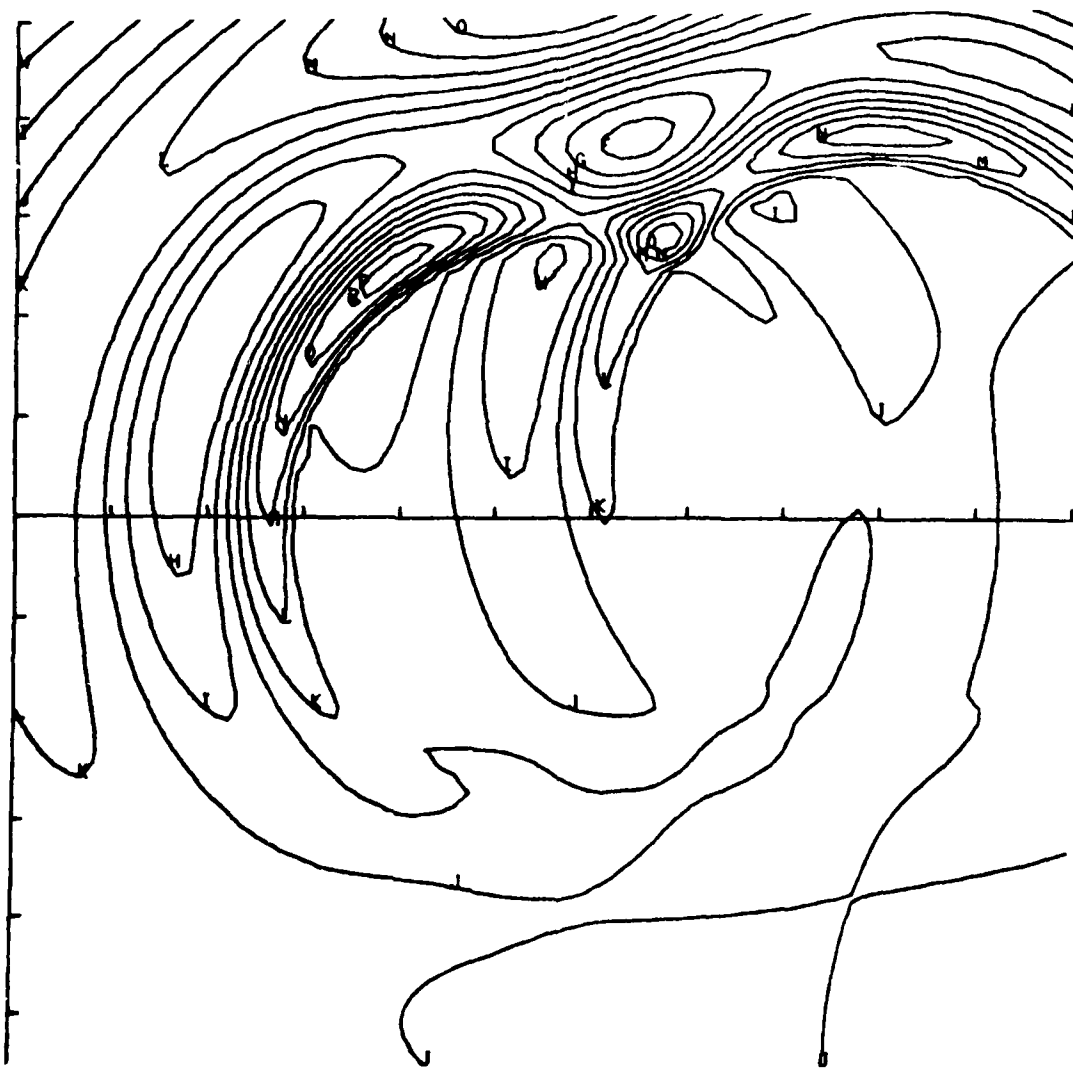
$T = 60 \text{ min}$

Figure 5. (continued)



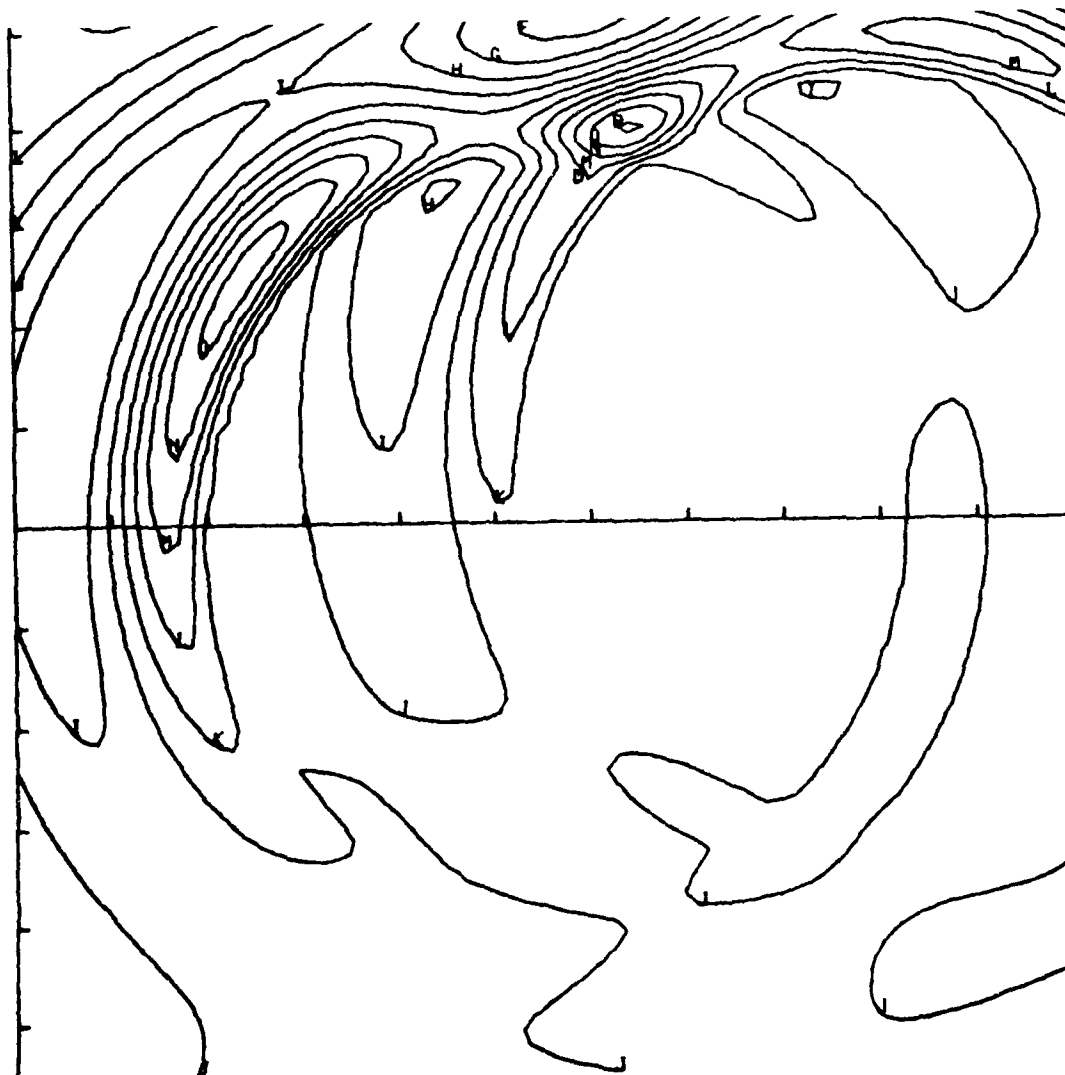
$T = 120 \text{ min}$

Figure 5. (continued)



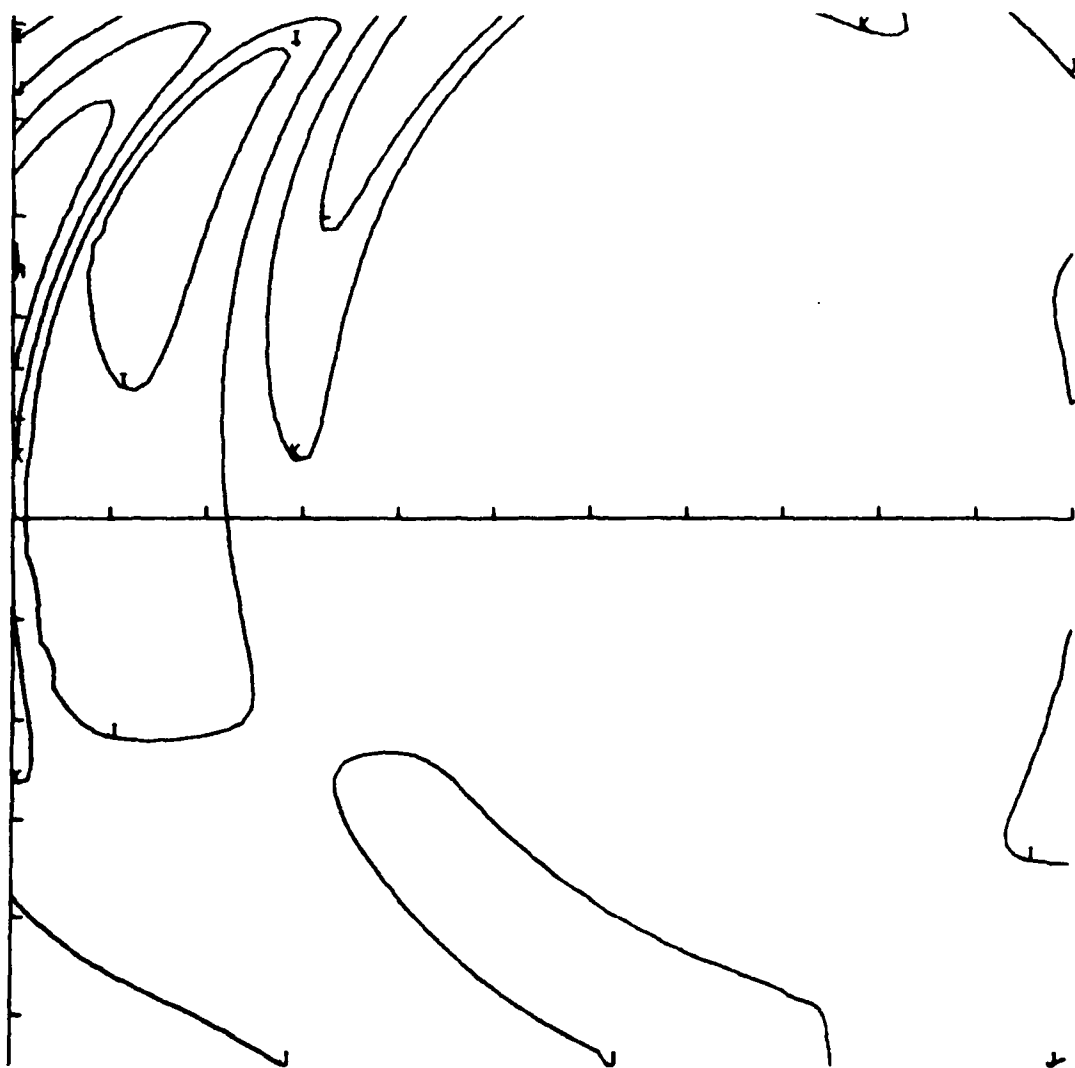
$T = 180 \text{ min}$

Figure 5. (continued)



$\tau = 240 \text{ min}$

Figure 5. (continued)



T = 360 min

Figure 5. (continued)

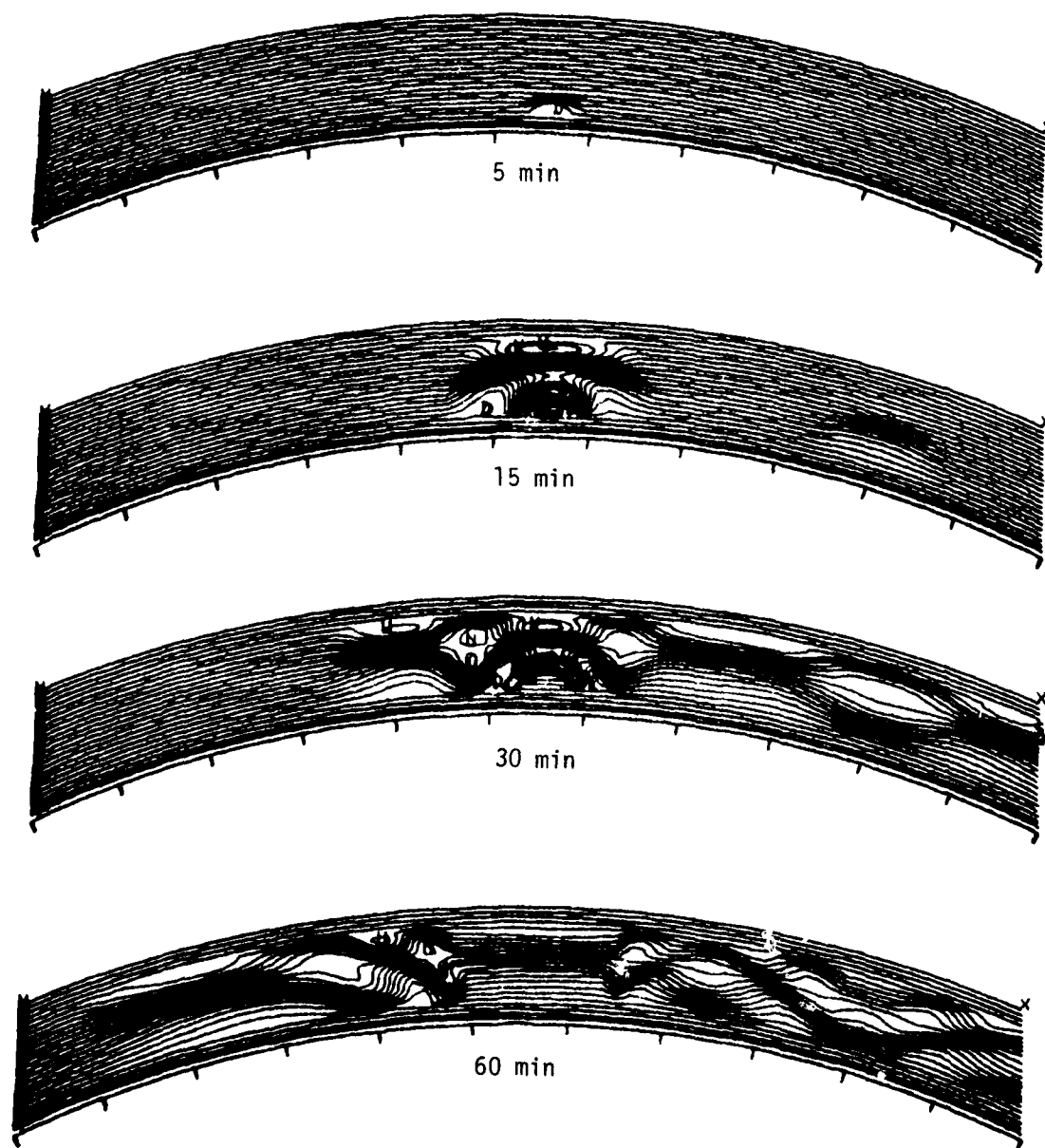


Figure 6. Contours of electron density for the event of Figure 5 along the line shown in Figure 5. The spacing between horizontal tic marks is 500 km. The contour interval is 25 km.

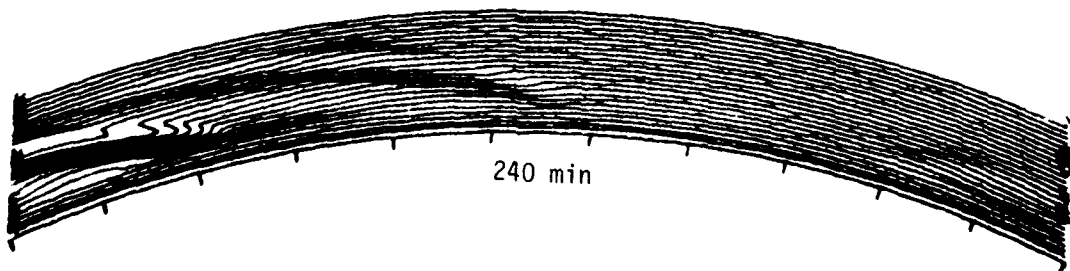
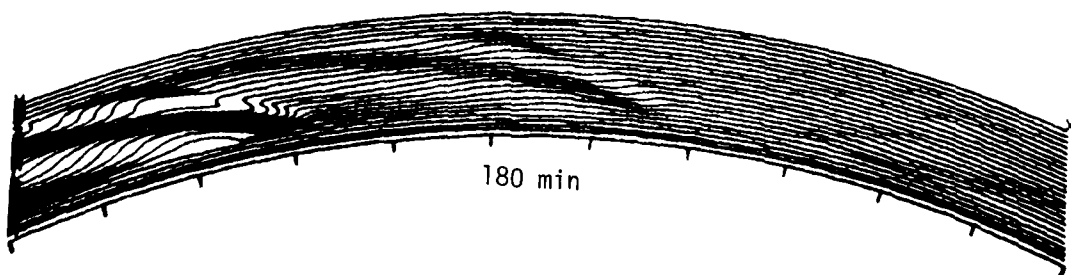
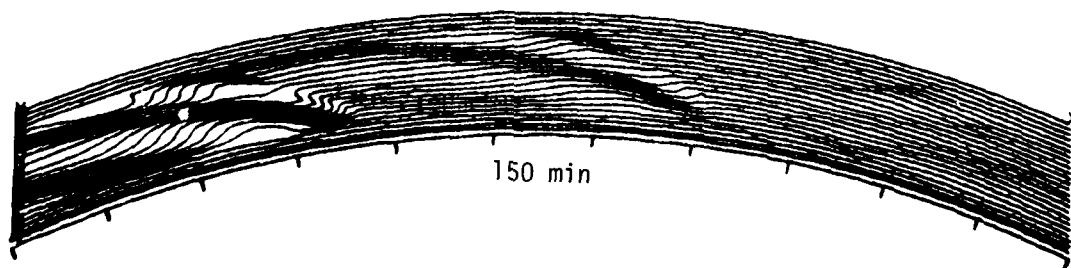
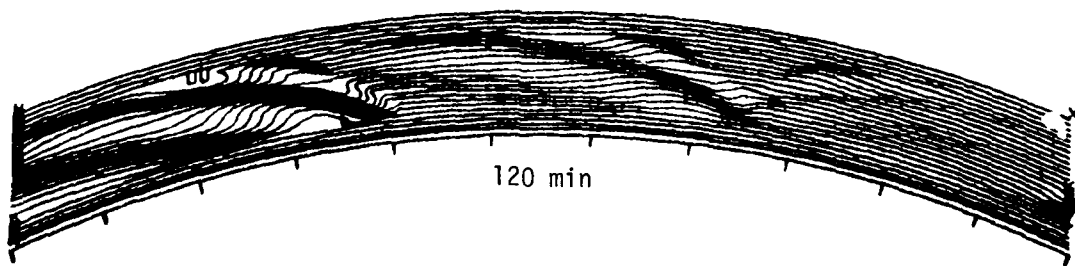


Figure 6. (continued)

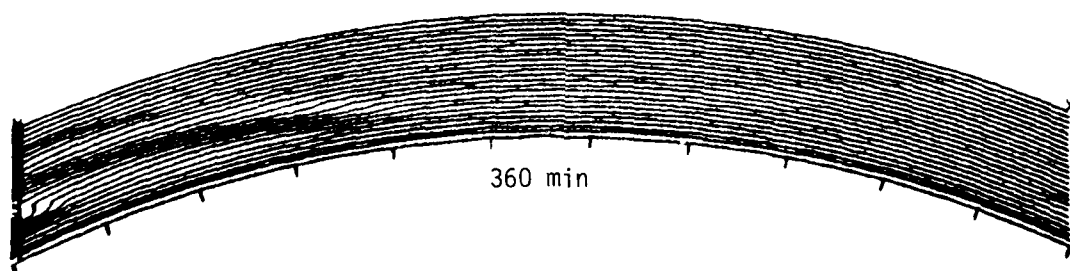
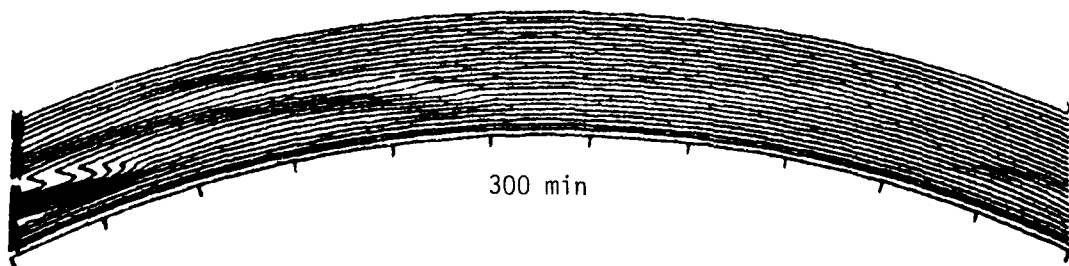


Figure 6. (continued)

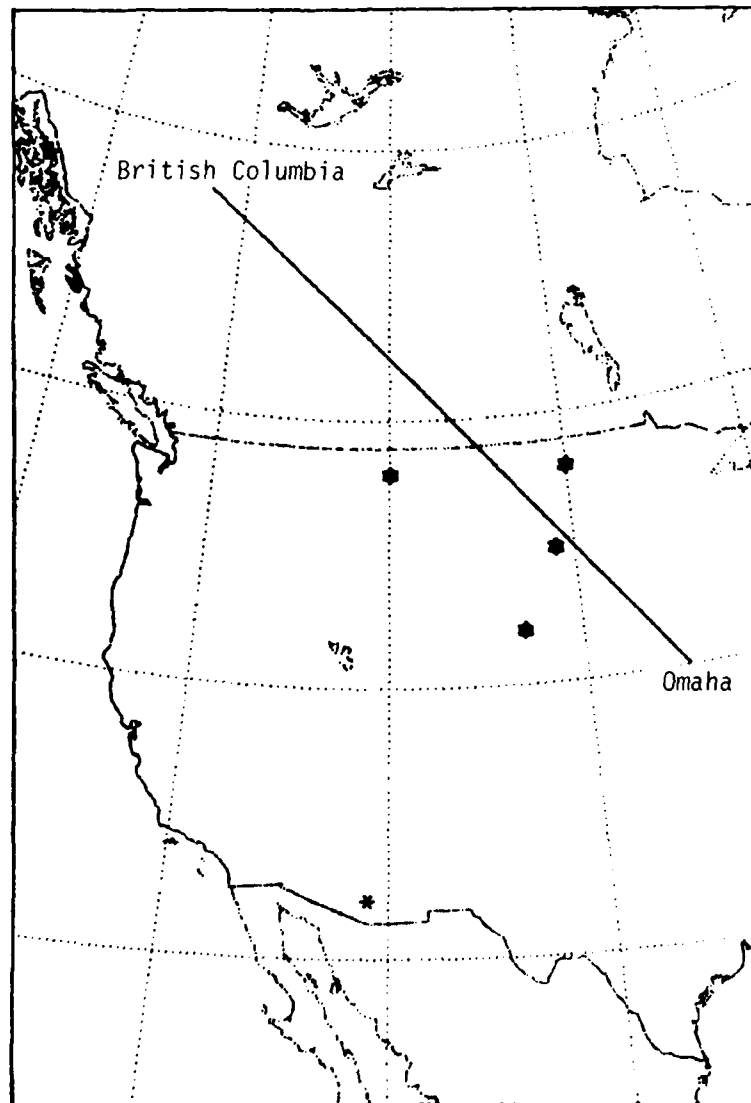


Figure 7. An HF link from Omaha, Nebraska to British Columbia and the location of explosions of 100 MT (star) and 30 MT (asterisk).

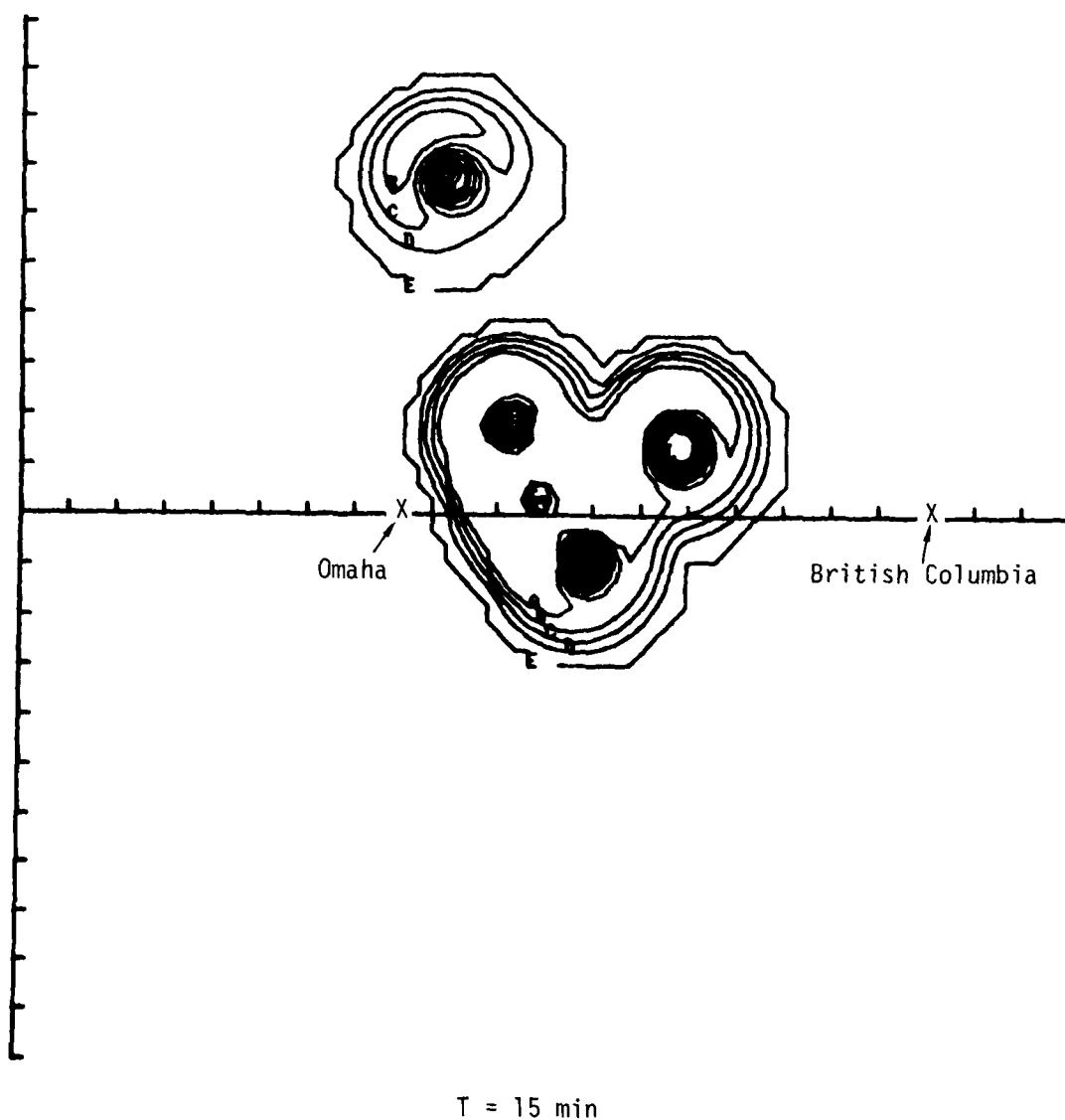
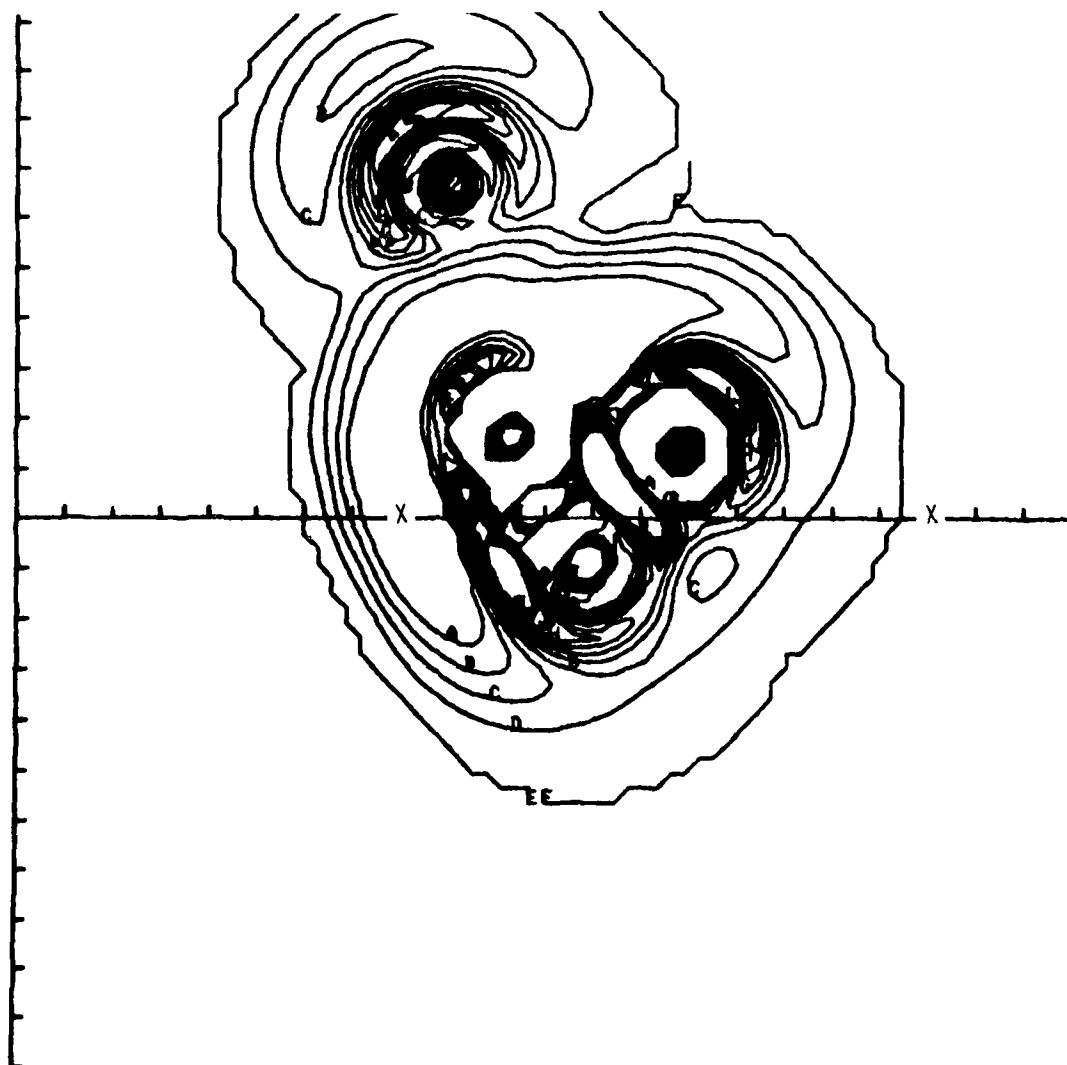
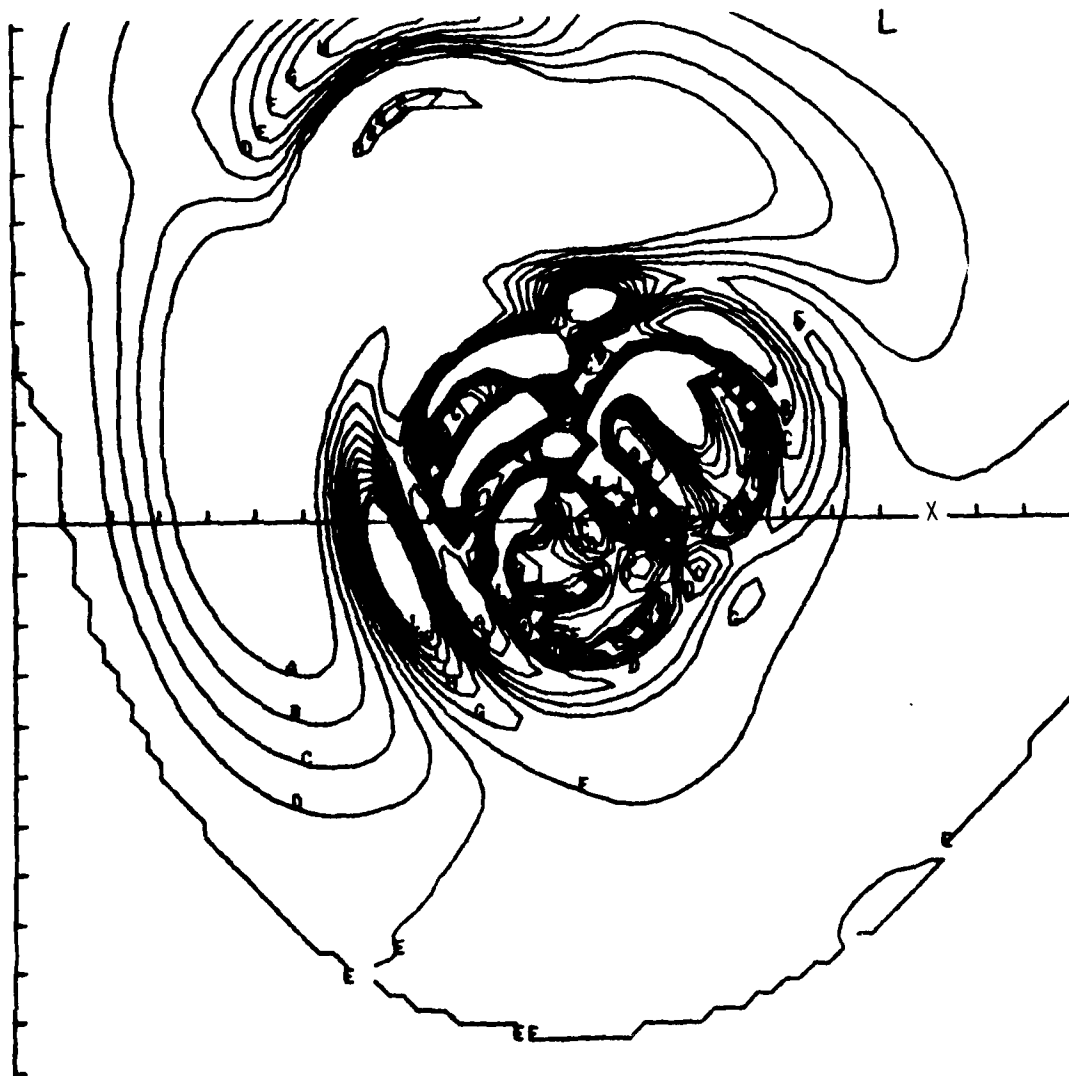


Figure 8. Contours of electron density (artificial ionosphere) at 250 km altitude following the attack. The X's mark the end points of the link shown. The tic marks are 250 km apart and the contour interval is 50 km.



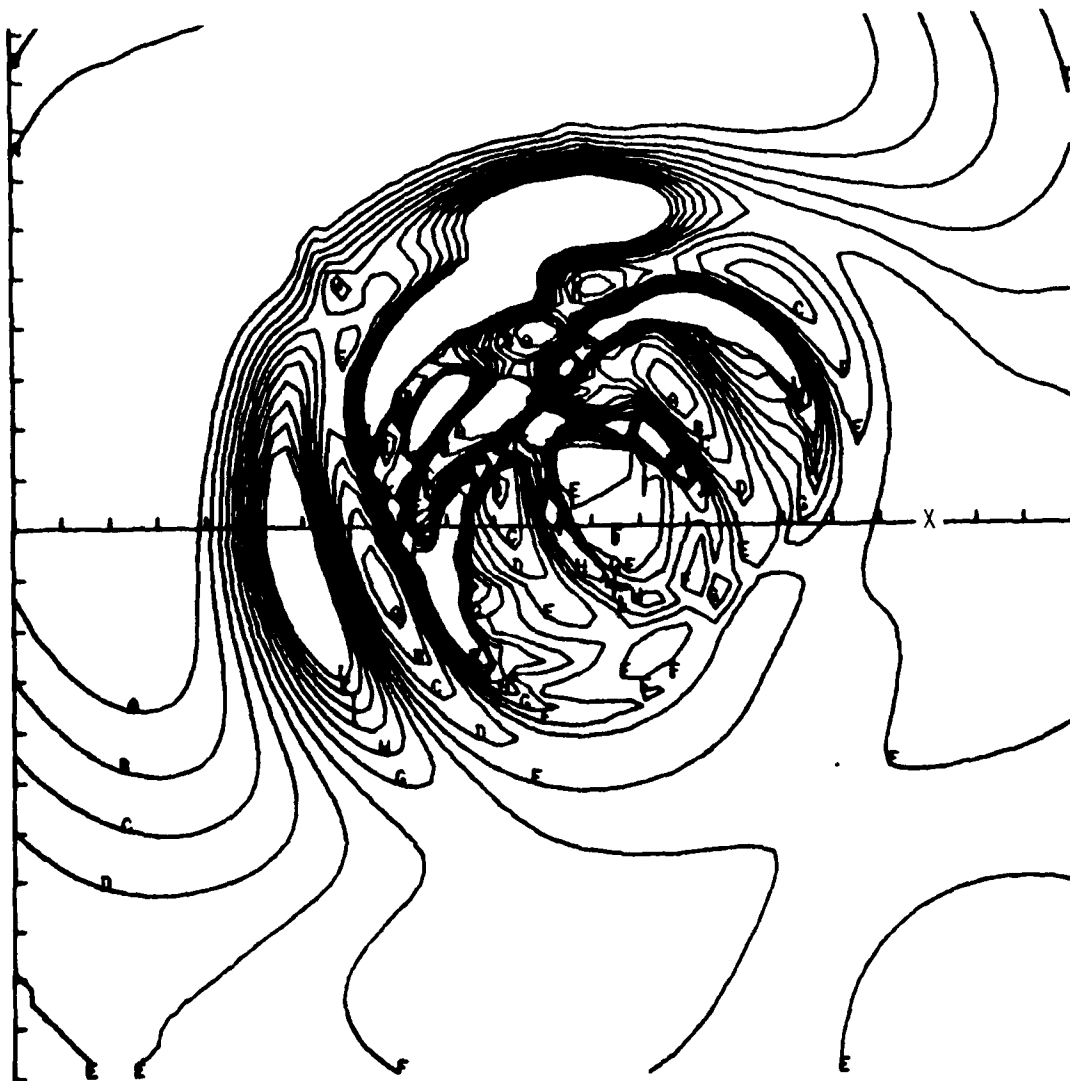
$T = 30 \text{ min}$

Figure 8. (continued)



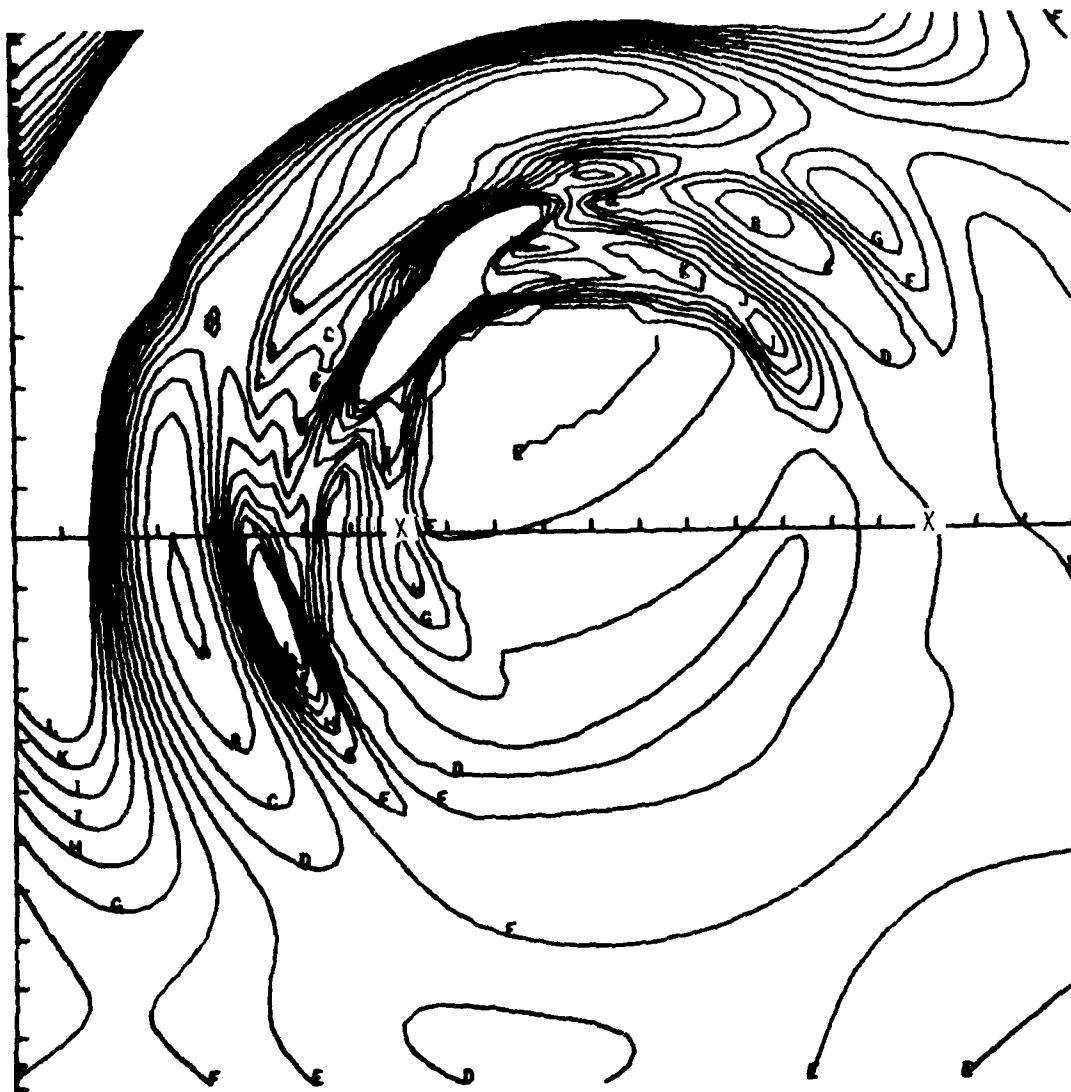
$T = 60 \text{ min}$

Figure 8. (continued)



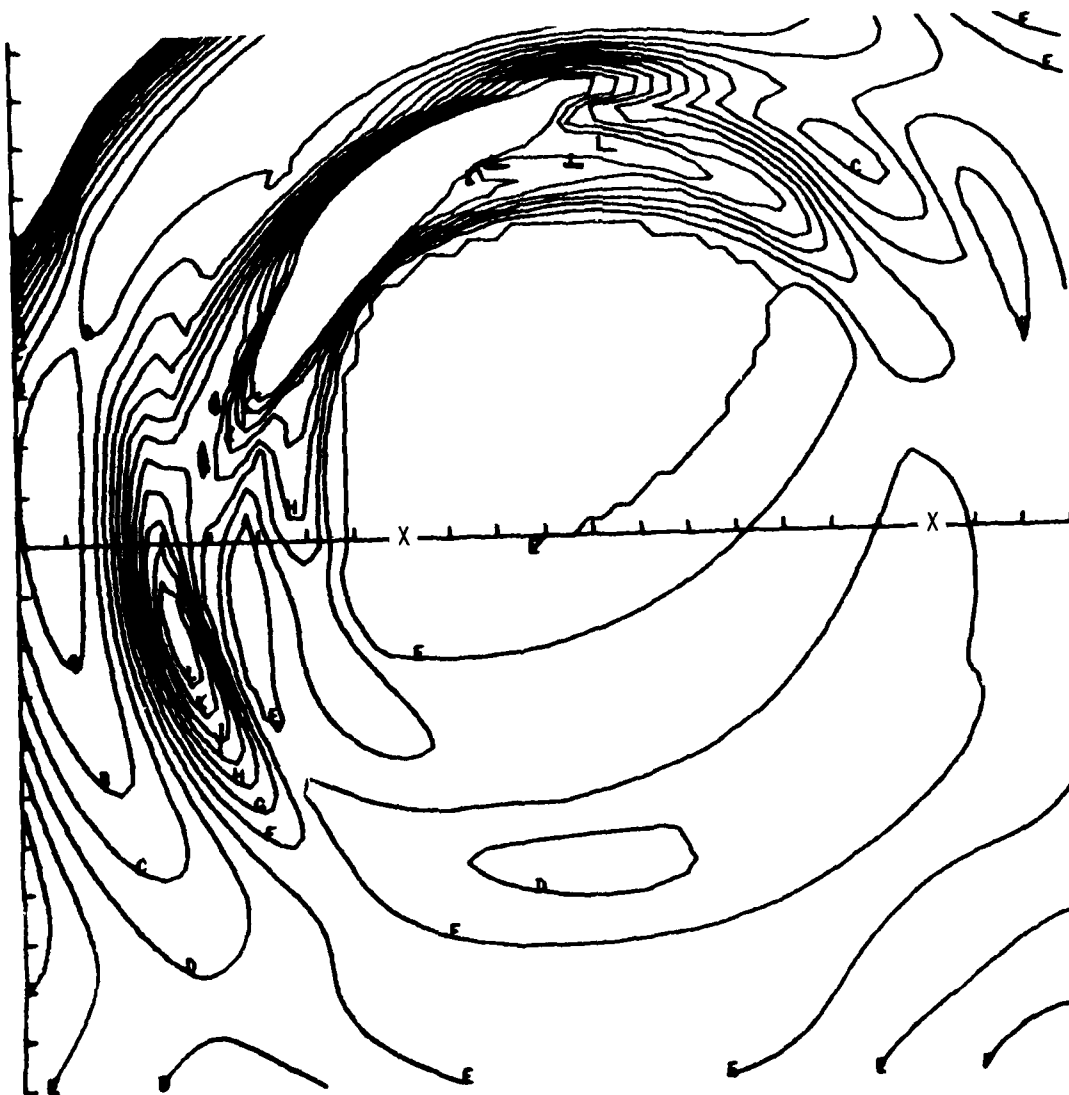
$T = 90 \text{ min}$

Figure 8. (continued)



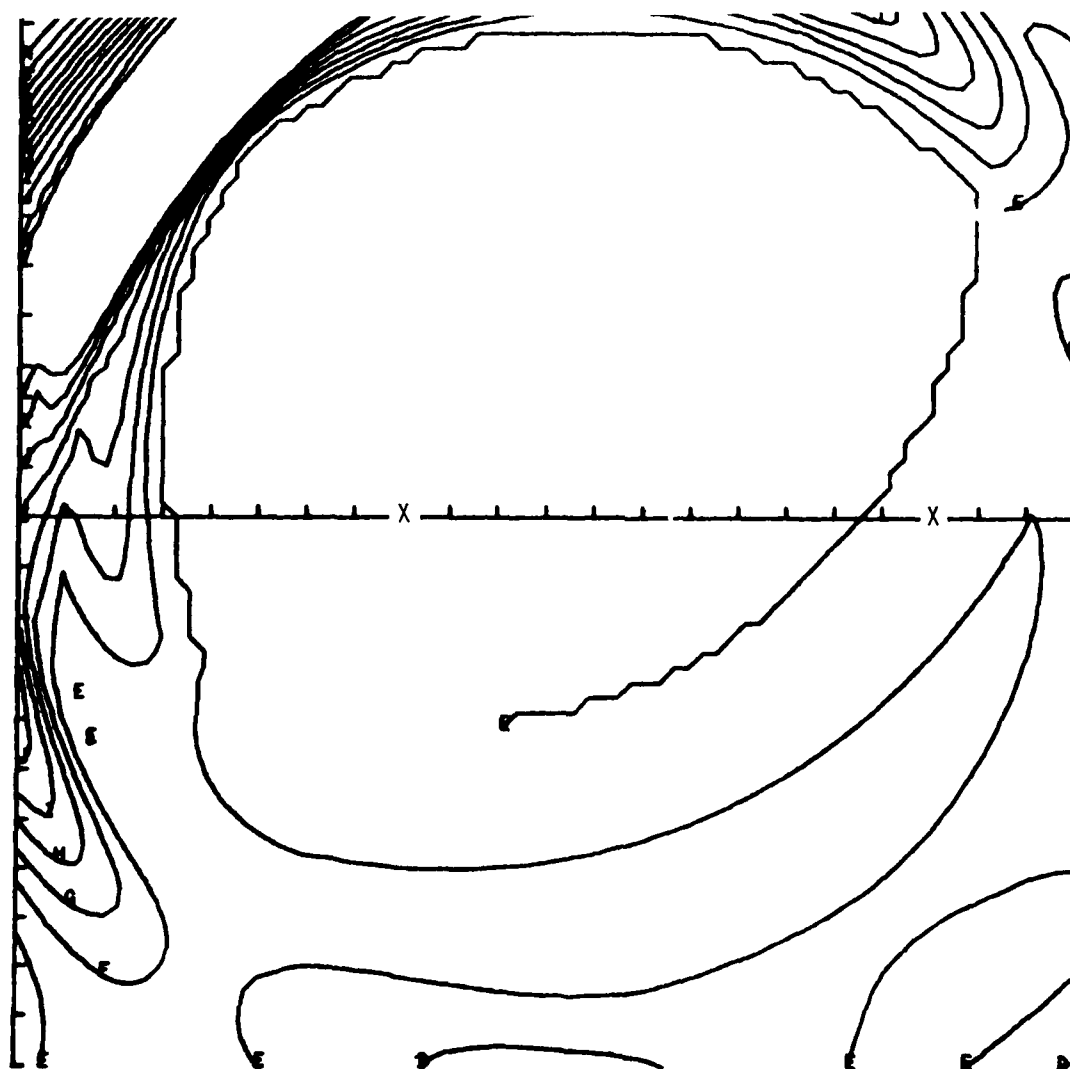
180 min

Figure 8. (continued)



240 min

Figure 8. (continued)



360 min

Figure 8. (continued)

by the necessity to project the spherical surface onto a plane. As before the artificial ionosphere is used and an altitude of 250 km is shown; in this case we have shown the contours in increments of 50 km starting with 50 km so the E contour is the ambient value at 250 km. In Figure 9 we show a vertical slice along the line of the HF link (as above, we use the artificial atmosphere to clarify the results); contours are shown in increments of 50 km starting with 50 km. In Figure 10 we show the same vertical plane as in Figure 9 but in this case we have used a realistic ionosphere, taken from Reference 7, and we have plotted contours of critical frequency starting with 1 MHz and in increments of 1 MHz. This figure shows the degree of disturbance in the ionosphere for the radio wave propagation.

We note in some of these figures that the model behaves in what may be an unphysical way when the disturbance becomes sufficiently strong. To understand this behavior consider a case where the amplitude of ΔZ at its maximum value at $Z = 300$ km is greater than 200 km. The model would then specify that the material at 300 km came from above 500 km or below 100 km. But the model specifies that the points at 100 km and 500 km do not move (that is, the amplitude of the disturbance goes to zero) thus the model produces a pattern in the ionosphere which cannot be arrived at by smooth, linear, wavelike motions. Close examination of Equation 22 shows that a problem of this type will develop somewhere whenever the amplitude of ΔZ becomes larger than 100 km. The discontinuity in the motion is near 100 km and 500 km where the amplitude of ΔZ is near 100 km and moves nearer 300 km for larger values of the maximum disturbance. We could remove the discontinuity in the underlying motion in various relatively simple ways but so far we have chosen not to do so. One reason is that the electron densities provided by the model are not discontinuous; there exists some motion which would produce the predicted electron densities. Another reason is that the problem occurs only for very violent disturbances such that the linear analysis used to develop the model could not be expected to give an accurate result. For motions large enough to

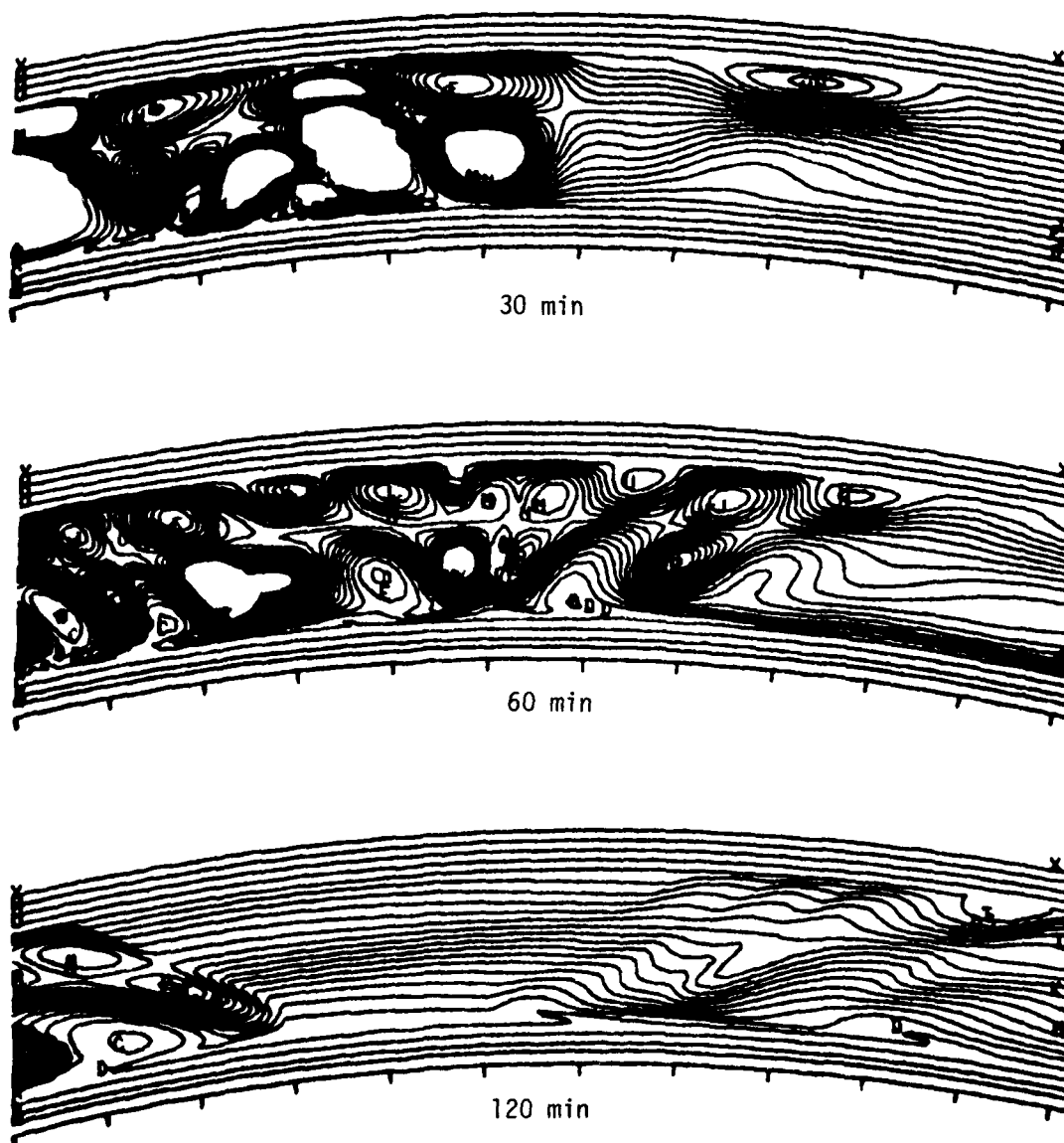


Figure 9. Contours of electron density along the link (for the artificial ionosphere) following the attack. The tic marks are 250 km apart and the contour interval is 50 km.

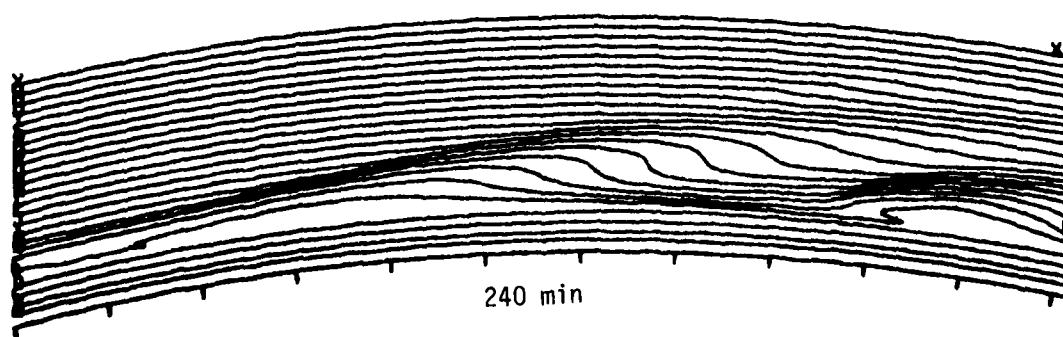
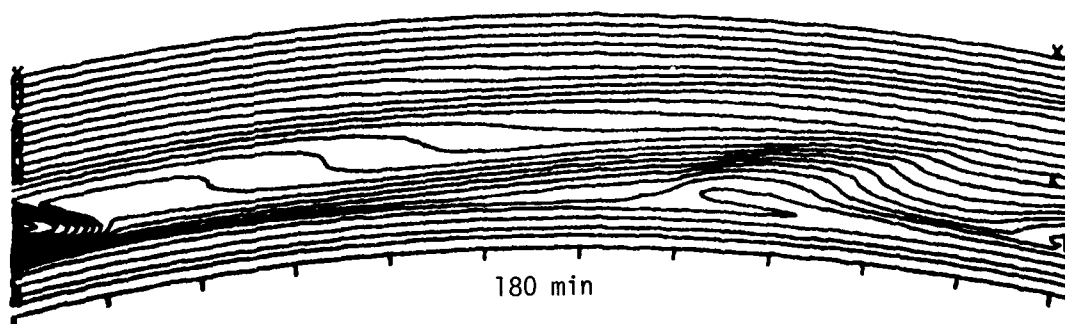
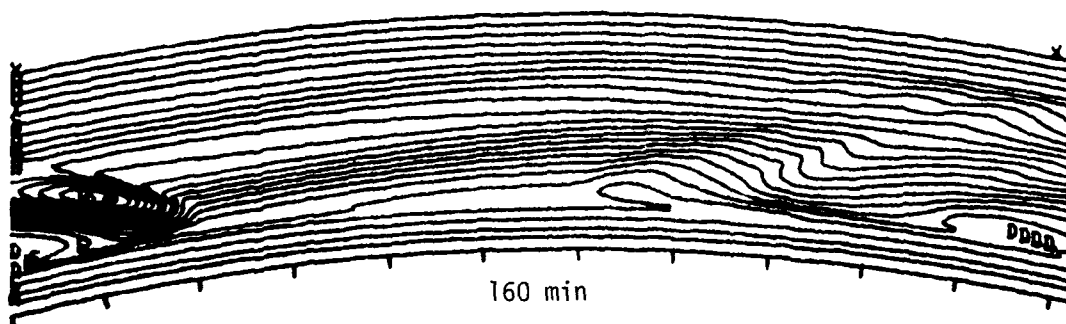


Figure 9. (continued)

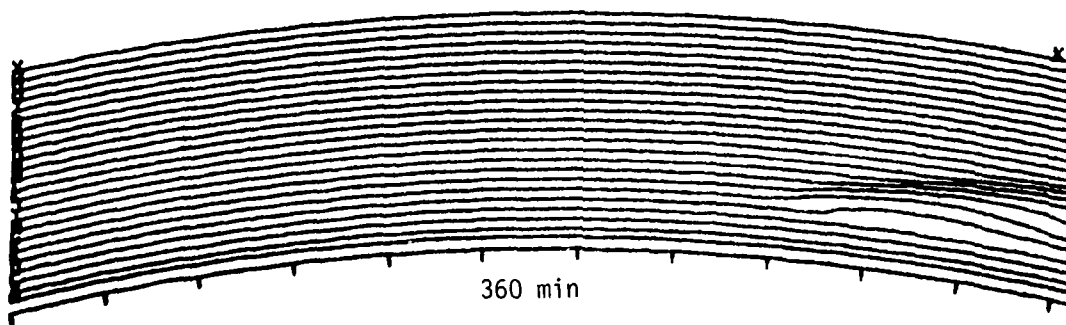
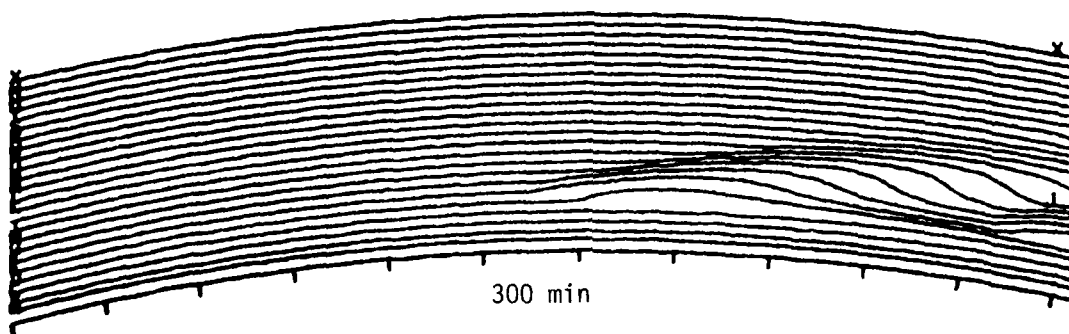


Figure 9. (continued)

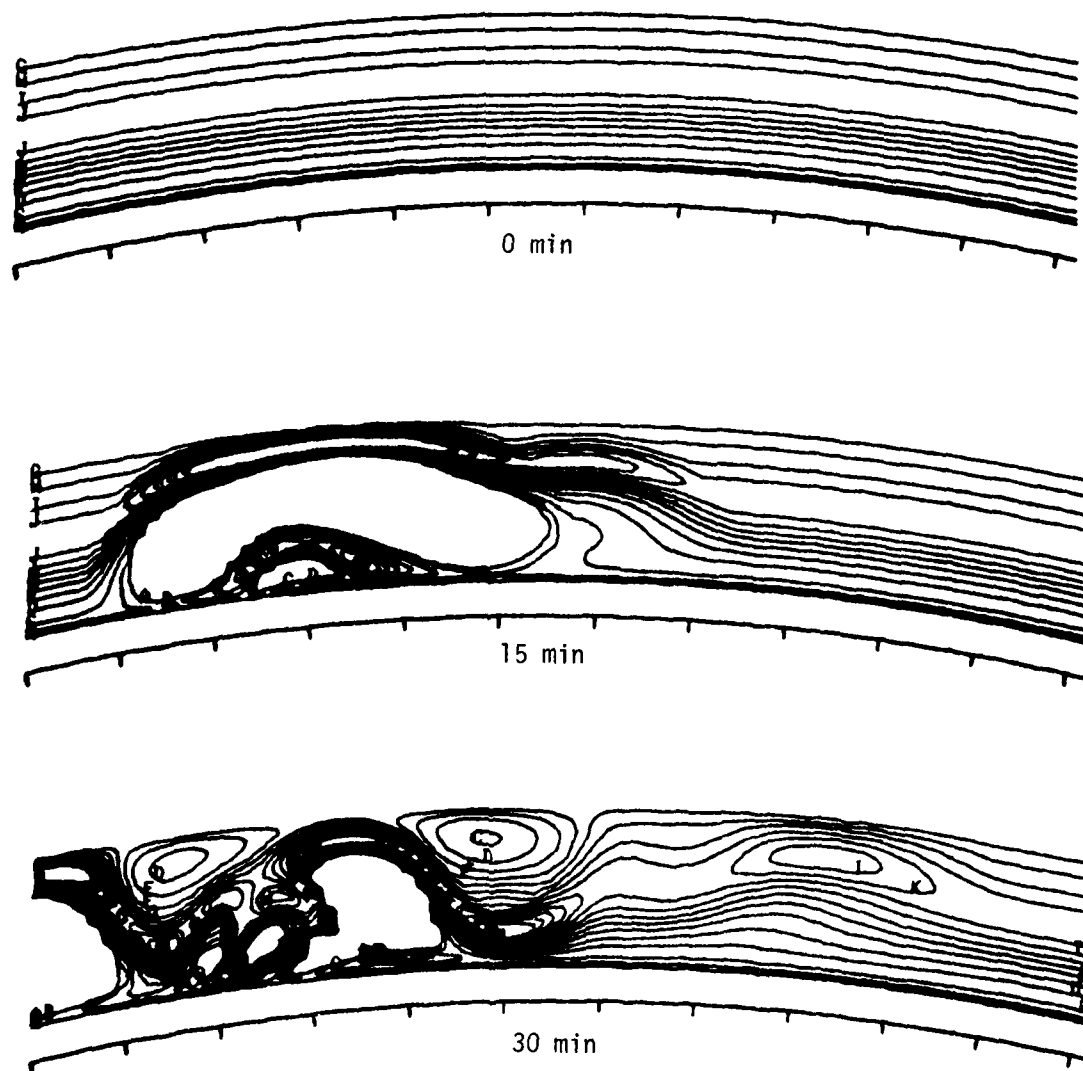


Figure 10. Contours of critical frequency (realistic ionosphere) along the link following the attack. The tic marks are 500 km apart and the contour interval is 1 MHz.

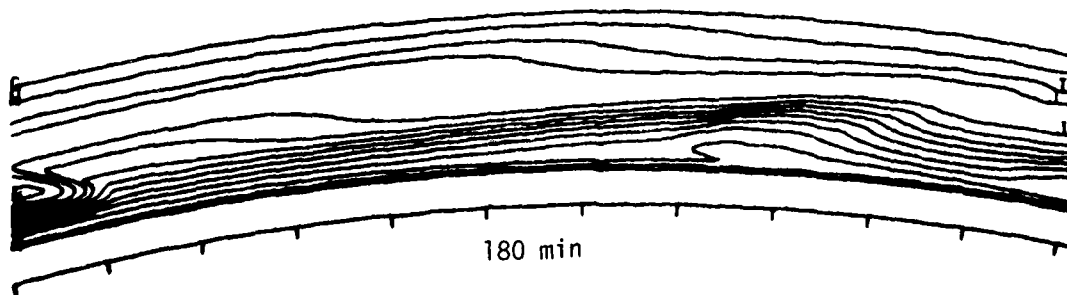
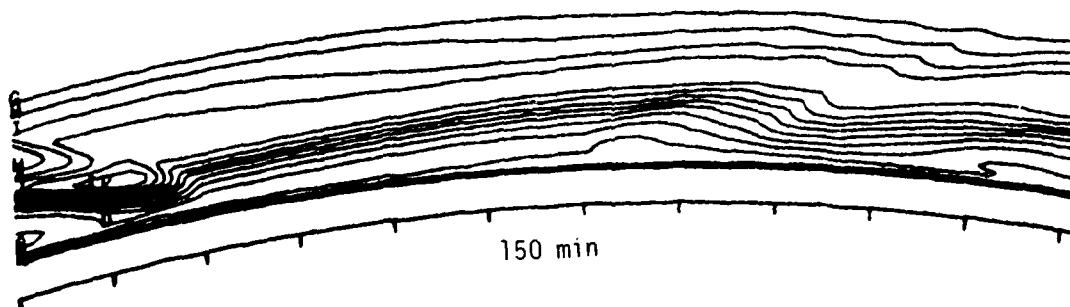
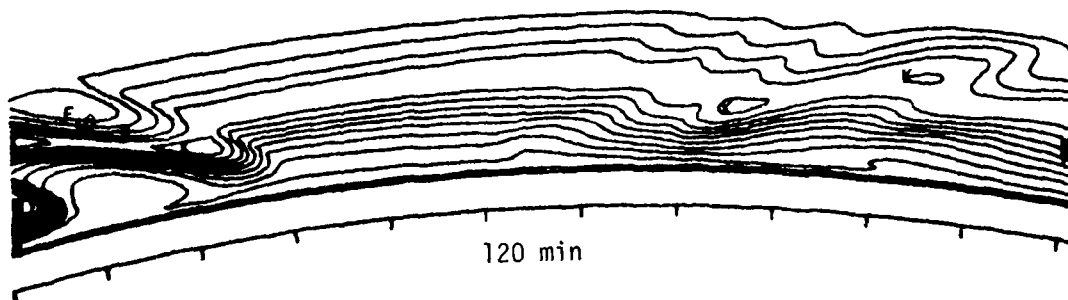
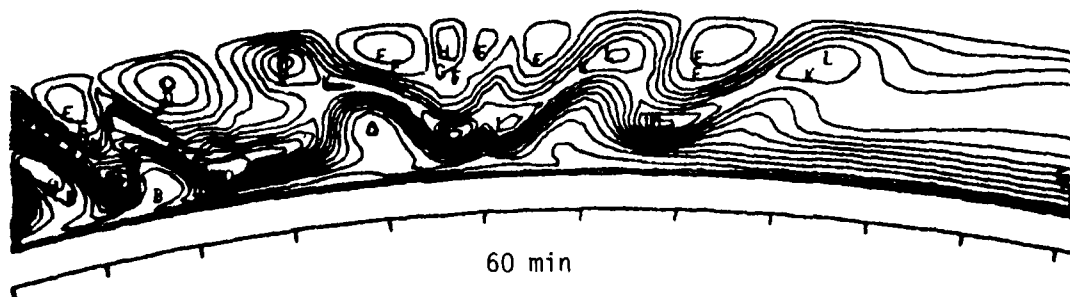


Figure 10. (continued)

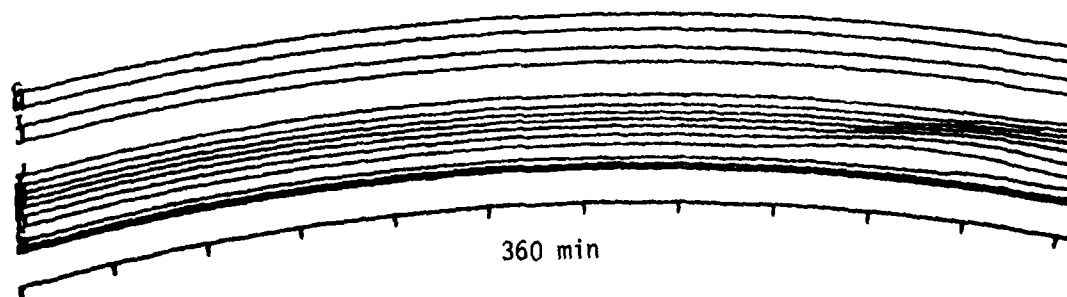
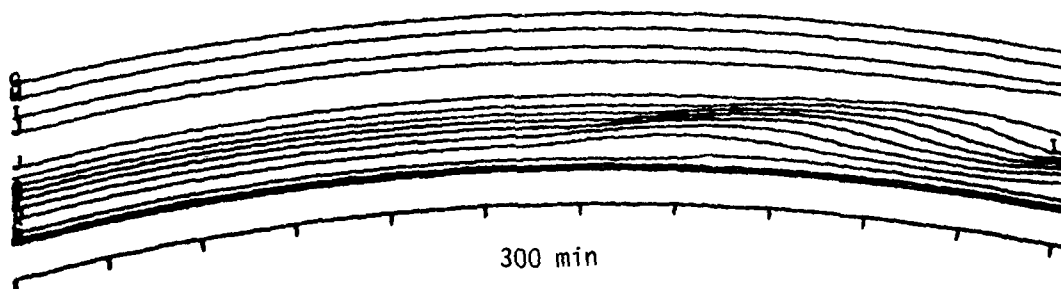
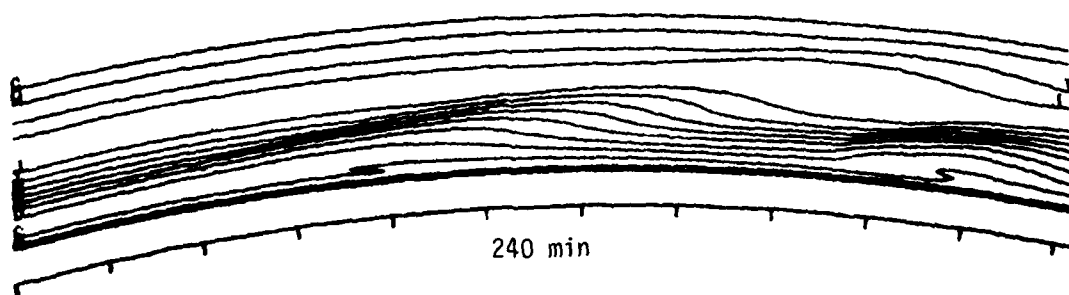


Figure 10. (continued)

produce displacements in the electrons as large as 100 km the flow will probably become turbulent and produce a fragmented ionosphere at least as disturbed as that predicted by the model.

We have traced some rays through the disturbed ionosphere in this model problem. These calculations were made to demonstrate that the gravity wave disturbance produces considerable effects on the propagation of HF radio waves. We have not yet made calculations in enough detail to analyze the expected performance of a system on the proposed link. By tracing rays in the undisturbed ionosphere we found that a 25 MHz ray launched at about 6° elevation would propagate to about 2800 km on a single hop. 15 MHz rays would not propagate to 2800 km on a single hop but for an elevation angle of about 18° two hops propagated to 2800 km. We then ran a few rays in the very disturbed environment at 60 minutes. The 15 MHz rays launched near 18° elevation all came to earth behind and to the left of the transmitter. We made no further calculations at 15 MHz at 60 minutes. The 25 MHz ray launched at 6° elevation went only 1700 km, and no ray launched along the line of the link went more than 2765 km. Rays launched near 1° elevation and somewhat to the right of the intended receiver did land in the region around 2800 km along the link. Whether this is the only launch angle to arrive at this point we do not know, but we did notice an interesting phenomena at about 2400 km. In Figure 11 we show the landing point, of two different bundles of rays. Figure 11a shows a bundle centered at a launch elevation of 2.70° and a launch azimuth of 325.50° . In Figure 11b we show the bundle centered at a launch elevation angle of 7.93° and a launch azimuth angle of 324.90° . In each plot the x in the center is the same point some 2400 km along the path shown by the line in Figure 7. As some sort of comparison we show, in Figure 11c, the landing points of the bundle of rays at the lower launch elevation angle for the ambient ionosphere. The center of the plot must, of course, be different but a comparison of the patterns of Figure 11c with those of Figures 11a and 11b shows the extreme distortion in the ray paths produced by the gravity wave. While we have not been able to analyze the signal at the location of the

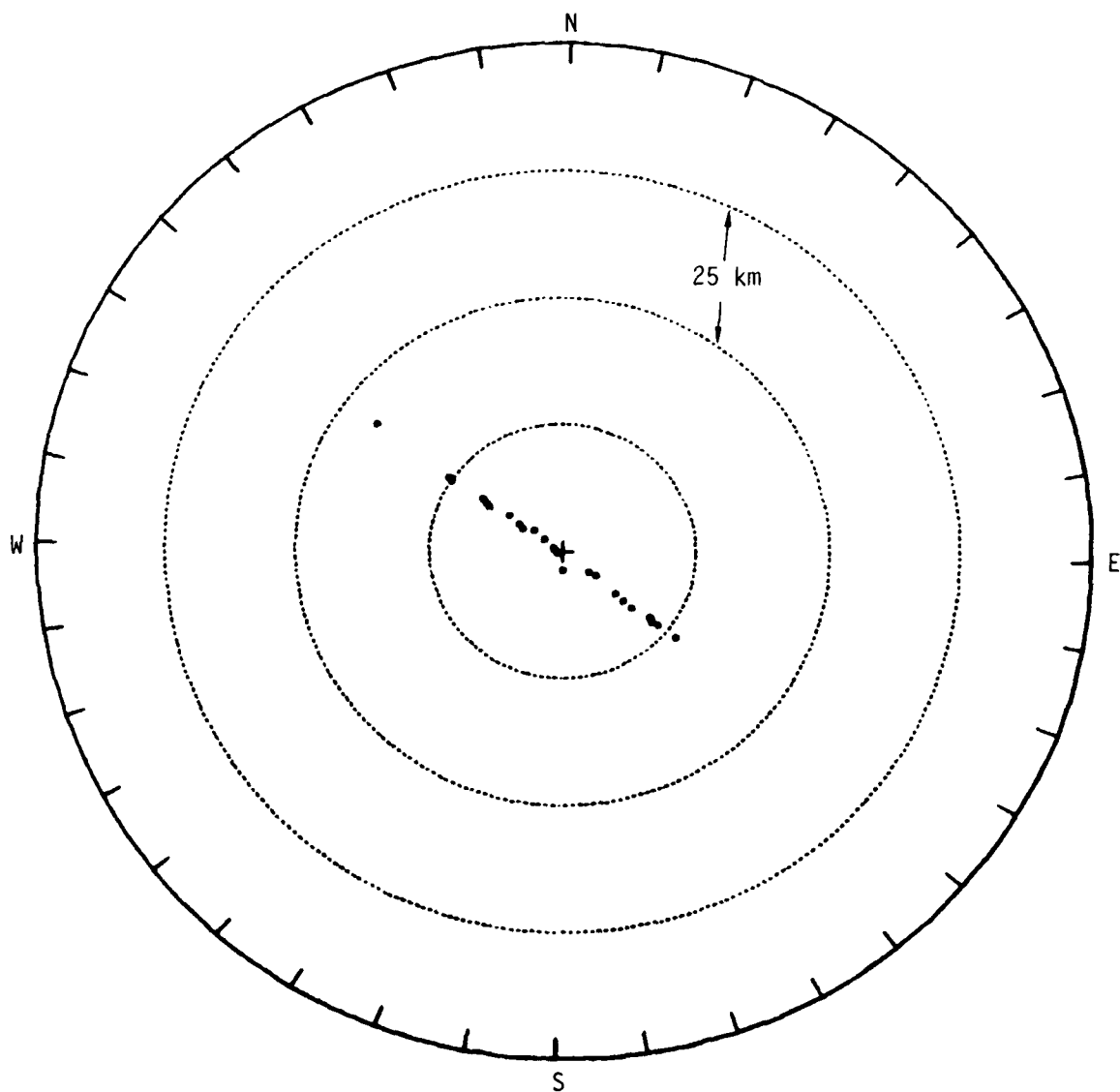


Figure 11a. The landing points for a bundle of 25 MHz rays launched at about 2.70° elevation 60 minutes after the attack. The radius of the figure is 100 km with 25 km between rings.

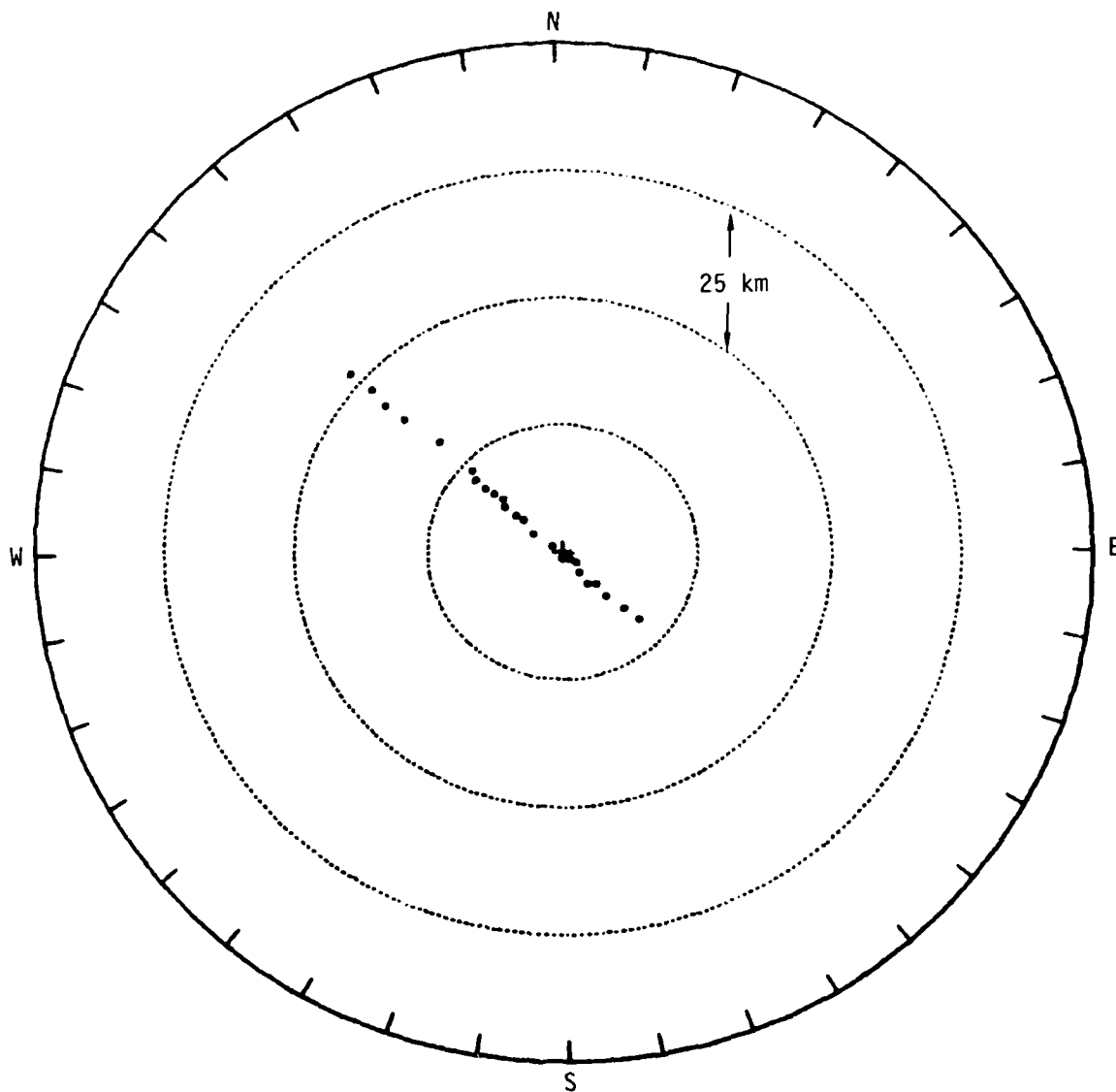


Figure 11b. The landing points for a bundle of 25 MHz rays launched at about 7.93° elevation angle 60 minutes after the attack.

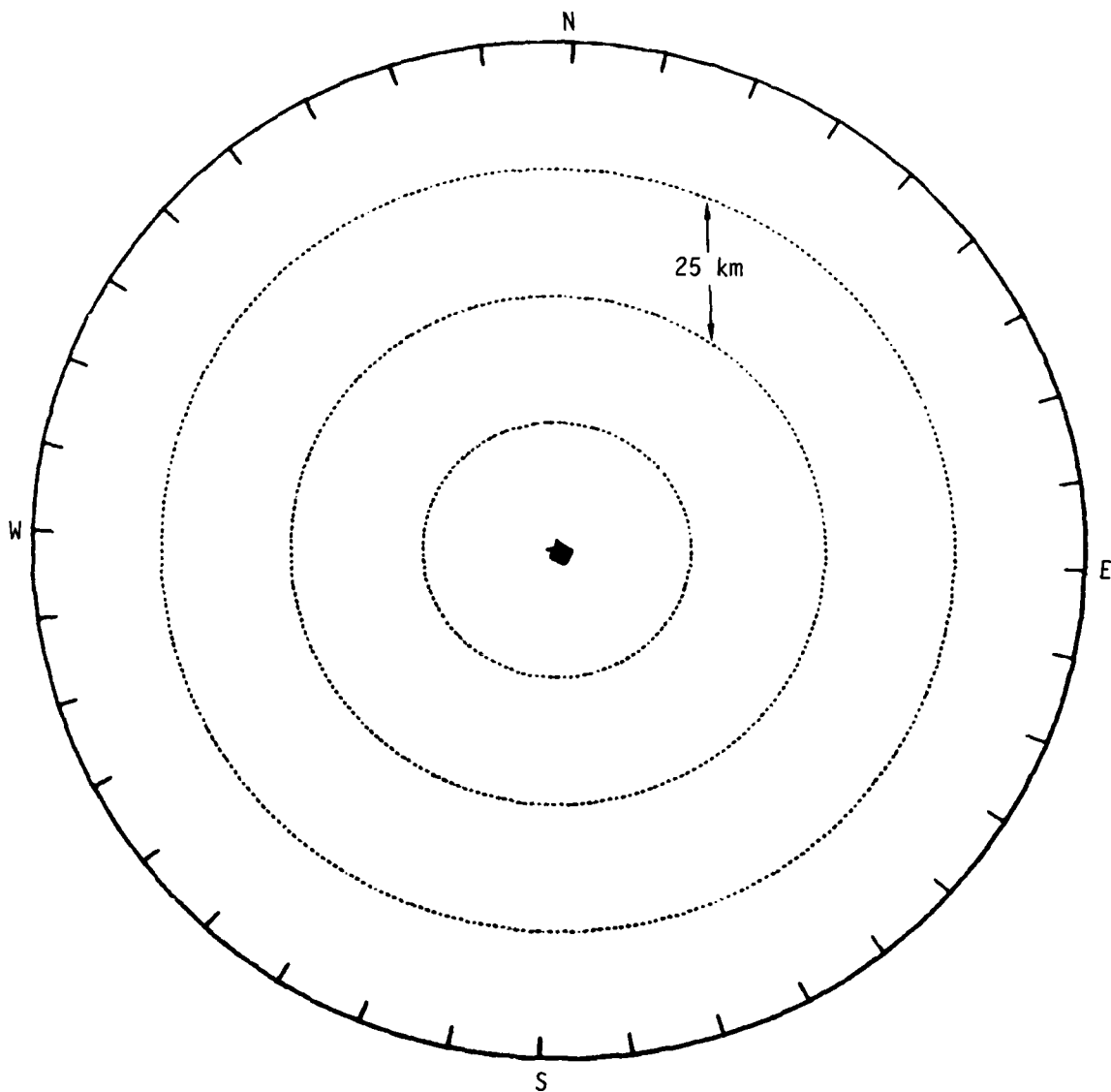


Figure 11c. The landing points for the 2.70° ray bundle for the ambient atmosphere.

center of Figures 11a and 11b in this report, it appears likely that a multi-path problem may be present for some systems.

We now consider the time of 240 minutes as shown in Figure 10 and again consider the case of 15 MHz and two hops. We have calculated ray paths for rays launched along the line in Figure 1 and having elevation angles from zero to twenty-five degrees. The rays all land fairly near the direction of launch, up to a few degrees deviation, so we can give some feel for the results by plotting the range vs. the launch angle; this has been done in Figure 12. The transmitted energy is seen to become highly concentrated in the vicinity of 3400 km. It appears that even after 4 hours the gravity wave is causing interesting radio wave phenomena at HF frequencies. It should be possible to perform an analysis of these effects from a systems point of view in the near future.

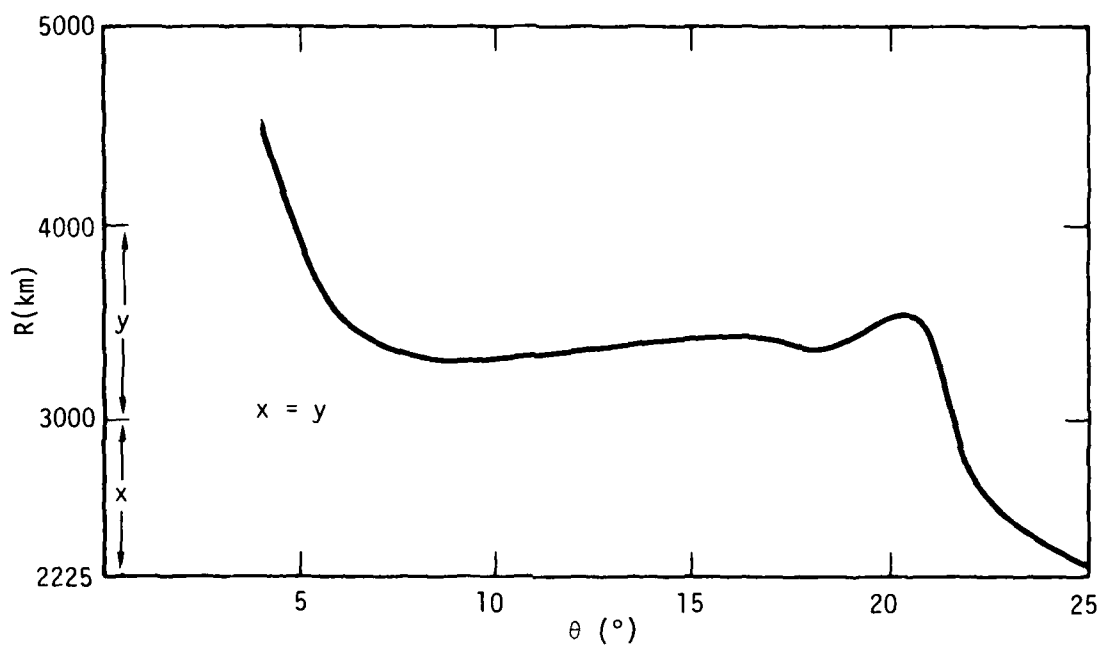


Figure 12. The range to which rays launched at elevation angle θ propagate for 15 MHz, two hops, for the 240 minute environment.

SECTION 5 CONCLUSIONS

In this report we have described a model which gives the ionospheric effects of the gravity waves produced by low altitude nuclear explosions. For large distances from the burst the model is based largely on data; for the region near the burst the model is based entirely on calculations. The model is described by a single set of equations, however, and is thus continuous with no "switch points" which might lead to anomalous behavior. The gravity wave model has been programmed into a ray trace computer code giving us the ability to analyze the changes the disturbed ionosphere produces on HF radio waves.

The gravity wave effects can be quite severe in the case of a large nuclear attack and strong effects last for periods of several hours. In the present work we have been able to do only a few example calculations. These examples confirm that the gravity wave model produces significant ionospheric distortions, as expected, that the ray trace codes can calculate the raypaths through the distorted ionosphere, and that the gravity wave phenomenon severely distorts the raypaths for times up to at least several hours after a nuclear attack.

REFERENCES

1. A general review of AGW is S. H. Francis, Theory and Models of Atmospheric Disturbances, Bell Laboratories, October 1973.
2. Hines, C. O., "On the Nature of Traveling Ionospheric Disturbances Launched by Low-Altitude Nuclear Explosions," J. Geophys. Res. 72, 1877 (1967).
3. Francis, S. H., "Propagation of Internal Acoustic-Gravity Waves Around a Spherical Earth," J. Geophys. Res. 77, 4221 (1972).
4. Kanellakos, D. P., "Response of the Ionosphere to the Passage of Acoustic-Gravity Waves Generated by Low-Altitude Nuclear Explosions," J. Geophys. Res., 72, 4559 (1967).
5. Longmire, C. L., G. McCartor, and W. Wortman, Ionospheric Effects and Energy Loss from the Blast Wave from Low-Altitude Nuclear Bursts, DNA 3494T, Mission Research Corporation, October 1974.
6. Hankrider, D. G., "Theoretical and Observed Acoustic-Gravity Waves from Explosive Sources in the Atmosphere," J. Geophys. Res. 69, 5295 (1964).
7. Knapp, W. S., and K. Schwartz, Aids for the Study of Electromagnetic Blackout, DNA 3499H, General Electric Company—TEMPO, February 1975.

APPENDIX A
(Taken from DNA 3494T)
SHOCK WAVE IN THE ATMOSPHERE

DECAY OF THE BLAST WAVE

After a nuclear explosion a substantial portion of the yield, perhaps 30%, is lost from the region immediately around the burst by radiation and, except for some heating in the air, plays no further role in the hydrodynamic effects which follow. The remaining energy is chiefly internal energy in the high temperature fireball which is approximately an isothermal sphere. As this sphere rapidly expands it drives a very strong blast wave ahead of it. As a consequence the original internal energy of the small hot region is converted partly to the energy of the blast wave, while the remainder is in the internal energy of the fireball which has expanded to pressure equilibrium. To get an estimate of the fractions involved consider a small hot region of ideal gas of density ρ and pressure P which adiabatically expands to a new state ρ' , P' with adiabatic exponent γ . If the region contains mass M , then the original and final internal energies are

$$E = M \cdot \frac{P}{(\gamma-1)\rho} \quad \text{and} \quad E' = M \cdot \frac{P'}{(\gamma-1)\rho'} \quad . \quad (A-1)$$

By the adiabatic condition

$$(P/\rho) \rho^{(1-\gamma)} = (P'/\rho') (\rho')^{(1-\gamma)} \quad (A-2)$$

so

$$E'/E = (\rho'/\rho)^{\gamma-1} \quad . \quad (A-3)$$

A typical case of interest might be $\gamma \approx 1.3$ and $\rho'/\rho \approx 1/20$ which gives $E'/E \approx 1/3$. That is, 2/3 of the original internal energy would be transferred to the blast wave. Consequently, perhaps 50% of the yield resides in the strong blast wave. This energy is deposited in the region through which it passes and it is of considerable interest to know just where and how this deposition occurs. In order to shed some light on this question, let us consider first the more accessible question of how the pressure of the blast wave declines with distance.

Pressure Decline

For the case of a point explosion there exists an analytical solution for the complete flow field if the external pressure is negligible compared with the shock pressure. The pressure at the shock¹ is given by

$$P_s = \frac{8}{25(\gamma+1)} \frac{E_0}{K(\gamma)} R^{-3} \quad (A-4)$$

where

$$K(\gamma) = \frac{64\pi}{75(\gamma^2-1)} \int_0^1 \left(\frac{1+\theta}{2} \right)^{11/5} \left(\frac{\theta+\gamma}{\gamma+1} \right)^{-\frac{4\gamma}{3\gamma-1}} \cdot \left[\frac{3(2-\gamma)\theta+2\gamma+1}{7-\gamma} \right] \frac{13\gamma^2-7\gamma+12}{5(2-\gamma)(3\gamma-1)} \left(\frac{d(F^3)}{d\theta} \right) d\theta$$

with

$$F = \theta^{\frac{\gamma-1}{2\gamma+1}} \left(\frac{1+\theta}{2} \right)^{-2/5} \left(\frac{\theta+\gamma}{\gamma+1} \right)^{\frac{\gamma+1}{3\gamma-1}} \cdot \left[\frac{3(2-\gamma)\theta+2\gamma+1}{7-\gamma} \right]^{-\frac{13\gamma^2-7\gamma+12}{5(2\gamma+1)(3\gamma-1)}} \quad (A-5)$$

which is the order of 1 for $\gamma = 1.3$. E_0 is the energy. Since $P \propto R^{-3}$, it is apparent that the sphere functions as a unit and the shock will not be able to run away and leave a detached inner region. In a realistic case the strong shock condition must eventually cease to be satisfied due to the finite pressure P_0 of the ambient medium. Still later when the shock weakens to the acoustic level the result should become the usual acoustic form

$$P_s = P_0 + \alpha/R. \quad (A-6)$$

The transition between these two forms is of course described by hydrodynamics although no analytic solution exists. Brode² has made a study of this question by use of a finite difference numerical method and the resulting pressure versus range curve is shown in Figure 1. The initial values for Brode's calculation were taken from the analytic point source solution with a dimensionless length unit of

$$\lambda_s = R_s / \left(\frac{E_{TOT}}{P_0} \right)^{1/3} \quad (A-7)$$

where R_s is the shock radius, E_{TOT} the yield, and P_0 the ambient pressure. As expected there is a R^{-3} behavior until the shock pressure ceases to be much larger than ambient.

Measurements of overpressure versus range have been made at most of the U.S. nuclear tests. In order to compare such results with calculations it is necessary to suitably scale the data taking into account the yield, altitude and physical surroundings of the bursts. This will be done in the usual way. In particular, suppose a measurement was made from a burst with yield Y , ambient pressure P_0 , density ρ_0 , and sound speed c_0 , and determined a pressure P , density ρ , or velocity u , radius R at time t . Then the scaling laws indicate that values

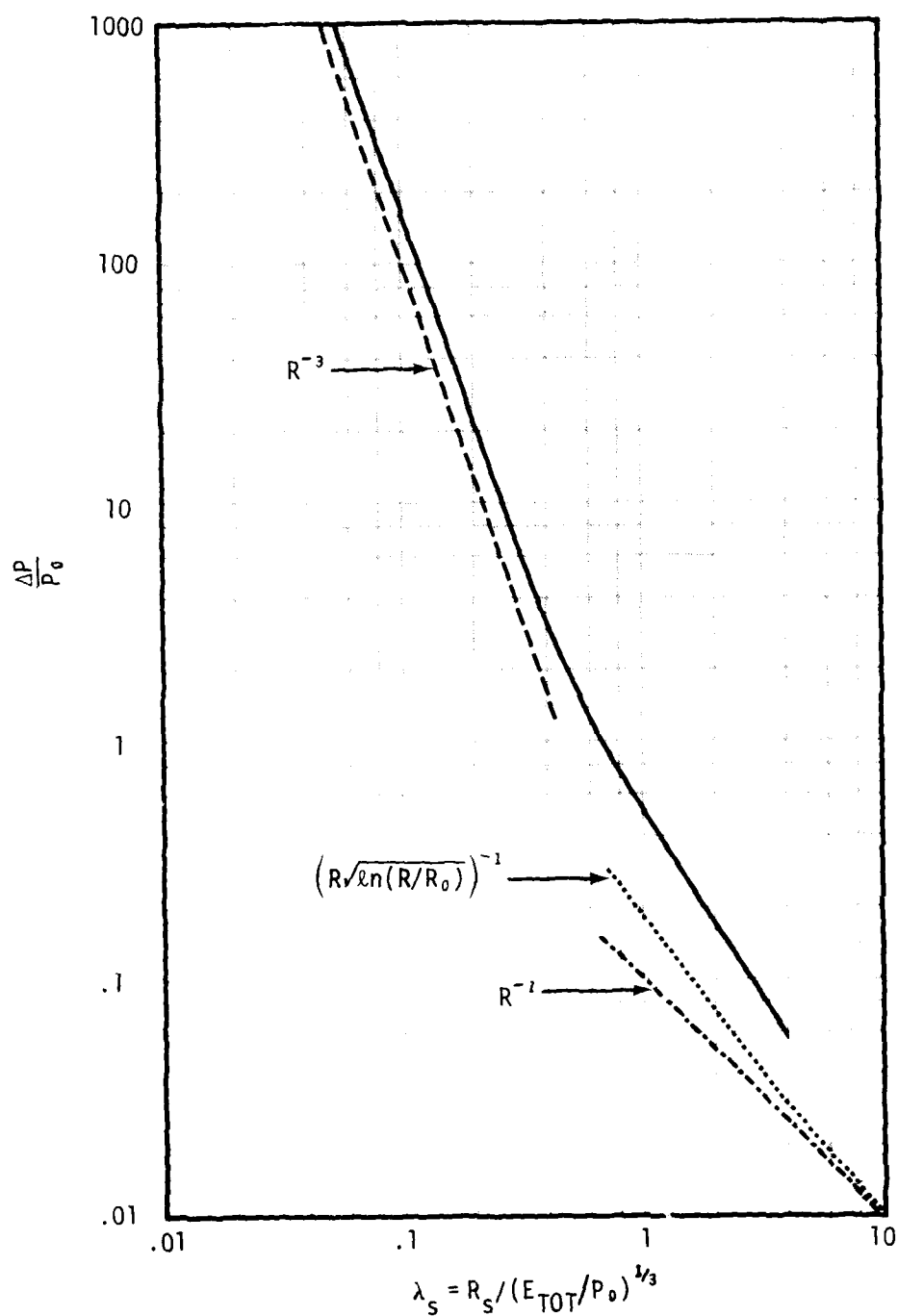


Figure A-1. Relative Overpressure versus Range from Brode. Slopes for Point Source, Semi-Acoustic, and Acoustic Limits are Shown.

$$\left. \begin{aligned} P' &= P_0' \left(\frac{P}{P_0} \right) \\ u' &= c_0' \left(\frac{u}{c_0} \right) \\ \rho' &= \rho_0' \left(\frac{\rho}{\rho_0} \right) \end{aligned} \right\} \quad (A-8)$$

will be found at

$$\left. \begin{aligned} R' &= \lambda R \\ \text{and} \quad t' &= \left(\frac{c_0}{c_0'} \right) \lambda t \\ \text{where} \quad \lambda &= \left(\frac{\epsilon' Y' P_0}{P_0' \epsilon Y} \right)^{1/3} \end{aligned} \right\} \quad (A-9)$$

for conditions indicated by a new set of parameters indicated by primes.
Here ϵ is a parameter indicating the surroundings of the burst

$$\epsilon = \begin{cases} 2 & \text{burst over water} \\ 1.5 & \text{burst over land} \\ 1 & \text{free air burst} \end{cases} \quad (A-10)$$

Data from a large number of US tests, scaled to 1 kiloton TNT equivalent (1 KT $\equiv 4.185 \times 10^{19}$ ergs), are shown on Figure 2. The results of the finite difference calculation appropriately scaled ($E_{\text{TOTAL}} = 1$ KT) are also shown and the agreement is excellent. Much of the data for low overpressures is not very good in that it comes from high yield bursts and so corresponds to measurements taken near the ground after the blast wave has traveled a very great distance. This would introduce ground effects and variations with local conditions. For example $\Delta P/P_0 = .05$ for a yield of 1 Megaton (MT) at sea level occurs at a distance of about 20 kilometers.

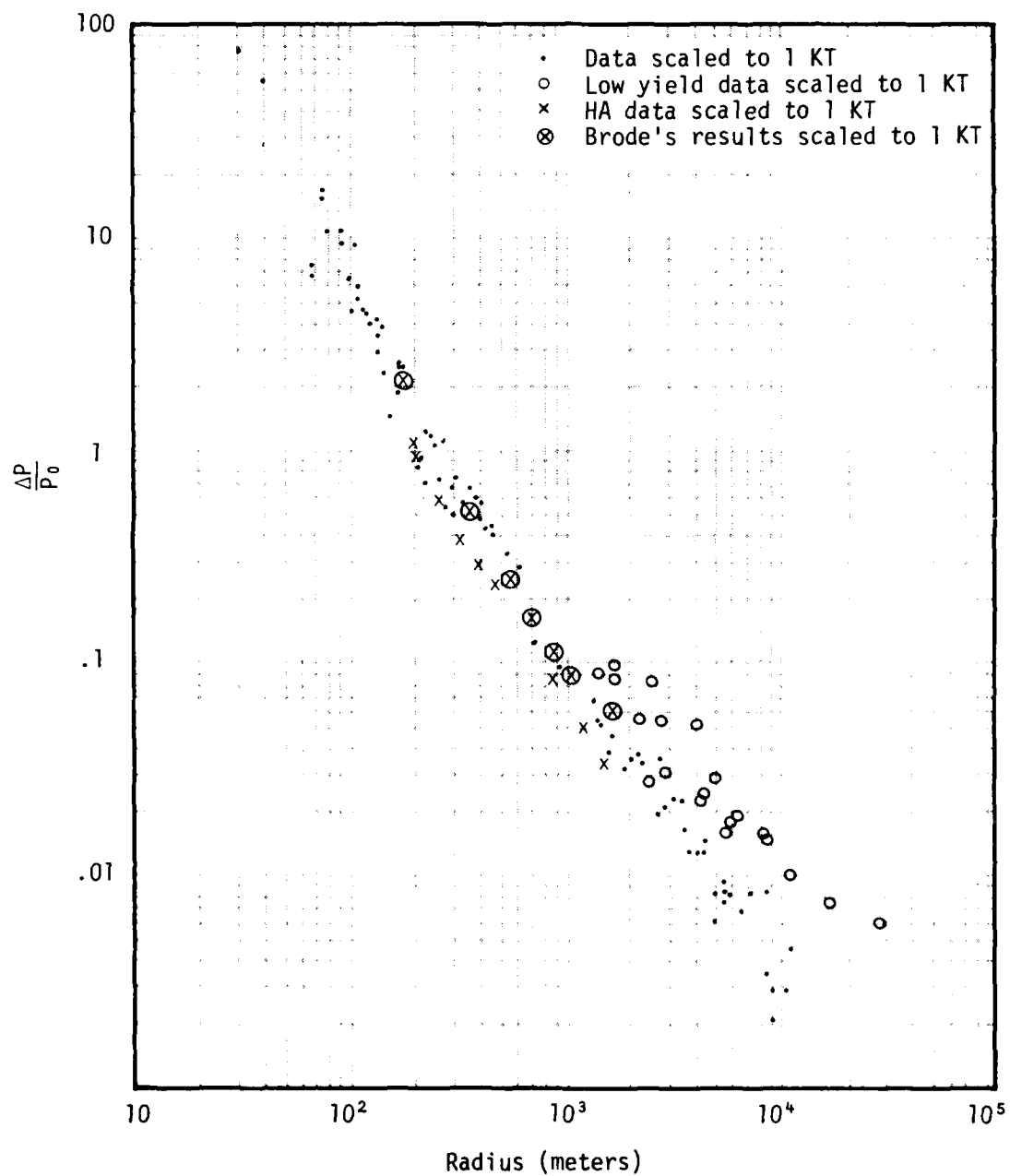


Figure A-2. Pressure versus Range for Test Data Scaled to 1 KT.

Acoustic theory predicts that $\Delta P/P_0 \sim R^{-1}$ for large R . However this corresponds to assuming that no energy is lost from the pulse which is not true. Bethe has developed a semi-acoustic theory in which lowest order non-linear corrections are introduced in the acoustic equations and the lowest order entropy gain term is taken from the Hugoniot shock conditions. Assuming that the shape of the pulse is constant, Bethe¹ was able to show that for spherical symmetry the asymptotic form is

$$\Delta P/P_0 \sim \left(R \sqrt{\ln(R/R_0)} \right)^{-1} . \quad (A-11)$$

Such behavior is shown in Figure 1 and it appears that this asymptotic behavior dominates for overpressures less than roughly .05.

As the blast wave moves out away from the region approximated by a strong shock from a point source, the shape of the pulse becomes that of Figure 3. The sequence of changes leading to that shape are shown in Figure 4. Clearly the limiting form can occur only when pulse has an overpressure less than 1. In Figure 5 the speeds corresponding to the pressures of Figure 4 are shown. The particle speed in the pulse behaves much as the pressure. It is to be expected that the shapes of u and P versus r would be similar in that for acoustic theory we know

$$u = (P - P_0)/\rho_0 c_0 \quad (A-12)$$

where ρ_0 is the ambient density and c_0 the sound speed.

There exists a large quantity of data on the positive pulse duration but much of it is of poor quality. The data scaled to 1 KT at sea level are shown on Figure 6. The scatter of the data at the larger radii shown is clearly indicative of the existence of extraneous effects for propagation over long paths. Special attention should be paid to the points

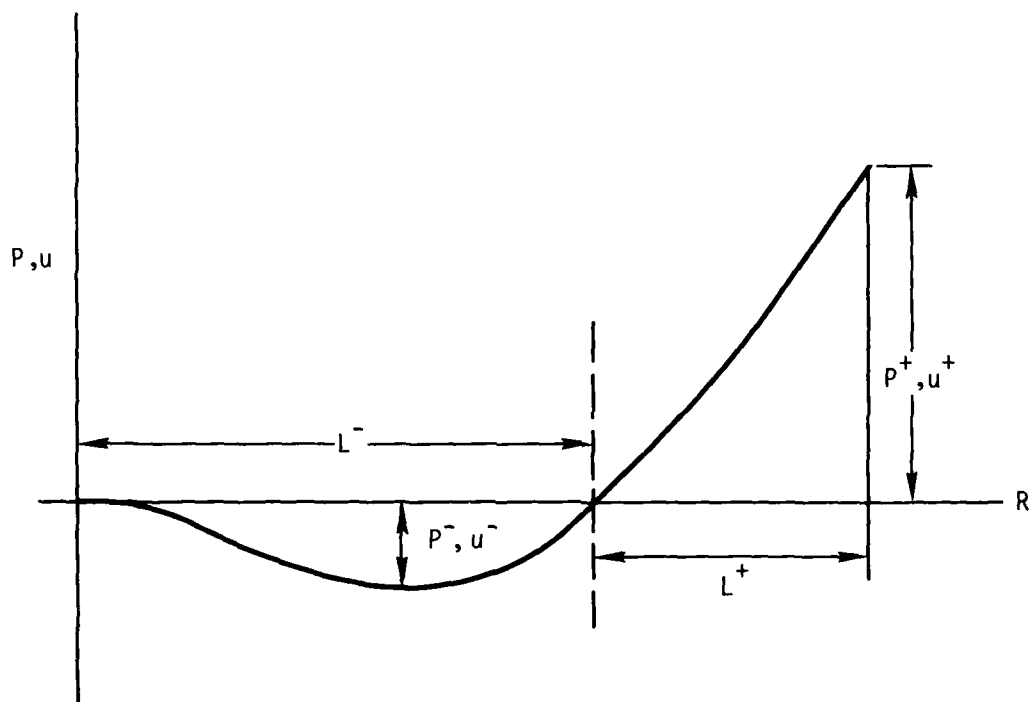


Figure A-3. Shape of Classical Shock Pulse.

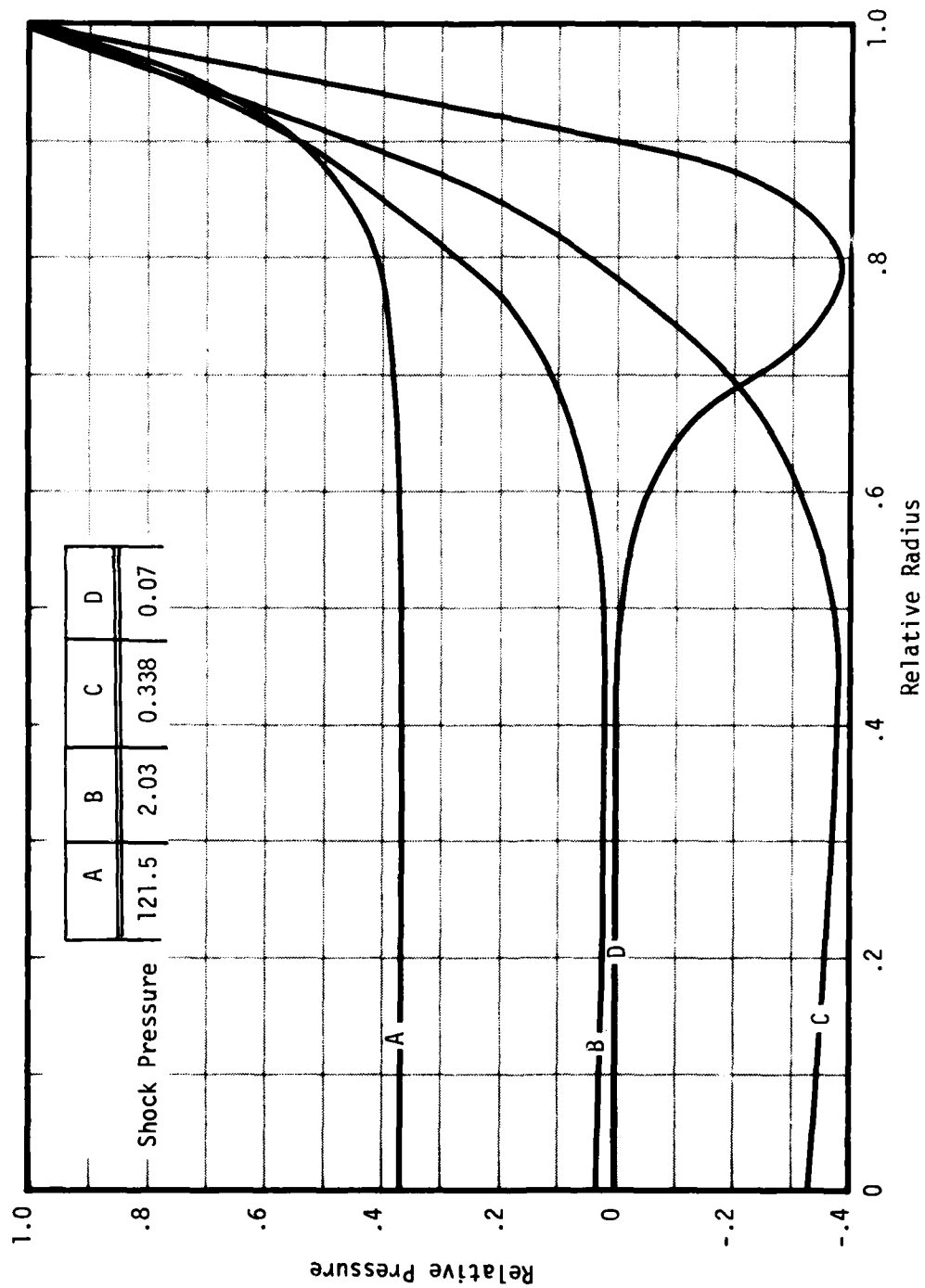


Figure A-4. Development of Pressure Pulse in Brode's Solution. The Variables are Scaled to their Values at the Shock.

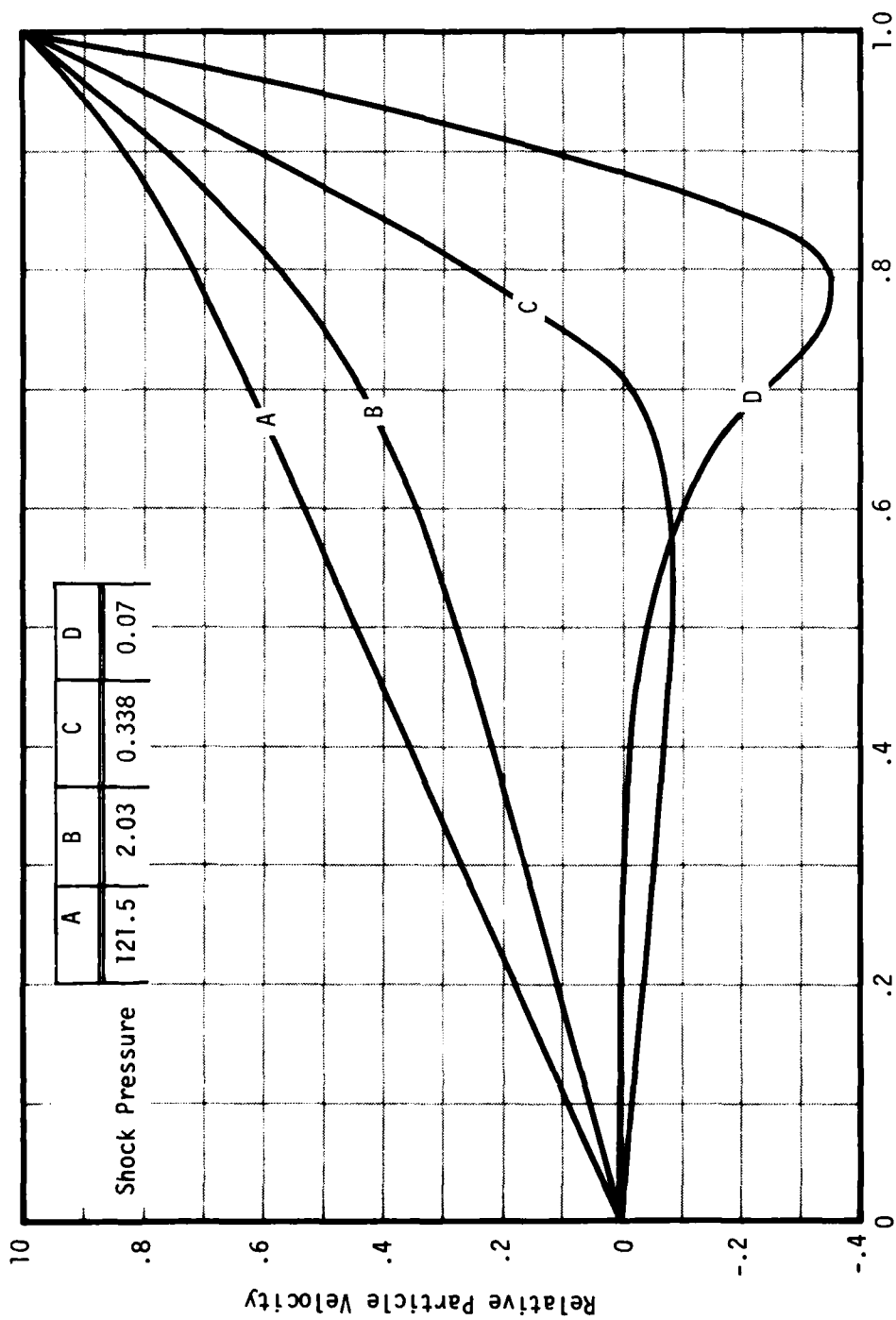


Figure A-5. Development of Particle Velocity in Brode's Solution. The Variables are Scaled to their Values at the Shock.

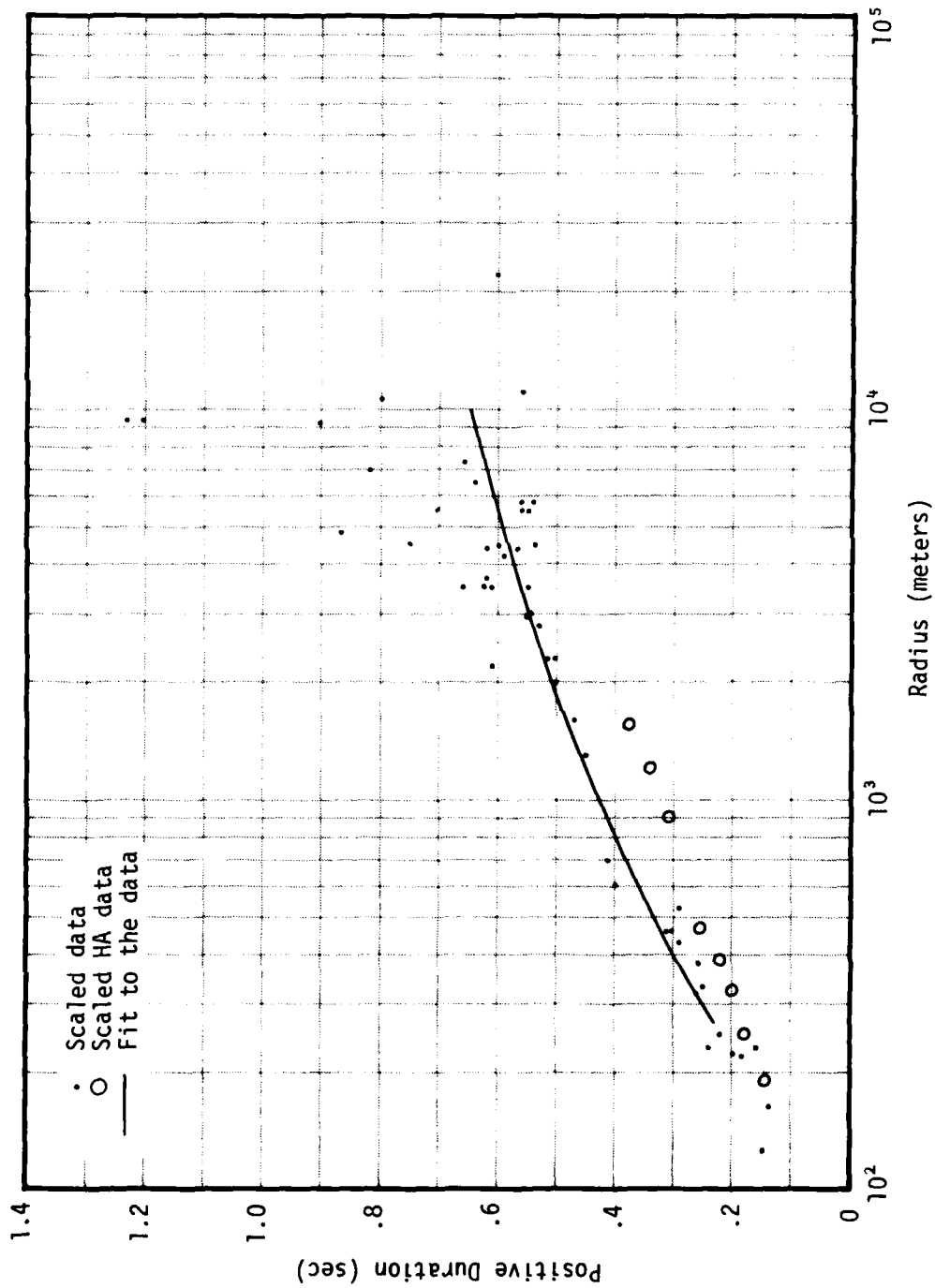


Figure A-6. Positive Pulse Duration versus Radius Scaled to 1 KT for Data and Fit as given in Text.

from shot HA for which the measurements were taken in free air by attaching instrument packages to parachutes which were released near the burst altitude. Note that the points on Figure 2 for the pressure of HA all lie below the fit curve. If the assumed yield was arbitrarily increased from 3 KT by about 70% the pressure points would be brought onto the fit curve. The same change would bring the points for HA on Figure 6 up about 20% and provide a reasonably consistent set of data. The line drawn to provide a fit to the data has been chosen to be of the form

$$D^+(R) = D_0^+ \left[1 + \frac{R_0}{c_0} \frac{(\gamma+1)}{2\gamma} \frac{\left(\frac{\Delta P}{P_0}\right)_0}{D_0^+} \ln(R/R_0) \right]^{\frac{1}{2}} \quad (A-13)$$

which is based on conditions which are discussed in the section, "Model for Propagation".

Energy Decline

The energy in the outward traveling pulse is

$$E = 4\pi \int R^2 dR \frac{[P-P_0]}{(\gamma-1)} + \frac{4\pi}{2} \int R^2 dR \rho u^2, \quad (A-14)$$

which is the sum of the internal energy (IE) and kinetic energy (KE). Since for the acoustic case

$$P-P_0 = \rho c^2 \quad (A-15)$$

it might be supposed that the KE is of lower order than the IE. However, this is not so due to the negative phase of the pulse. In fact for the acoustic case $KE = IE$. For the case of a strong shock it continues to be the case that $KE = IE$ at the front. The Rankine-Hugoniot conditions expressing mass, momentum, and energy conservation across the shock require that for a strong shock,

$$P_s/(\gamma-1) = \frac{1}{2} \rho_s u_s^2 . \quad (A-16)$$

Consequently we will consider that $E = 2 \times KE$ for all our cases.

The energy in the pulse shown in Figure 3 may be approximated as that in the similar linear form. Then

$$\begin{aligned} E &\cong \rho 4\pi R_-^2 \frac{1}{3} (L^-)(u^-)^2 + 4\pi R_+^2 \frac{1}{3} (L^+)(u^+)^2 \rho \\ &\equiv E^- + E^+ \end{aligned} \quad (A-17)$$

Relative dimensions for the pulses in the well developed negative phase region show that

$$P_+ \cong 3P_- \quad \text{or} \quad u_+ \cong 3u_- ,$$

and

$$L_- \cong 2.5 L_+ \quad (A-18)$$

so $E_+/E \cong .78$. Consequently we will hereafter consider only the energy in the positive phase as the energy of the pulse and the general expression used will be

$$E^+ = 4\pi \int_{R_s - L_+}^{R_s} R^2 \rho u^2 dR . \quad (A-19)$$

For the purpose of computing E^+ from data we will presume that the pulse is linear and weak. Then

and

$$\left. \begin{aligned} \Delta P &\cong u \rho_0 c_0, \\ \rho &\cong \rho_0 \quad \text{so} \\ E^+ &\cong \frac{4\pi}{\gamma} \frac{R_s^2}{3} L^+ \left(\frac{\Delta P}{P_0} \right)^2 \end{aligned} \right\} \quad (A-20)$$

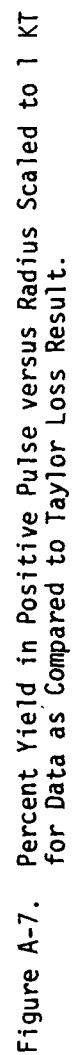
The length of the pulse L^+ is related to the passage time of the pulse Δt by $L^+ \cong c_0 \Delta t$ since the shock is weak and traveling at nearly the sound of speed c_0 . Figure 7 shows the widely scattered data scaled to 1 KT at sea level. Three sets of data taken from the same tests are shown, one being from shot HA with the yield increased by 70% as discussed previously. These sets provide a better feeling for the radial behavior of E_+/E_{TOTAL} when taken individually.

It is apparent that by the time the shock reaches an overpressure of about .05 only 5% of the yield resides in the positive pulse part of the shock. In order to understand this, the mechanism by which energy is lost must be investigated.

The sequence of events which leads to the loss of energy from the pulse is as follows:

1. Material is shocked increasing entropy, density, pressure, and temperature.
2. After passage of the shock the material reexpands, approximately adiabatically.
3. The material finally reaches the original pressure and ceases to expand but it is now at higher than original temperature.
4. Since the pressure is ambient no further expansion occurs and the increased internal energy is no longer available to the shock.

This will be referred to as the Taylor³ loss mechanism.



The increase in internal energy per unit mass will be

$$\Delta I = \frac{P_0}{(\gamma-1)\rho_f} - \frac{P_0}{(\gamma-1)\rho_0} = \frac{P_0}{(\gamma-1)\rho_0} (\rho_0/\rho_f - 1) \quad (A-21)$$

where ρ_f is the final density after reexpansion which is

$$\rho_f = \rho_s \left(\frac{P_0}{P_s} \right)^{\frac{1}{\gamma}}. \quad (A-22)$$

The subscript s denotes values at the shock position. Thus by the Rankine-Hugoniot relations

$$\text{and } \left. \begin{aligned} \rho_s/\rho_0 &= \frac{\gamma+1}{\gamma-1+2/M^2} \\ P_s/P_0 &= 1 + \frac{2\gamma}{\gamma+1} (M^2-1) \end{aligned} \right\} \quad (A-23)$$

where $M = V_s/c_0$ is the Mach number of the shock. The entropy increase per unit mass due to the shock will be

$$\Delta S = \frac{R^*}{\gamma-1} \left[\ln(P_s \rho_s^{-\gamma}) - \ln(P_0 \rho_f^{-\gamma}) \right] \quad (A-24)$$

where $P = \rho R^* T$. Therefore the energy per unit mass which can no longer be available for work will be

$$\begin{aligned} \Delta E_s &= T_0 \Delta S = \frac{\gamma P_0}{(\gamma-1)\rho_0} \ln \left(\left(\frac{P_s}{P_0} \right)^{\frac{1}{\gamma}} \left(\frac{\rho_f}{\rho_s} \right) \right) \\ &= \frac{\gamma P_0}{(\gamma-1)\rho_0} \ln (\rho_0/\rho_f). \end{aligned} \quad (A-25)$$

Since $\rho_0/\rho_f \rightarrow 1$ for weak shock and $\ln(1+\epsilon) \rightarrow \epsilon$ one sees that

$\Delta E_s \cong \gamma \Delta I$ for $\Delta P/P_0 \ll 1$. If one takes this limit it is found that

$$\Delta I \xrightarrow{P_s \rightarrow P_0} \frac{(\gamma+1)}{12 \gamma^3} \frac{P_0}{\rho_0} \left(\frac{P_s - P_0}{P_0} \right)^3 \equiv \Delta I_0 . \quad (A-26)$$

Note that the first two orders do not appear. On Figure 8 $\gamma \Delta I_0$, $\gamma \Delta I$, ΔI , and E_s are plotted. The energy which is lost from the shock will be at least equal to the larger of ΔE_s and ΔI . For shocks that are not too strong say $\frac{\Delta P}{P_0} < 10$, a suitable expression for the rate at which energy is lost from the shock is

$$\frac{dE_{\text{shock}}}{dR} = - 4\pi R^2 \frac{\gamma}{\gamma-1} P_0 \left(\left(\frac{\rho_0}{\rho_s} \right) \left(\frac{P_s}{P_0} \right)^{\frac{1}{\gamma}} - 1 \right) . \quad (A-27)$$

From this one can find the shape of E_{shock} versus R curve given $P_s(R)$. However, there is no firm initial condition with which to normalize this curve. On Figure 7 a set of $E_{\text{shock}}(R)$ curves are given based on $P_s(R)$ from Figure 2. It appears that there is reasonable agreement with the data although the data are poor.

If one assumes a point source solution it is possible to find accurately the energy which is available to the shock. Using Equation (2-27) in conjunction with $P_s(R)$ from the point source solution from Equation (2-4), one finds that,

$$E_{\text{shock}} \Big|_{\substack{P_s = 108. \\ \gamma = 1.2}} = .23 E_{\text{TOTAL}} .$$

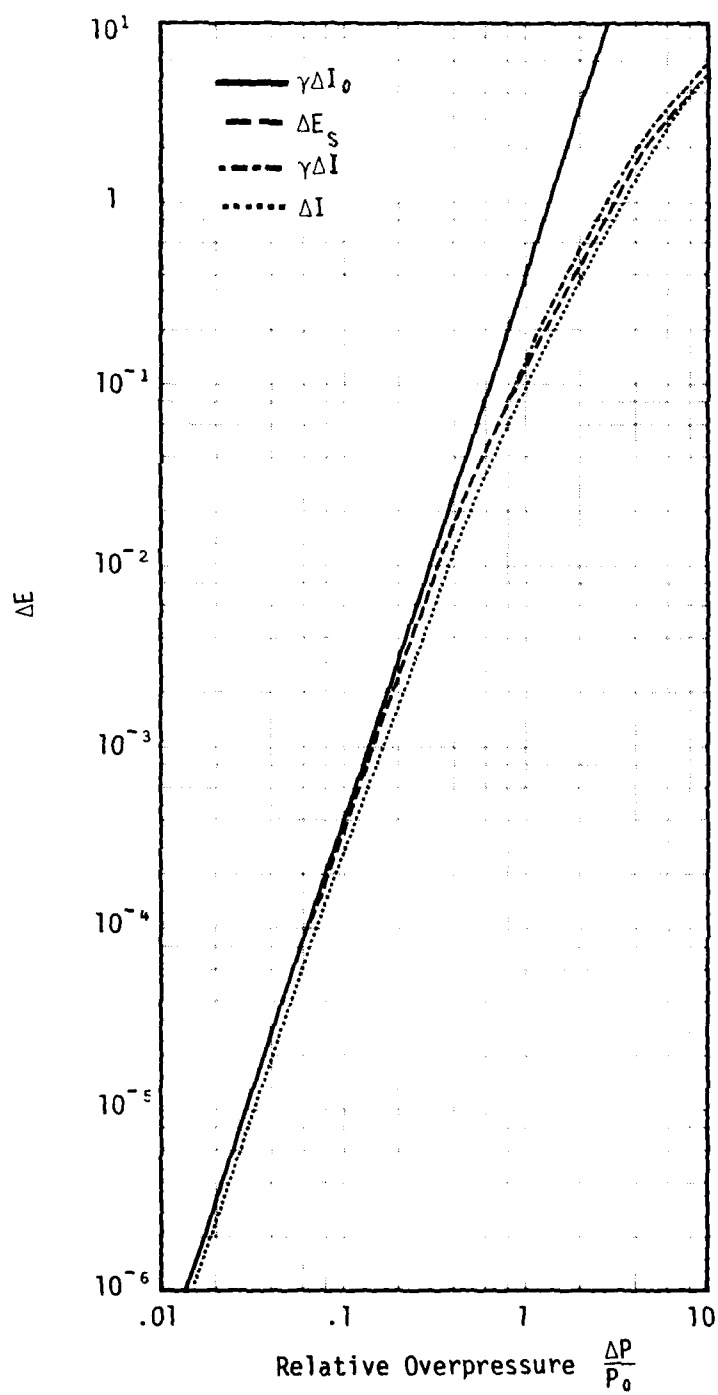


Figure A-8. A Comparison of the Various Energy Loss Formulas of Equations (2-21) to (2-22).

Note that $\gamma = 1.2$ has been used due to the high temperature influence on the equation of state. Such a calculation cannot be taken too seriously because the point source solution is not applicable to a real explosion at early times due to the radiation phase of real explosions.

Still, a value of .23, which would be at about 85 meters on Figure 7, is in the range of the data. Perhaps the energy loss by radiation in the real case is of the same magnitude as the Taylor loss energy for the very strong shock at early times in the point source model. Note that by the point source model $E_{\text{shock}} = .64 E_{\text{TOTAL}}$ whereas for the realistic case $\left. \begin{array}{l} P_s = 1000 P_0 \\ \gamma = 1.2 \end{array} \right\}$

case the radiation phase would still be important allowing energy to be easily transported throughout. Thus some energy which would have been lost from the shock can return to the shock by radiation.

In conclusion it seems certain that the portion of the yield which is in the horizontally outgoing weak shock wave cannot be more than 5% when the pressure has fallen to 5% of ambient. For the region beyond $\Delta P/P_0 = .05$ the pressure $P_s(R)$ appears well described by the semiacoustic result

$$P_s(R) - P_0 = \frac{A}{R \sqrt{\ln(R/R_0)}} \quad (\text{A-28})$$

As a consequence the energy content decreases like $[\ln(R/R_0)]^{-1}$ at large distances.

BEHAVIOR IN A STRATIFIED MEDIUM

Previous discussions were concerned with propagation through an isotropic medium. However, for propagation in the atmosphere this cannot be a suitable description unless the characteristic length $(E_{TOT}/P_0)^{1/3} \ll H$ where H is the scale height. For cases of current interest this condition is not satisfied. Consequently we must consider the effect of the stratified atmosphere on propagation of a shock wave.

Acoustic Propagation

In order to begin to understand such effects, let us consider the propagation of an initially spherical pulse into an isothermal atmosphere which is stable under a constant gravitational force acting in one Cartesian dimension as described in the linearized (acoustic) equations of hydrodynamics.

In general,

$$\left. \begin{aligned} \frac{\partial \vec{V}}{\partial t} + \vec{V} \cdot \nabla \vec{V} &= - \frac{1}{\rho} \nabla P - g \hat{e}_z, \\ \frac{\partial \rho}{\partial t} + \vec{V} \cdot \nabla \rho &= - \rho \nabla \cdot \vec{V}, \text{ and} \\ \frac{\partial P}{\partial t} + \vec{V} \cdot \nabla P &= - \gamma P \nabla \cdot \vec{V}, \end{aligned} \right\} \quad (A-29)$$

where the third equation is equivalent to the adiabatic condition

$$\frac{d}{dt} (P \rho^{-\gamma}) = 0 \quad (A-30)$$

Now for an ideal gas

$$P_0 = \rho_0 R^* T \quad (A-31)$$

so that the steady state unperturbed condition is

$$\left. \begin{aligned} P_0 &= P_{sL} e^{-z/H} \\ \rho_0 &= \rho_{sL} e^{-z/H} \end{aligned} \right\} \quad (A-32)$$

$$\text{where } H = \frac{1}{g} \frac{P_0}{\rho_0} = \frac{1}{g} \frac{P_{sL}}{\rho_{sL}} = \frac{1}{g} R^* T_0 .$$

The linearized equations then give

$$\begin{aligned} \frac{\partial v_r}{\partial t} &= -\frac{1}{\rho_0} \frac{\partial p_1}{\partial r} + \frac{\rho_1}{\rho_0^2} \left(-\frac{\cos \theta}{H} \right) P_0 , \\ \frac{\partial v_\theta}{\partial t} &= -\frac{1}{\rho_0} \frac{1}{r} \frac{\partial p_1}{\partial \theta} + \frac{\rho_1}{\rho_0^2} \frac{\sin \theta}{H} P_0 , \\ \frac{\partial \rho_1}{\partial t} &= -\rho_0 \left(\frac{\partial v_r}{\partial r} + \frac{2}{r} v_r + \frac{1}{r} \frac{\partial v_\theta}{\partial \theta} + \frac{\cot \theta}{r} v_\theta \right) \\ &\quad + v_r \frac{\cos \theta}{H} \rho_0 - v_\theta \frac{\sin \theta}{H} \rho_0 , \text{ and} \\ \frac{\partial p_1}{\partial t} &= -\gamma P_0 \left(\frac{\partial v_r}{\partial r} + \frac{2}{r} v_r + \frac{1}{r} \frac{\partial v_\theta}{\partial \theta} + \frac{\cot \theta}{r} v_\theta \right) \\ &\quad + v_r \frac{\cos \theta}{H} P_0 - v_\theta \frac{\sin \theta}{H} P_0 \end{aligned} \quad (A-33)$$

where $\vec{V} = V_r \hat{e}_r + V_\theta \hat{e}_\theta$, $\rho = \rho_0 + \rho_1$, and $P_1 = P_0 + P_1$.

If we temporarily assume $V_\theta = 0$ and write $V_r = U/r$ an equation for U is found as

$$\frac{\partial^2 U}{\partial t^2} = c_0^2 \frac{\partial^2 U}{\partial r^2} - c_0^2 \frac{\cos \theta}{H} \frac{\partial U}{\partial r} \quad (A-34)$$

Therefore for a spherical outgoing wave with

$$U \sim e^{i(kr - \omega t)} \quad (A-35)$$

we find the dispersion relation

$$\left. \begin{aligned} \frac{\omega^2}{c_0^2} &= k^2 + i \frac{\cos \theta}{H} k \\ \text{or} \quad k &= -i \frac{\cos \theta}{2H} + \frac{1}{2} \left[\frac{4\omega^2}{c_0^2} - \frac{\cos^2 \theta}{H^2} \right]^{1/2} \\ \text{or} \quad k &= \frac{\omega}{c} \left[1 - \frac{c_0^2 \cos^2 \theta}{4H^2 \omega^2} \right]^{1/2} - i \frac{\cos \theta}{2H} \end{aligned} \right\} \quad (A-36)$$

The limit $H \rightarrow \infty$ gives the usual isotropic case. However if

$$\omega < \frac{c_0}{2H} \cos \theta \quad (A-37)$$

k is purely imaginary and such frequencies will not propagate. For this reason $\omega_c = \frac{c_0}{2H}$ is known as the acoustic cutoff frequency. The numerical value in the lower atmosphere is $\sim 2 \times 10^{-2} \text{ sec}^{-1}$.

The velocity of the particles will therefore be

$$V_r \propto \frac{1}{r} \exp i ((\text{Re } k) r - \omega t) \exp \left(\frac{\cos \theta}{2H} r \right) \quad (\text{A-38})$$

Thus for an upwardly traveling wave the particle velocity, and also the pressure, increases exponentially according to

$$V_r \cong c_0 \frac{\rho_1}{\rho_0} \cong \frac{P_1}{c_0 \rho_0} \propto \frac{1}{r} e^{\frac{r}{2H}} \quad (\text{A-39})$$

in the acoustic limit for $\omega \gg \omega_c$.

Returning to the question of V_θ , we find using our solutions,

$$\frac{|V_\theta|}{|V_r|} \approx \frac{\frac{\sin \theta}{H} \left(\frac{1}{Y} - \frac{1}{2} \right)}{\left[\left(\frac{\omega}{c} \right)^2 + \frac{\cos^2 \theta}{4H^2} \right]^{\frac{1}{2}}} \quad (\text{A-40})$$

Therefore if $\frac{\omega}{c} \gg \frac{1}{2H}$ it will be true that $|V_\theta| \ll |V_r|$ and the $V_\theta = 0$ assumption (strictly radial flow) is justified. The condition for validity is perhaps better written

$$\lambda \ll 4\pi H \quad (\text{A-41})$$

where $\lambda = 2\pi c/\omega$ is the wavelength. Note that the condition for upward propagation (2-37) could have been written $\frac{2\pi c_0}{\omega} < 4\pi H$ although since

$$\lambda = 2\pi/\text{Re } k = 2\pi c_0/\omega [1 - \omega_c^2/\omega^2]^{-\frac{1}{2}}, \quad (\text{A-42})$$

the quantity $2\pi c_0/\omega$ ceases to be the wavelength unless $\omega \gg \omega_c$.

The important conclusion is that so long as $\omega \gg \omega_c$, which is usually the case, the pressure of a pulse propagating up into a decreasing stratified medium will vary as $P_1/P_0 \propto \frac{1}{r} e^{r/2H}$ according to the acoustic equations. Of course no energy will be lost from the pulse and the pulse will not change shape so long as $\omega \gg \omega_c$.

Non-Linear Propagation

There exists no analytic solution to the general non-linear problem of propagation of a pulse into a medium of variable density. However, some related problems have been studied which contain some aspects of the problem of current interest⁴. Raizer⁵ produced a similarity solution for the case of a strong plane shock in an infinite medium with exponentially varying density. This solution, also found by Grover and Hardy⁶, allows the shock wave to reach infinity in a finite time with a shock velocity at position x

$$V_s(x) = c e^{\alpha x/H} \quad (A-43)$$

where α is a function of γ given in Figure 9. Grover and Hardy also studied the problem by a finite difference code and found that asymptotically the solution approached the similarity solution largely independently of the initial pulse configuration. The similarity character of this solution is such that the ratio of the variables ρ , P , and u behind the shock to that at the shock is constant for a fixed distance behind the shock. Consequently one cannot speak about the length of the pulse.

They considered by their finite difference code the same problem in spherical and cylindrical geometry and found the asymptotic behavior to involve the same exponential factor. This is shown by Figure 10.

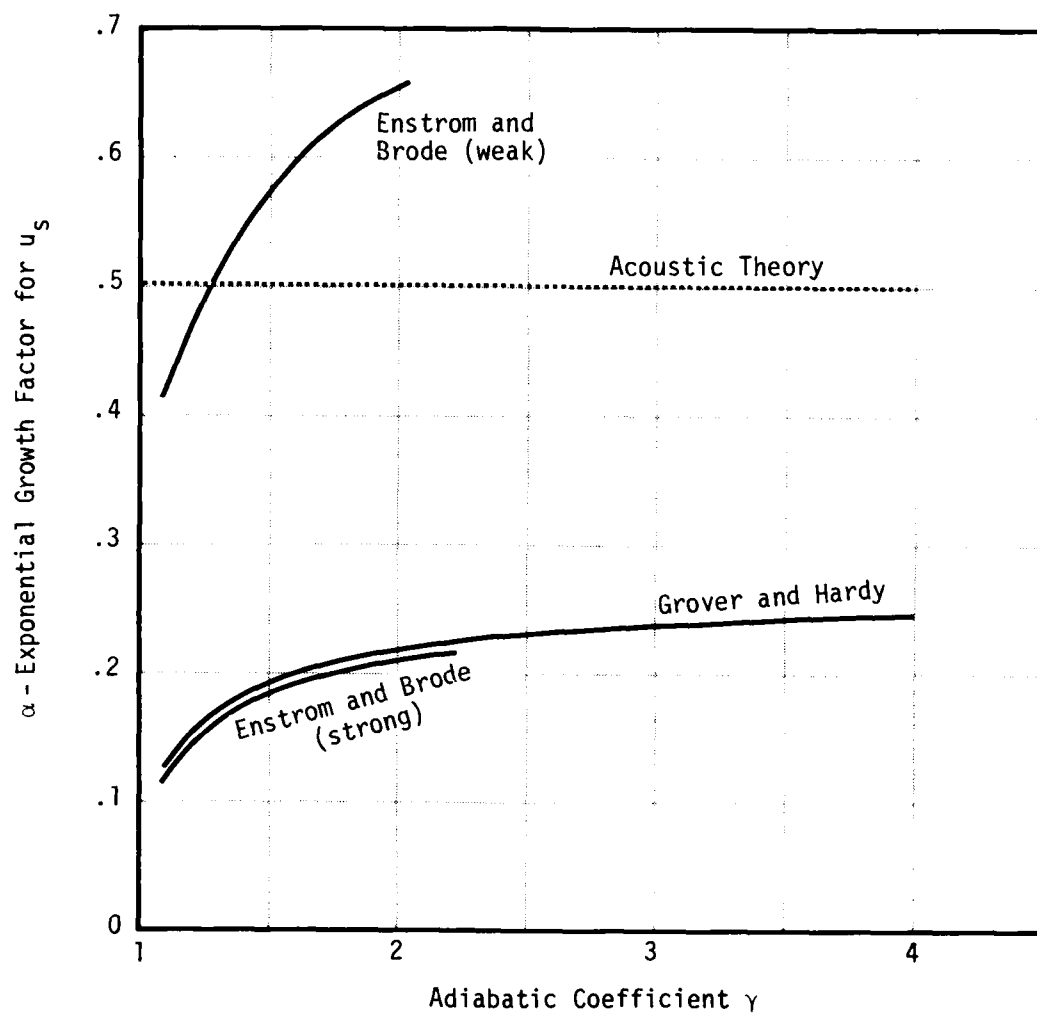


Figure A-9. Exponential Growth Factor α where $u_s \propto \exp(\alpha(\gamma)x/H)$.

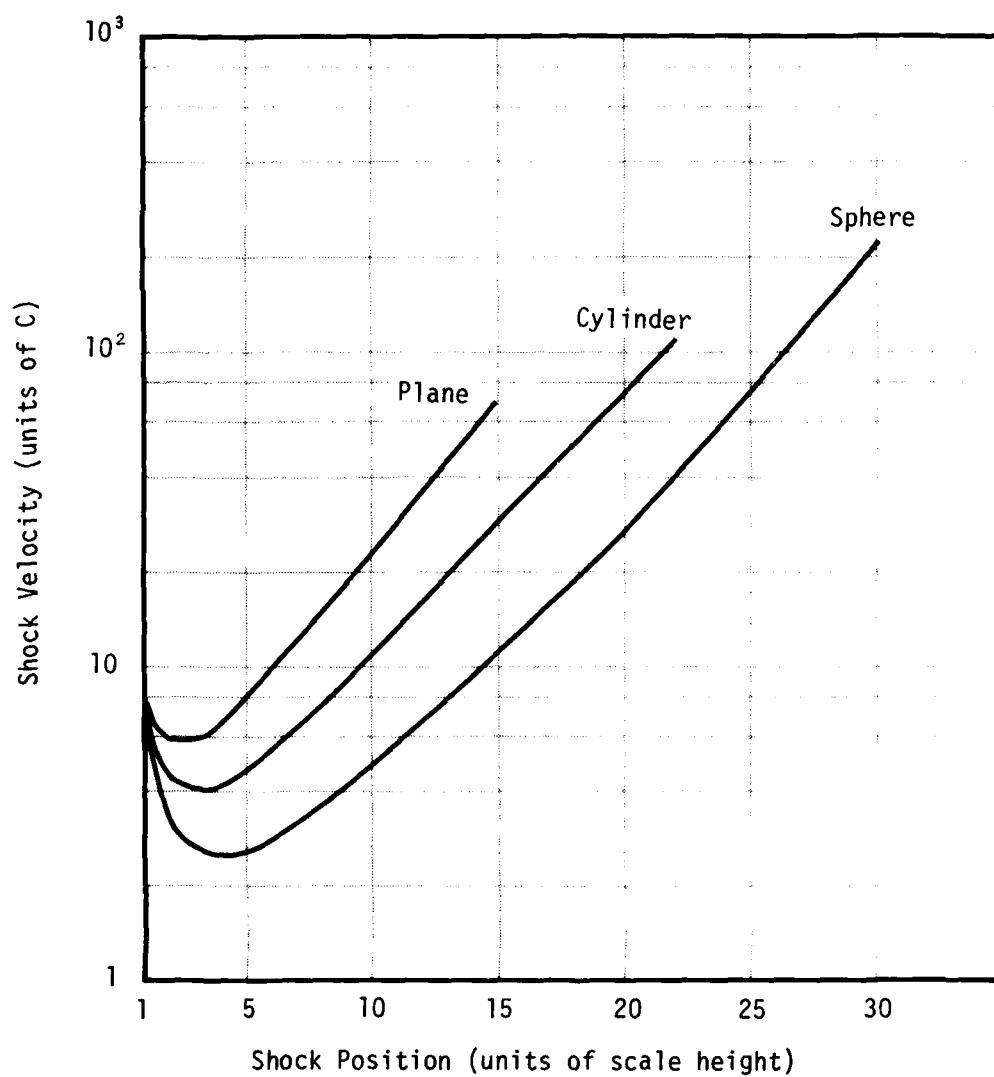


Figure A-10. Shock Velocity versus Position for $\gamma = 2$ (from Grover and Hardy).

In a similar vein Enstrom and Brode⁸ have considered finite difference solutions for both weak and strong shocks in planar geometry. For strong shocks the growth is very much like that of Grover and Hardy⁷, that is

$$V_s \propto e^{\alpha x/H}, \quad (A-44)$$

while for weak shocks the growth is much more rapid as indicated on Figure 9. Strong and weak here mean whether $P \cdot H$ is much less than or much greater than the energy per unit area of the shock.

From these considerations we expect that the upwardly traveling shock from a nuclear explosion will behave like

$$V_s \propto \frac{1}{r} e^{+\frac{3\alpha}{H} r} \quad (A-45)$$

once the shock wave gets sufficiently far away from the burst point. Since H is a function of height and increases rapidly above 100 km, one may expect the growth to decrease substantially in the real atmosphere in this region.

MODEL FOR PROPAGATION

In order to understand how the upwardly propagating shock varies with yield and burst altitude, it would be useful to have a simple model of the process short of the use of expensive two dimensional finite difference codes. Otterman⁸ has suggested a model for such propagation of nearly acoustic pulses and Reed⁹ has provided an additional condition which allows some loss of energy as in the semi-acoustic theory of Bethe¹.

The Otterman-Reed model provides for a triangular pressure pulse propagating with length $L(R)$ and relative overpressure $\beta(R)$. This pulse

is to be such that the flow is strictly radial so that the model is one dimensional and spherical. It is assumed that the tail of the pulse which is at ambient pressure, travels at the ambient sound speed while the head of the pulse advances at the shock speed, and that the shape of the pulse remains triangular. This means that

$$\frac{dL}{dt} = V_s(R) - c_0 \quad . \quad (A-46)$$

It is reasonable that the tail advances at the sound speed since the tail is at the ambient condition where c is exactly the speed with which disturbances are propagated. However, the assumption about constancy of shape requires some support. The energy in the pulse is taken as

$$E_s = \frac{4\pi}{3\gamma} R^2 \beta^2 L P_0(R) \quad (A-47)$$

which is obtained for an acoustic spherical pulse with a triangular pressure distribution of length L . This is readily found by taking E_s as twice the kinetic energy

$$E_s = 4\pi R^2 \rho_0 \int u^2 dR \quad (A-48)$$

where $\beta = u p_0 / c$. To complete the model Reed observed that

$$\frac{dE_s}{dR} = - \frac{(\gamma+1)}{3\gamma^2} P_0 \beta^2 R^2 = - \frac{(\gamma+1)}{4\gamma} \frac{\beta}{L} E_s \quad (A-49)$$

for the small β limit as noted earlier. Finally one notes that the Rankine-Hugoniot condition on the shock velocity in the weak shock limit is

$$V_s \cong c \left[1 + \beta \frac{(\gamma+1)}{4\gamma} \right] \quad . \quad (A-50)$$

Therefore the final set of equations is

$$\text{and } \left. \begin{aligned} \frac{dL}{dR} &= \frac{\gamma+1}{4\gamma} \beta \\ \frac{1}{E_s} \frac{dE_s}{dR} &= - \frac{\gamma+1}{4\gamma} \frac{\beta}{L} \end{aligned} \right\} \quad (\text{A-51})$$

where $E_s = \frac{4\pi}{3\gamma} R^2 \beta^2 L P_0(R)$. Taking $D^+(R)$, the duration of the positive pulse, to be given by $D^+(R) = L^+/c_0$, the solution to the above equations gives the result previously quoted in Equation (2-13).

This model is not suitable for our purposes because it is limited to very weak shocks. However, the basic ingredients are not explicitly dependent upon the weak shock assumption so one can attempt to modify the model for higher pressure. Kahalas and Murphy¹⁰ have added the second order corrections to the shock velocity and energy loss which allow a somewhat stronger shock to be described, but this is still inadequate for our purposes. We propose to avoid expanding in powers of β and simply express the shock speed and energy loss in their general form. That is we will take as our model equations

$$\frac{dL}{dR} = \frac{V_s - c}{V_s} \quad \text{and} \quad (\text{A-52})$$

$$\frac{dE_s}{dR} = - \frac{4\pi\gamma}{\gamma-1} R^2 \left[\left(\frac{\rho_s}{\rho_0} \right) \left(\frac{P_s}{P_0} \right)^{\frac{1}{\gamma}} - 1 \right] - \frac{dE_g}{dR}.$$

here ρ_s and V_s are found from the Hugoniot conditions as

$$\left. \begin{aligned} \rho_s / \rho_0 &= \frac{\gamma+1}{\gamma-1 + \frac{2c^2}{V_s^2}} \\ \text{and } P_s / P_0 &= 1 + \beta = 1 + \frac{2\gamma}{\gamma+1} \left(\frac{V_s^2}{c^2} - 1 \right). \end{aligned} \right\} \quad (\text{A-53})$$

The quantity dE_g/dR will represent energy lost to the gravitational potential.

The energy in the pulse will be taken to be twice the kinetic energy. It will be assumed that the pulse is triangular in the particle velocity (rather than pressure) as viewed in Lagrangian coordinates. Thus the energy will be

$$E_s = 4\pi \int_{R-L}^R \rho_0(r) u^2 r^2 dr \quad (A-54)$$

where $u = u_s \left(\frac{r+L-R}{L} \right)$ and $\rho_0(r) = \rho^* \exp(-r/H)$. ρ^* is the ambient density at the burst altitude. Generally $H(r)$ is a function of position but it is only slowly varying. Note that H is the average scale height up to r , not the local scale height. Assuming H can be removed from the integral we define a function f by

$$E_s = \frac{4\pi\gamma}{3} \left(\frac{u_s}{c} \right)^2 LR^2 P_0(R) \exp(fL/H). \quad (A-55)$$

Thus f is the fraction of L back from the pulse front at R such that

$$\int_{R-L}^R r^2 e^{-r/H} \left(\frac{r+L-R}{L} \right)^2 dr = R^2 e^{-(R-fL)/H} \int_{R-L}^R \left(\frac{r+L-R}{L} \right)^2 dr. \quad (A-56)$$

This requires

$$f = 1 - \frac{1}{x} \ln \left(\frac{y^2 x^3}{3(h-g)} \right)$$

where

$$\left. \begin{aligned} x &= L/H, \quad y = R/H, \\ h &= 24 + 12(y-x) + 2(y-x)^2, \text{ and} \\ g &= e^{-x} \left\{ x^4 + 4x^3 + 12x^2 + 24x + 24 + 2(y-x)(x^3 + 3x^2 + 6x + 6) \right. \\ &\quad \left. + (y-x)^2(x^2 + 2x + 2) \right\} \end{aligned} \right\} \quad (A-57)$$

The particle velocity at the shock u_s is related to β by the Hugoniot conditions giving

$$\frac{u_s}{c} = \frac{\beta}{\gamma\sqrt{1 + \beta(\gamma+1)/2\gamma}} \quad (A-58)$$

Note that for $\beta \rightarrow 0$, $u_s \propto \beta$ and for $\beta \rightarrow \infty$, $u_s \propto \sqrt{\beta}$. It may appear that $u_s \propto \beta$ is inconsistent with the assumption of the equality of the internal and kinetic energies. In fact this demonstrates the existence of the negative phase for weak pulses which gives a net contribution to the internal energy which is proportional to β^2 .

The loss of energy to gravity will be found by noting that following the passage of the shock the atmosphere will return to ambient pressure P_0 but to a temperature $T > T_0$. For an ideal gas this will be

$$T = T_0 \left(\frac{\rho_0}{\rho_s} \right) \left(\frac{P_s}{P_0} \right)^{\frac{1}{\gamma}} \quad (A-59)$$

with a density

$$\rho_f = \rho_0 \frac{T_0}{T} \quad . \quad (A-60)$$

Taking $R(r,t)$ as the Eulerian coordinate the continuity condition is

$$\rho_f R^2 dR = \rho_0(r) r^2 dr \quad (A-61)$$

so that

$$R^3(r) - r_0^3 = 3 \int_{r_0}^r \left(\frac{T_0}{T} \right) r^2 dr \quad . \quad (A-62)$$

The amount by which the atmosphere originally at r will be raised is thus

$$\Delta r = R(r) - r$$

and the energy lost from the pulse will be

$$\frac{dE_g}{dr} = 4\pi r^2 \rho_0(r) (R(r) - r) g \quad . \quad (A-63)$$

From Equation (2-55) following differentiation with respect to r we obtain

$$\begin{aligned} \frac{1}{E_s} \left[\frac{dE_s}{dr} \right] &= \frac{1}{L} \frac{dL}{dr} + \frac{2}{r} - \frac{1}{H} + \frac{r}{H} \frac{dH}{dr} + \frac{f}{H} \frac{dL}{dr} + \frac{L}{H} \left(\frac{df}{dr} \right) \\ &\quad - \frac{L}{H^2} \frac{dH}{dr} + \frac{2}{(u_s/c)} \left(\frac{d(u_s/c)}{d\beta} \right) \frac{d\beta}{dr} \quad . \quad (A-64) \end{aligned}$$

AD-A119 947

MISSION RESEARCH CORP SANTA BARBARA CA

F/G 4/1

A MODEL FOR GRAVITY WAVES PRODUCED BY LOW ALTITUDE EXPLOSIONS F--ETC(11)

SEP 81 G D MCCARTOR, W R WORTHMAN, W R FROLLI

DNA001-R1-C-0022

UNCLASSIFIED

MRC-N-659

DNA-5885T

NL

20 2

00047

END

DATE

FILED

11 82

DTIC

Now $\frac{dH}{dr}$ is known from the atmosphere and $\frac{d(u_s/c)}{d\beta}$ is known from Equation (2-58). The function f is readily differentiated to give

$$\frac{df}{dr} = \left(\frac{\partial f}{\partial x} \right) \left(\frac{1}{H} \frac{dL}{dr} - \frac{1}{H^2} L \frac{dH}{dr} \right) + \left(\frac{\partial f}{\partial y} \right) \left(\frac{1}{H} - \frac{R}{H^2} \frac{dH}{dr} \right) \quad (A-65)$$

Combining these results we find

$$\begin{aligned} \frac{1}{E_s} & \left(- \frac{4\pi\gamma}{\gamma-1} r^2 \left(\left(\frac{\rho_0}{\rho_s} \right) \left(\frac{P_s}{P_0} \right)^{\frac{1}{\gamma}} - 1 \right) - \frac{dE_g}{dr} \right) \\ & = \frac{dL}{dr} \left(\frac{1}{L} + \frac{f}{H} + \frac{L}{H^2} \frac{\partial f}{\partial x} \right) + \frac{d\beta}{dr} \left(\frac{2}{(u_s/c)} \frac{d(u_s/c)}{d\beta} \right) \\ & + \frac{2}{r} - \frac{1}{H} + \frac{r}{H} \frac{dH}{dr} + \frac{L}{H} \left(- \frac{L}{H^2} \frac{dH}{dr} \frac{f}{x} + \frac{\partial f}{\partial y} \left(\frac{1}{H} - \frac{r}{H^2} \frac{dH}{dr} \right) \right) \\ & - \frac{fL}{H^2} \frac{dH}{dr} \quad (A-66) \end{aligned}$$

All parameters are either known or functions of β and L . Therefore if we use this in conjunction with

$$\frac{dL}{dr} = \frac{(V_s/c)-1}{(V_s/c)} \quad (A-67)$$

we have a pair of integrodifferential equations for $\beta(r)$ and $L(r)$. Note that dE_g/dr depends on the history of β .

SOLUTION OF THE MODEL EQUATIONS

These equations are readily integrated numerically using a Runge-Kutta procedure for initial values $\beta_0(r_0)$ and $L(r_0)$ provided dE_g/dr is suitably handled. The results are relatively insensitive to dE_g/dr so

it is treated by taking Δr to be constant in each interval of a scale height which is taken from the integration through the previous scale height. That is we use

$$\Delta r = \left[r_0^3 + 3 \sum_{i=1}^{n-1} \left(\frac{\rho_0}{\rho} \right)_i (r_0 + i\Delta x)^2 \Delta x \right]^{1/3} - r_0 \quad (\text{A-68})$$

for $r_0 + (n-1)\Delta x < r < r_0 + n\Delta x$ where Δx has been chosen somewhat arbitrarily as H which seems to be a suitable interval between printouts of the results.

To test the validity of the model we can compare with finite difference calculations in one dimension. The current model is easily modified to planar geometry so we can compare for both spherical and planar geometry.

For an exponential atmosphere in planar geometry we have the results of Enstrom and Brode⁷ as well as a local Lagrangian hydro-code (HYDRO) with which to compare. In Figure 11 two cases are shown using these two methods. In Figure 12 similar results are shown for spherical geometry.

For propagation into a real atmosphere we have used the CIRA¹¹ Model 5 (hour 8) case giving mid-solar cycle conditions. Since the real atmosphere is far from isothermal in the region above 100 km, one expects substantial differences. In Figure 13 planar geometry is shown for the current model and hydro-codes while Figure 14 gives the results for spherical geometry. All these results indicate that the model provides a reasonable description of the propagation so long as the relative overpressure is much less than 100.

The model is readily changed for propagation at some angle θ relative to vertical by making the substitution $H \rightarrow H \cos\theta$ in all expressions. Having done this we can compare the model with the results of Greene and Whitaker¹² who consider the initial condition of a 4 MT isothermal sphere at sea level using both a one-dimensional and two-dimensional hydro-code for propagation at 45°. The model was given initial conditions for

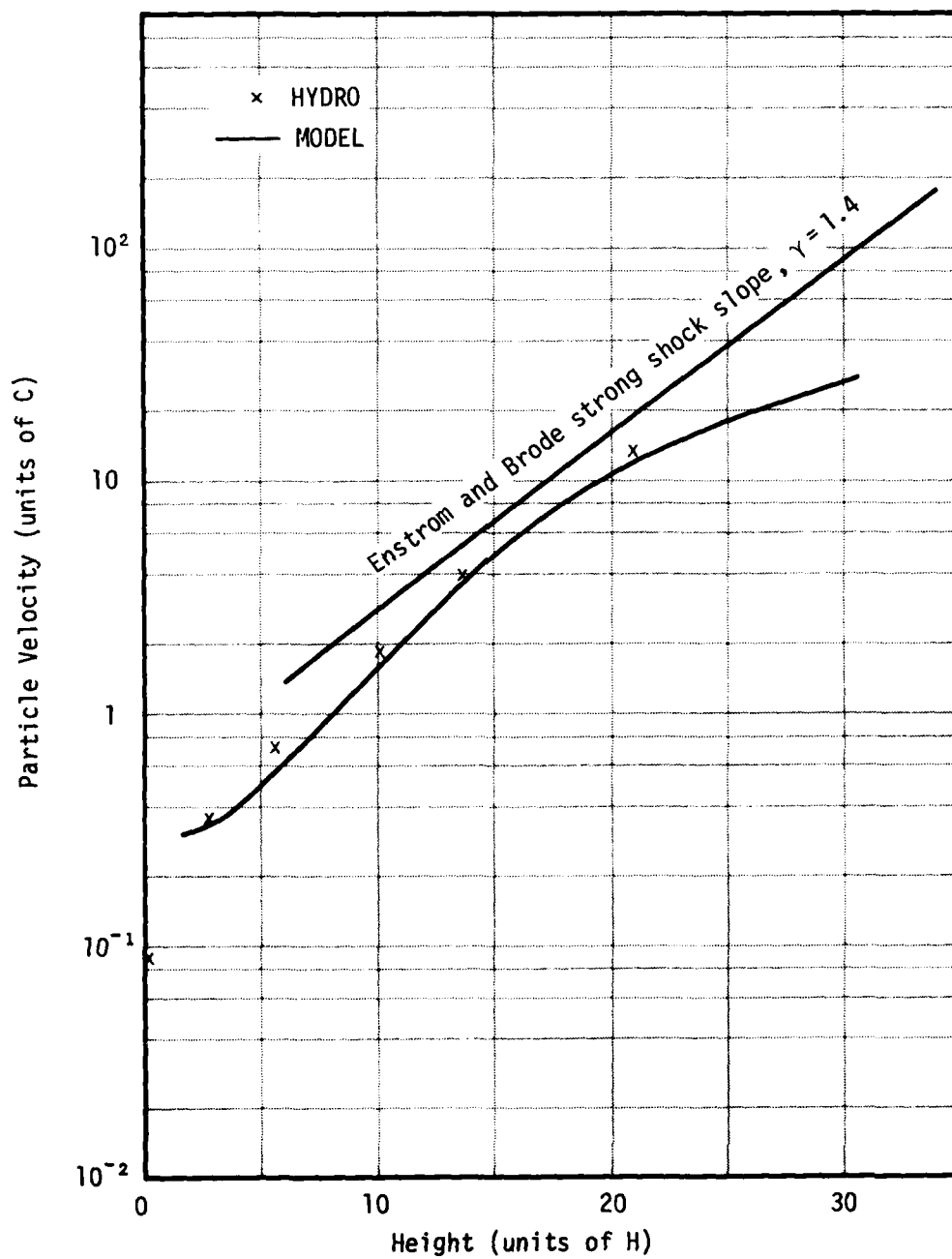


Figure A-11. Comparison of MODEL, HYDRO code, and Strong Shock Slope for a Plane Shock in an Exponential Atmosphere.

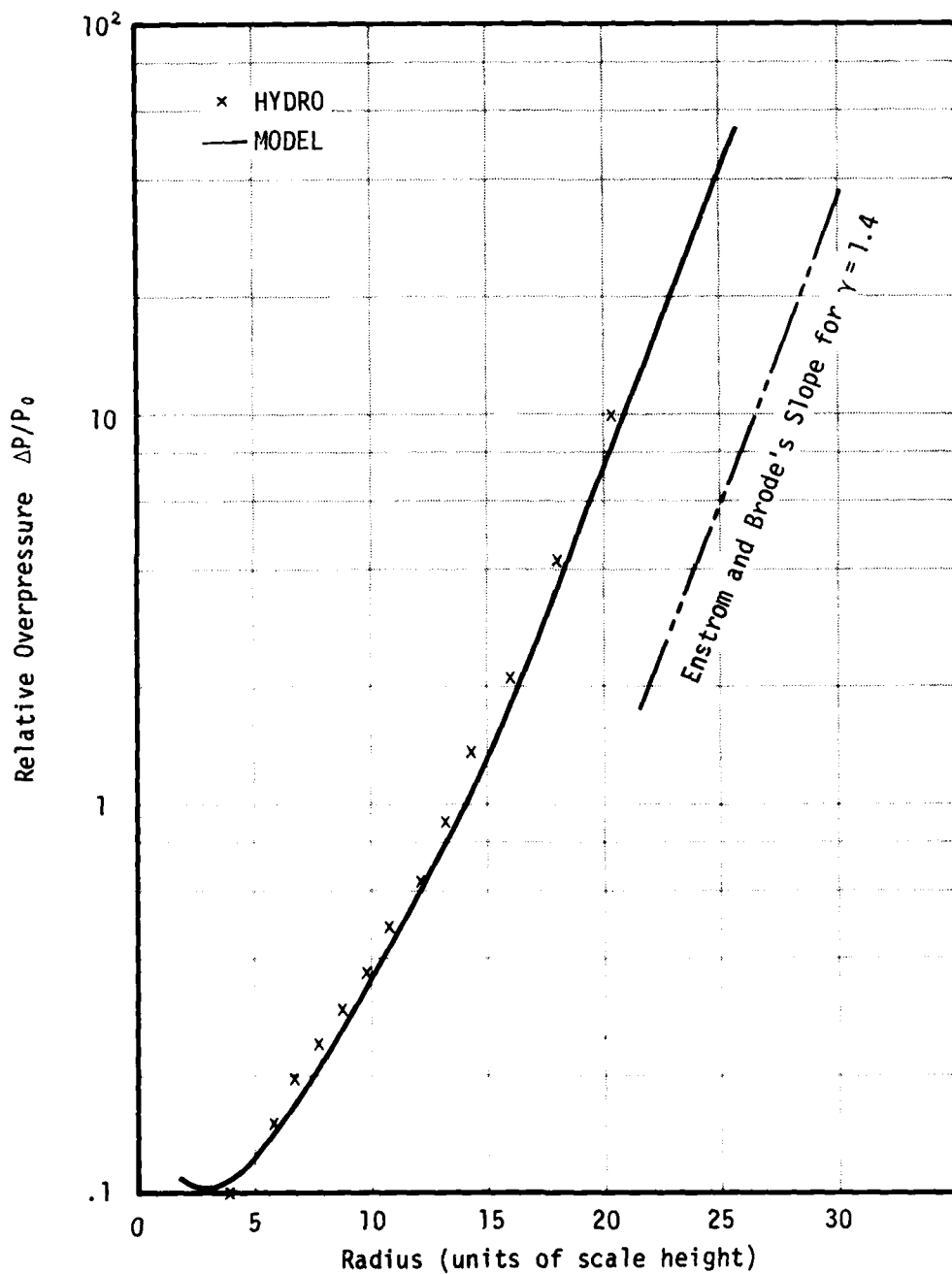


Figure A-12. Comparison of MODEL, HYDRO Code and Strong Shock Slope for a Spherical Exponential Atmosphere.

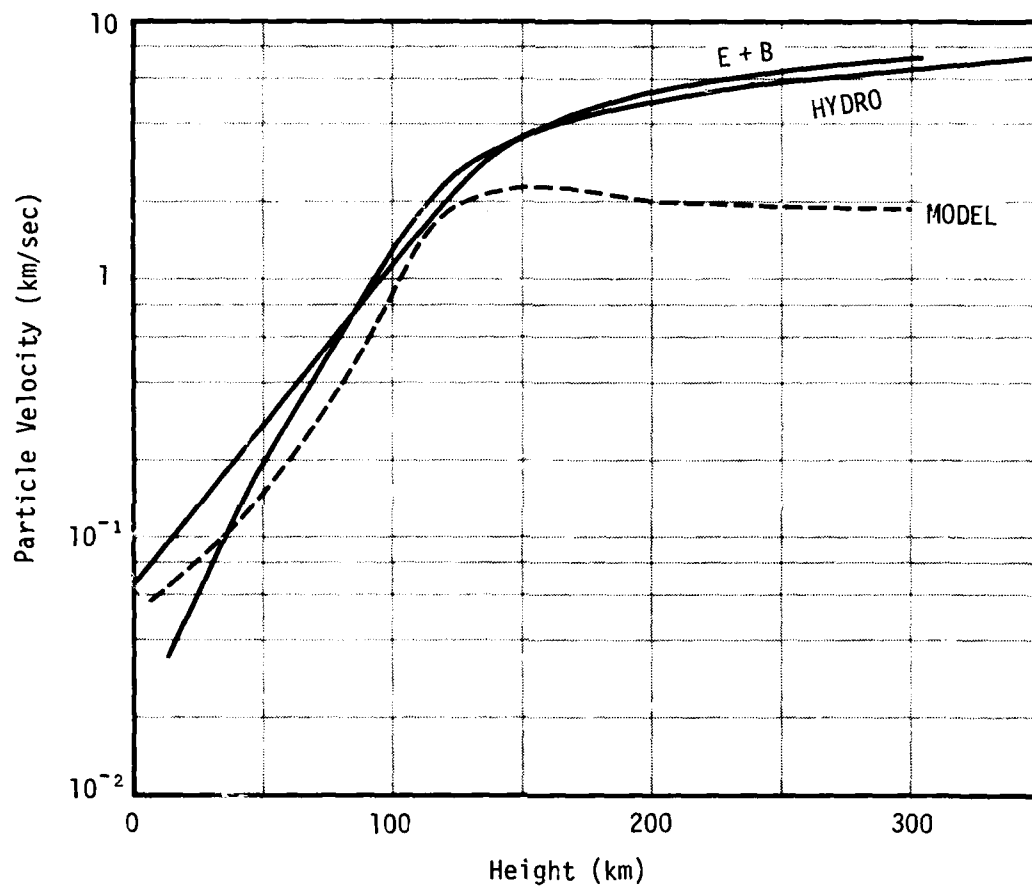


Figure A-13. Comparison of MODEL, HYDRO Code and Enstrom and Brode's Result for a Plane Shock in a Real Atmosphere.

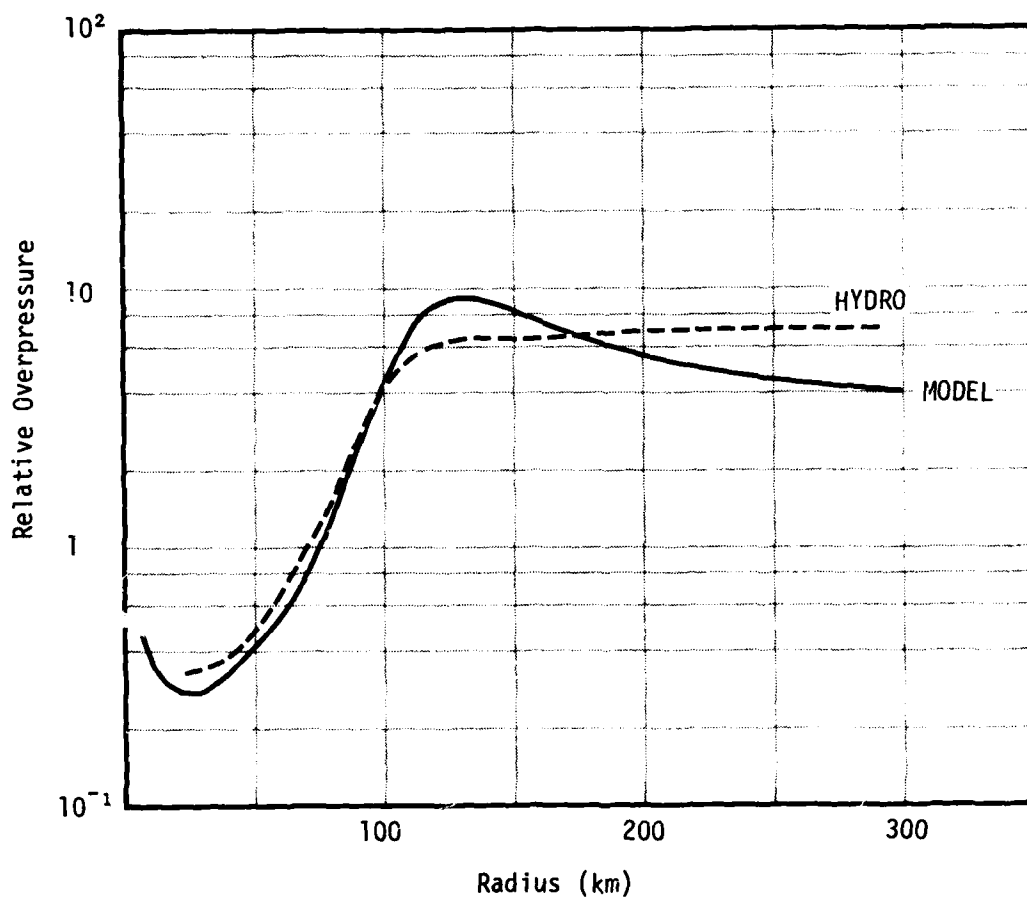


Figure A-14. Comparison of MODEL and HYDRO Code for a Spherical Shock in a Real Atmosphere.

L_0 and β_0 using Brode's calculation as a guide as discussed in the following two paragraphs. The results are shown in Figure 15 along with a HYDRO run with the same initial conditions given to the model. Again the model somewhat overestimates the pressures.

The model makes use of the assumption that the pulse is linear in the particle speed. To test this assumption a HYDRO calculation was made starting with a linear pulse propagating upwardly. The resulting pulse is shown in Figure 16 as a function of Lagrangian and Eulerian coordinates. The near linearity of the particle speed as a function of the Lagrangian position validates the assumption of linearity for the model.

We are now prepared to use this model for a variety of yields and altitudes to determine the character of the shocks in the upper atmosphere which may lead to communications effects. In order to initialize the pulse we have used the results of Brode for the relative overpressure $\beta(r)$ and positive pulse duration $D_p^+(r)$ for a spherical shock wave for some radii at which the pulse develops a linear character. For radii scaled to a dimensionless variable λ by

$$r = \lambda \left(\frac{E_{TOT}}{P} \right)^{1/3} \equiv \lambda R_{sc} , \quad (A-69)$$

we take the overpressure as

$$\beta = \frac{.137}{\lambda^3} + \frac{.119}{\lambda^2} + \frac{.269}{\lambda} - .019 \quad (A-70)$$

for $.1 \lesssim \beta \lesssim 10$ which corresponds to $.2 \lesssim \lambda \lesssim .25$.

Using Brode's $D_p^+(\lambda)$ and taking the shock speed as the sound speed for this weak shock region the pulse length was fit by

$$L(\lambda) = .116\lambda + .15 - .0012 \exp(1.84\lambda) . \quad (A-71)$$

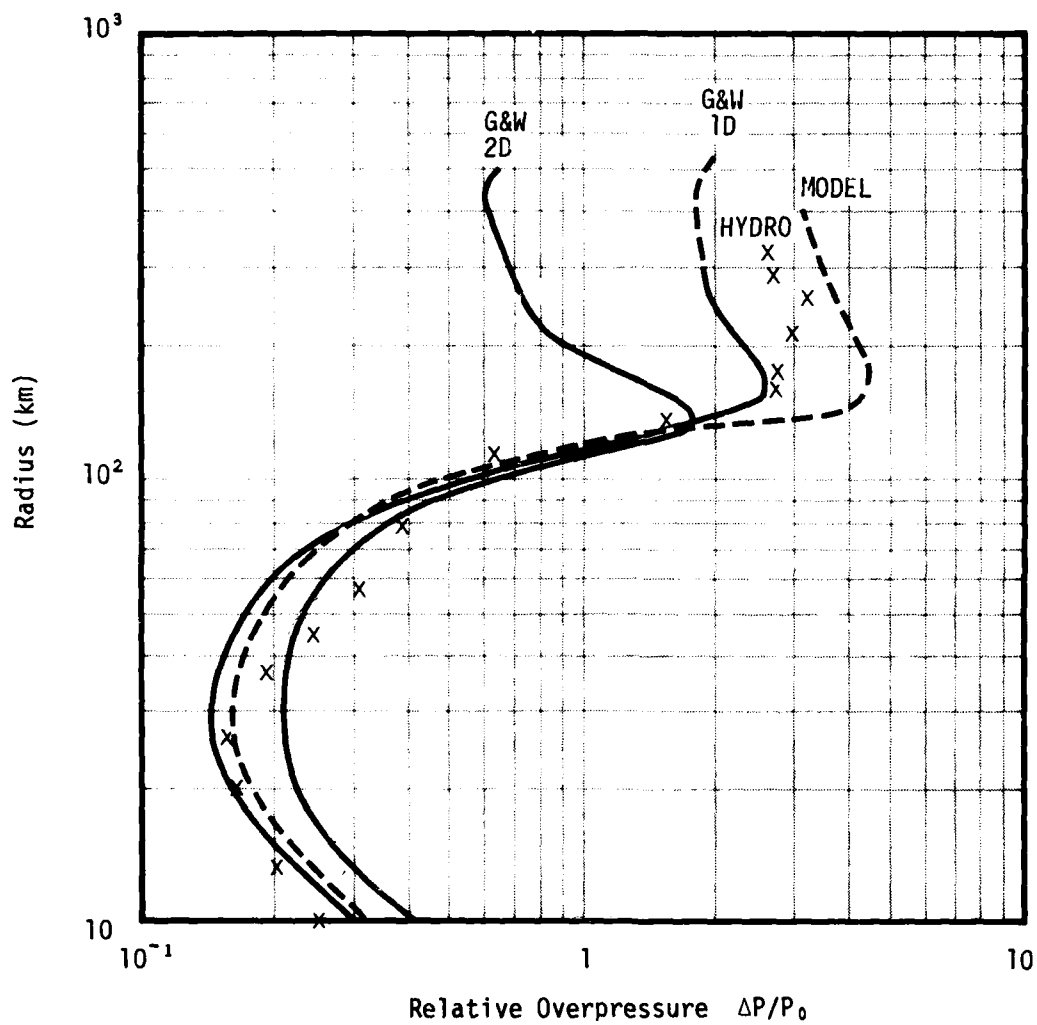


Figure A-15. Comparison of MODEL, HYDRO Code, and Greene and Whitaker's Results for 45° Propagation Resulting from 4 MT at Sea Level.

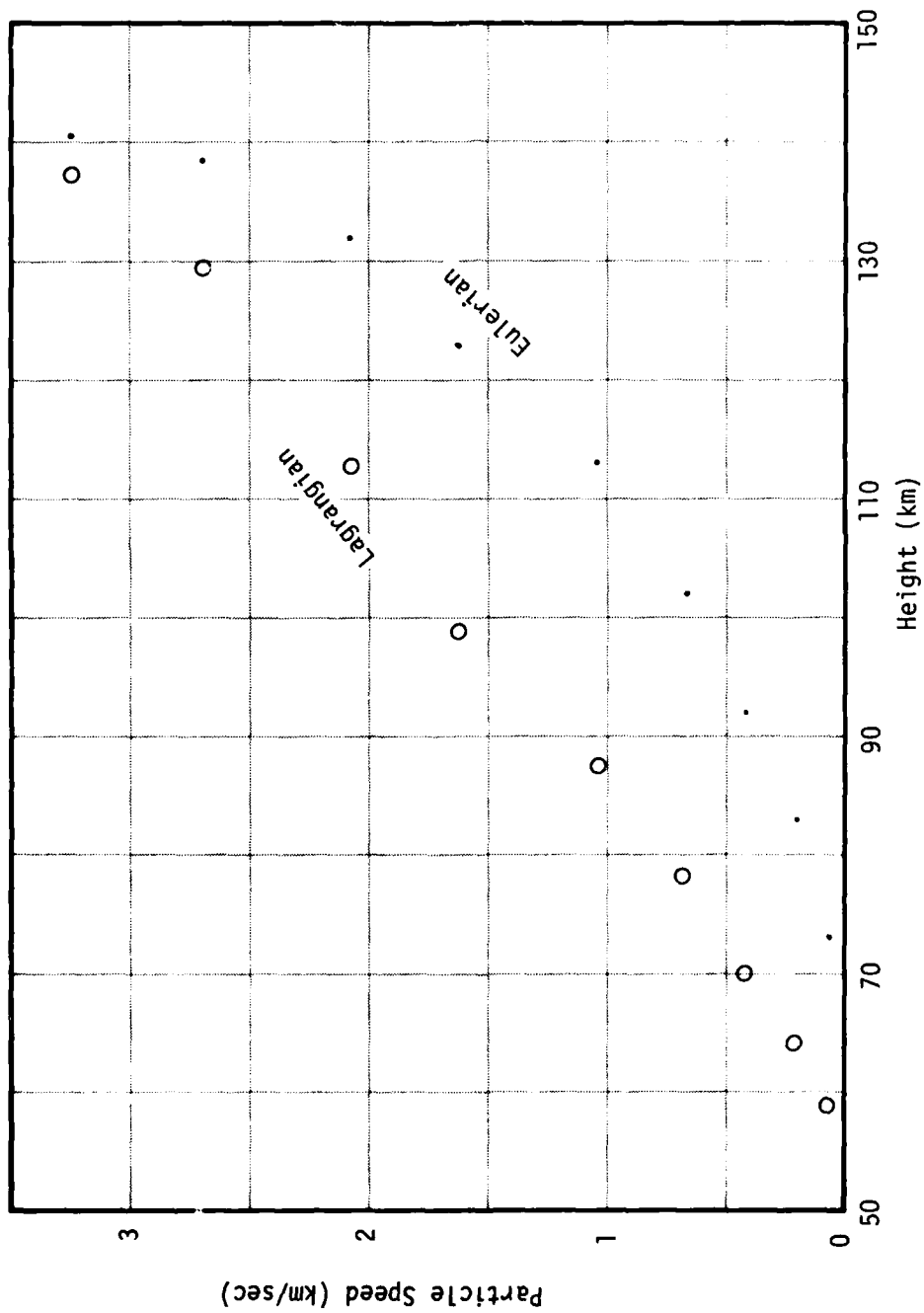


Figure A-16. Particle Speed in a Pulse as a Function of Lagrangian and Eulerian Coordinates as Obtained by a HYDRO Calculation for an Initially Linear Pulse.

In order to initialize β and L for all angles to guarantee equal energy in all directions the initial conditions were chosen as

$$\begin{aligned} R_0 &= x\lambda R_{sc} \\ L_0 &= L(\lambda) \times R_{sc} \end{aligned} \quad (A-72)$$

and

$$\beta = \beta(\lambda).$$

$$\text{Here } \lambda = \text{MIN} \left[2, \frac{H}{1.2 R_{sc}} \right] \text{ and } x = 3 \left(\frac{H}{\lambda R_{sc}} \right) \ln(x) (\cos\theta)^{-1}.$$

This procedure sets upper limits on the yield, for a given altitude, which can be handled. This is

$$Y_{\max} \cong P_0 \left(\frac{4H}{1.2} \right)^3 \quad (A-73)$$

which, for example, means $Y_{\max}(\text{sea level}) = 300 \text{ MT}$ and $Y_{\max}(100 \text{ km}) = .09 \text{ KT}$. For cases outside this range the upward traveling shock would remain very strong at all altitudes if the scale height were constant. In Table 1 are shown results for a variety of yields and altitudes for propagation upward and for $\theta = 45^\circ$.

Sears and Kamm¹³ have attempted to account for some F-region disturbances following several high altitude tests, Teak being the most prominent, as being due to passage of the shock wave. The arrival times for the disturbances were taken from ionosonde data and shock pressures were calculated based on these times and empirical scaling laws. They concluded that the shock waves were Mach 2 to 3 in the F-region over Maui (1500 km away from the Johnston Island test site).

The model described in this report (MODEL) would not generally be applicable to the cases considered by Sears and Kamm. However, due to the nearly horizontal direction of propagation, we were able to use MODEL with an initial shock strength consistent with the required pulse shape. It was found that the F-region arrival times at Maui predicted by MODEL were 2 to

Table A-1. Model Results for Pulse Relative Overpressure β and Pulse Length L for Different Yields and Altitudes.

Altitude (km)			100		150		200		250		300		350	
Yield (kT)	Burst Altitude (km)	Angle Degree	β	L (km)	β	L (km)	β	L (km)	β	L (km)	β	L (km)	β	L (km)
30000	0	0	15.	37	23.	76	13.	115	9.5	150	8.2	180	7.6	210
		45	7.5	40	13.	90	8.0	140	6.2	180	5.4	230	5.2	260
10000	0	0	7.8	27	13.	67	8.1	100	6.3	130	5.5	160	5.3	190
		45	4.0	28	7.0	70	5.0	115	4.1	150	3.8	190	3.7	220
4000	0	0	4.5	21	8.0	55	5.5	87	4.5	110	4.1	140	4.0	165
		45	2.3	21	4.3	58	3.4	95	3.0	130	2.8	160	2.8	195
1000	0	0	2.1	15	3.8	41	3.1	64	2.8	88	2.6	110	2.6	130
		45	1.2	14	2.0	36	1.8	69	1.7	95	1.7	120	1.8	145
100	0	0	0.7	7	1.0	20	1.0	33	1.0	45	1.0	60	1.0	70
		45	0.4	6	0.6	18	0.6	33	0.6	46	0.6	60	0.6	70
2000	33	0	5.0	24	7.4	56	5.0	87	4.0	115	3.6	140	3.6	165
		45	2.9	28	4.8	67	3.5	105	3.0	140	2.8	170	2.8	200
500	0	0	3.8	22	6.2	52	4.3	80	3.5	105	3.3	130	3.2	155
		45	2.0	23	3.3	57	2.6	89	2.3	120	2.2	150	2.2	180
100	0	0	1.6	14	2.6	35	2.1	57	1.9	77	1.9	96	1.9	115
		45	0.9	13	1.4	36	1.2	58	1.2	80	1.2	100	1.2	120
10	0	0	0.6	7	0.8	18	0.7	30	0.7	40	0.7	50	0.8	60
		45	0.3	6	0.5	18	0.4	28	0.4	38	0.4	50	0.5	60
20	67	0	1.7	14	1.8	34	1.4	51	1.3	67	1.3	82	1.3	98
		45	1.1	16	1.2	38	1.0	57	0.9	76	0.9	95	1.0	115
5	0	0	1.5	13	1.5	30	1.2	46	1.1	61	1.1	75	1.2	90
		45	0.8	13	0.9	30	0.7	47	0.7	62	0.7	77	0.7	92
1	0	0	0.6	7	0.7	18	0.6	28	0.6	37	0.6	46	0.6	55
		45	0.4	8	0.4	18	0.4	28	0.4	37	0.4	45	0.4	54
.05	100	0	-	-	0.4	13	0.3	19	0.3	24	0.3	29	0.3	34
		45	-	-	0.2	14	0.2	19	0.2	23	0.2	27	0.2	32

3 times those observed and the shock pressures were 5 to 10 times less than those given by Sears and Kamm. The disparity is so great as to lead us to suspect that straight line shock propagation cannot account for the disturbances.

APPENDIX B

(From an unpublished report)

THE CALCULATION OF LINEAR DISTURBANCES IN AN ISOTHERMAL ATMOSPHERE

The simplest model of the atmosphere which exhibits a substantial number of the features of interest to the considerations of this report is that of an isothermic atmosphere having a constant ratio of specific heats, γ , in which we assume all disturbances are sufficiently weak that the linearized hydrodynamic equations apply. If we restrict ourselves to point sources (which depend on time), we can obtain an exact solution with no great effort or expense. We have written a small computer code which performs this task. The reasons for writing such a code are two-fold: first, the model in hand approximates the earth's atmosphere and the pressure source due to an underground explosion sufficiently well to allow useful comparisons with test data or order-of-magnitude estimates of some parameters in hypothetical situations; second, we can use the exact results from the code to test possible approximation procedures which appear potentially useful for calculations with more complicated atmospheres or sources.

It is shown in Reference B-1 that the response of an isothermal atmosphere to a point source at the origin can be calculated using the Green's function

$$G(z, r, \omega) = \frac{1}{4\pi R} \left(\frac{\omega^2 - \omega_g^2}{\omega^2 - \omega_c^2} \right)^{1/2} \exp \left[i t_0 (\omega^2 - \omega_c^2)^{1/2} \left(\frac{\omega^2 - \omega_A^2}{\omega^2 - \omega_g^2} \right)^{1/2} \right], \quad (B-1)$$

where z is the altitude, r is the horizontal distance, and ω is the Fourier transform variable conjugate to the time. The constants in Equation B-1 are defined as follows

$$\begin{aligned}\omega_g &= (\gamma-1)^{1/2} \frac{g}{c}, \\ \omega_A &= \frac{\gamma g}{2c}, \\ R &= (r^2 + z^2)^{1/2}, \\ \omega_c &= \frac{z\omega}{R} \quad \text{and} \\ t_0 &= \frac{R}{c},\end{aligned}\tag{B-2}$$

where g is the constant acceleration of gravity and c the speed of sound. We can use this Green's function to calculate the relative pressure fluctuation $\delta p/p_0$, p_0 being the unperturbed pressure, by computing

$$\frac{\delta p}{p_0}(z, r, t) = \frac{1}{2\pi} e^{\frac{z}{2H}} \int_{-\infty}^{\infty} G(z, r, \omega) \tilde{M}(\omega) e^{-i\omega t} d\omega, \tag{B-3}$$

where M is the Fourier transform of the pressure source:

$$\tilde{M}(\omega) = \int_{-\infty}^{\infty} M(t) e^{i\omega t} dt, \tag{B-4}$$

and $M(t)$ is the relative pressure source. As it stands, Equation B-3 is only a formal expression, for we have not chosen the branch on which G is to be evaluated or indicated the integration path (it is not, in general, the real axis). From (B-1), we see that G has branch points at $\pm\omega_g$, $\pm\omega_A$, and $\pm\omega_c$. These points are real and their relative magnitude is as shown in

Figure B-1. We choose the function to have the set of branch cuts shown in Figure B-1, cuts joining ω_A to ω_g , ω_g to ω_c , ω_c to $-\omega_c$, $-\omega_c$ to $-\omega_g$, and $-\omega_g$ to $-\omega_A$, all the cuts running along the real axis. For real values of ω greater than ω_A , we choose all the square-roots in Equation B-1 to be evaluated on the principal branch of the square-root function. With the chosen set of branch cuts, the function G is now determined everywhere by analytic continuation. The path of integration for Equation B-3 is that shown in Figure B-1(a) running slightly above the real axis. That this path must be chosen is dictated by causality.

For most choices of $M(t)$, the integral of Equation B-3 must be done numerically. The best way to execute such a calculation will depend upon the singularities of $\tilde{M}(\omega)$ and the behavior of this function for large values of ω . Rather than attempt a general discussion, we consider the class of functions:

$$M(t) = \begin{cases} 0 & , \quad t < -\frac{T_0}{2} \\ -A \frac{2t}{T_0} & , \quad -\frac{T_0}{2} < t < \frac{T_0}{2} \\ 0 & , \quad t > \frac{T_0}{2} \end{cases} \quad (B-5)$$

This set of functions, sometimes called N-waves, provides a reasonable representation of the pressure source resulting from an underground explosion. Using Equation B-4, we calculate

$$\tilde{M}(\omega) = \frac{2Ai}{\omega} \left[e^{\frac{i\omega T_0}{2}} \left(\frac{1}{2} + \frac{1}{iT_0\omega} \right) + e^{-\frac{i\omega T_0}{2}} \left(\frac{1}{2} - \frac{1}{iT_0\omega} \right) \right] \quad (B-6)$$

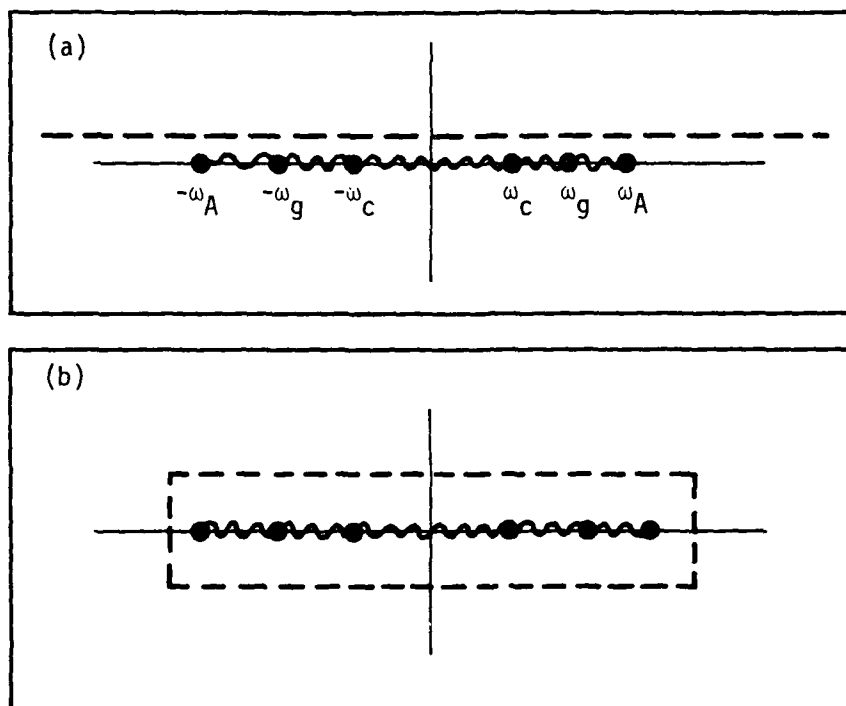


Figure B-1. (a) The location of the branch cuts and integration contour defining Equation B-3; (b) The integration contour used to compute I_1 and I_2 .

We use Equation B-6 to rewrite Equation B-3 as

$$\frac{\delta p}{p_0} = I_1 + I_2, \quad (B-7)$$

where

$$I_1 = \frac{1}{2\pi} e^{\frac{z}{2H}} \int_{-\infty}^{\infty} G \frac{2Ai}{\omega} e^{i\omega \frac{T_0}{2}} \left(\frac{1}{2} + \frac{1}{iT_0 \omega} \right) e^{-i\omega t} d\omega, \quad (B-8)$$

and

$$I_2 = \frac{1}{2\pi} e^{\frac{z}{2H}} \int_{-\infty}^{\infty} G \frac{2Ai}{\omega} e^{-i\omega \frac{T_0}{2}} \left(\frac{1}{2} - \frac{1}{iT_0 \omega} \right) e^{-i\omega t} d\omega. \quad (B-9)$$

Looking at Equation B-1, we see that, if ω has a large imaginary part, the behavior of the Green's function is dominated by $e^{i\omega t_0}$. The behavior of the integrand of Equation B-8 is thus dominated by $\exp i\omega(t_0 + T_0/2 - t)$, while that of Equation B-9 is dominated by $\exp i\omega(t_0 - T_0/2 - t)$. For times less than $t_0 - T_0/2$, we can close the contours for both I_1 and I_2 with a large semi-circle in the upper half-plane. Since neither G nor M have singularities in the upper half-plane, we thus get zero for $\delta p/p_0$, a result much to be expected since $t_0 - T_0/2$ is the arrival time of a pulse traveling at velocity c . If t lies between $t_0 - T_0/2$ and $t_0 + T_0/2$, the contour for I_1 can still be closed in the upper half-plane and the integral again gives zero. For values of the time in this range, if we wish to close the contour for I_2 we must do so in the lower half-plane and thus encircle the singularities of G . I_2 will, therefore be nonzero for $t_0 - T_0/2 < t$. In the same way, for $t_0 + T_0/2 < t$, I_1 will be nonzero and both I_1 and I_2 will contribute.

As discussed in the previous paragraph, whenever I_1 or I_2 is nonzero, we can close the contour in the lower half-plane. As there are no singularities in the lower half-plane or on the real axis for $\omega > \omega_A$, we can contract the contour to be the one shown in Figure B-1(b). It may appear that we can contract the contour further to integrate the discontinuity across the branch cuts along the real axis. This procedure would, however, lead to a problem equivalent to integrating $\exp(1/x)$ through the origin of x . We must, in fact, choose the contour with some care. If we come too close to the real axis, the singularities there cause problems, while if we go too far above the real axis, the exponential increase in the integrand causes difficulties. Using a simple first order integration technique and choosing the contour somewhat carefully, we can achieve three figure accuracy by using a few thousand points.

If $\omega_A = \omega_g$ (corresponding to a value $\gamma = 2$), the worst singularities in the Green's function cancel, and we can indeed contract the contour all the way to the real axis since the discontinuity of the integrand in that case contains only integrable square-root type singularities. We can thus save the trouble of choosing a contour, and the approximation $\omega_A = \omega_g$ is one whose accuracy we wish to investigate. Another simplifying approximation, called the low frequency limit, consists of assuming that the only important contributions to the integrals I_1 and I_2 come from the branch cut from ω_c to $-\omega_c$. In this approximation an answer can be given in closed form. In Reference B-1, several examples are given in which the low frequency limit gives very accurate answers from very soon after t_0 on. It appears that this good agreement is not general, however, but results from the particular way the source term used in Reference B-1 depends on the time.

As an illustration of the results of the calculations, we consider the particular set of parameters:

$$\begin{aligned}
\omega_g &= 1.049 \times 10^{-2} \text{ sec}^{-1} \\
\omega_A &= 1.068 \times 10^{-2} \text{ sec}^{-1} \\
T_o &= 100 \text{ sec} \\
z &= 2 \times 10^6 \text{ cm} \\
r &= 10^7 \text{ cm} \\
c &= 3 \times 10^4 \text{ cm/sec}
\end{aligned}$$

We choose the amplitude of the initial disturbance such that the amplitude of the N-wave arriving at the point (z,r) will be 1. In Figure B-2 we show the results for times later than 450 seconds after the source first became nonzero (the starting time for the plot was arbitrarily chosen; the result is, of course, nonzero from $t_o - T_o/2$ on). Plotted on the large graph are the results for setting ω_g and ω_A both equal to 1.049×10^{-2} and for the low frequency limit. The low frequency limit completely misses the early time structure of the result. This structure, which is substantial, might be important to considerations of detection or coupling to other atmospheric modes. The result of setting $\omega_A = \omega_g$ appears quite satisfactory in this particular case, being very close to the exact result at all times.

In Figure B-3, we show the results of the case of:

$$\begin{aligned}
\omega_g &= 8.25 \times 10^{-3} \text{ sec}^{-1} \\
\omega_A &= 8.75 \times 10^{-3} \text{ sec}^{-1} \\
T_o &= 19.4 \text{ sec} \\
z &= 2.25 \times 10^7 \text{ cm} \\
r &= 1.3 \times 10^7 \text{ cm} \\
c &= 4.3 \times 10^4 \text{ cm/sec}
\end{aligned}$$

We show the results for times later than 900 seconds; the earlier results are off the graph. The results are shown for the exact calculation and for $\omega_A = \omega_g = 8.25 \times 10^{-3} \text{ sec}^{-1}$. The results of the low frequency limit

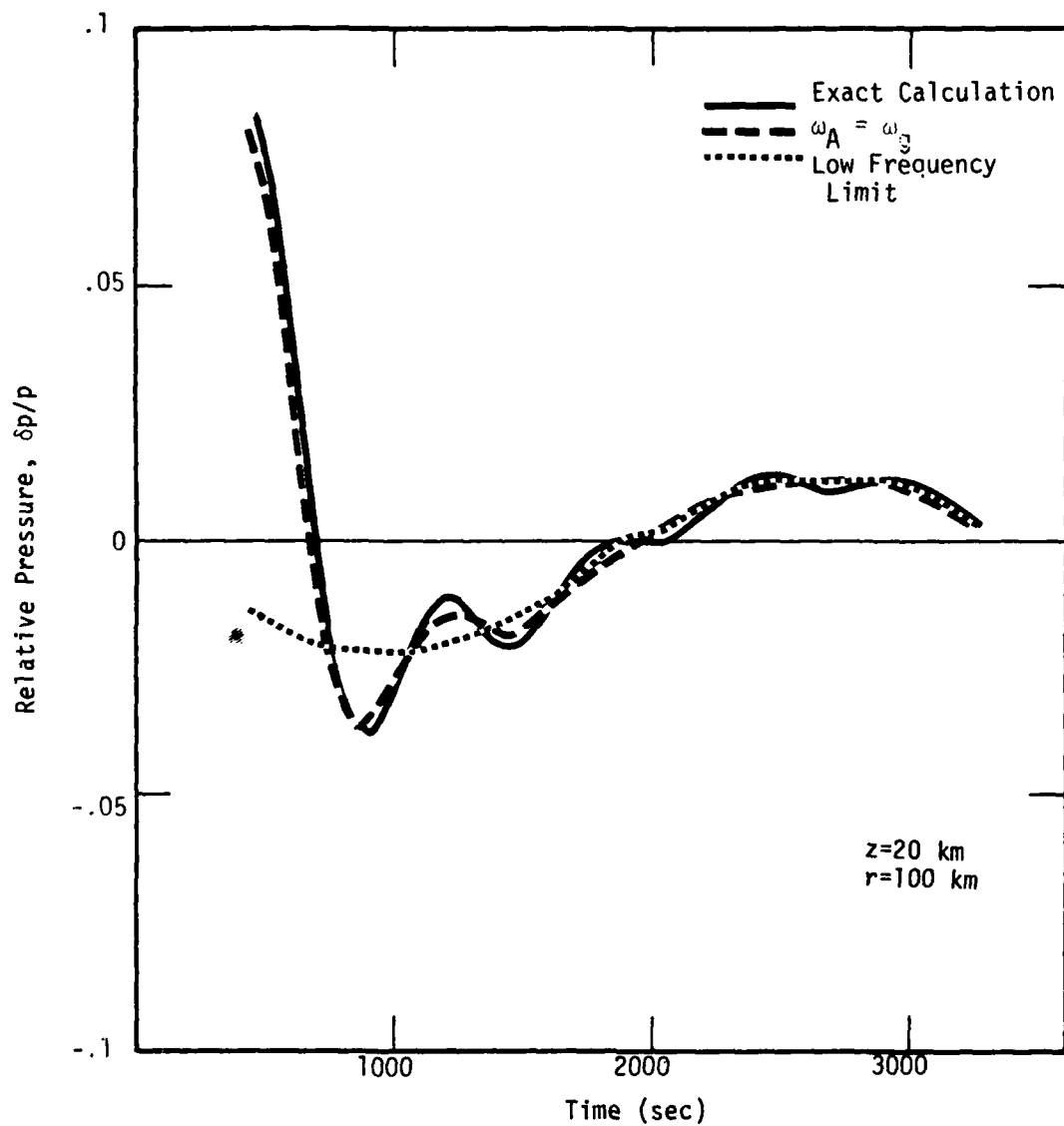


Figure B-2. A comparison of three methods of calculating the relative pressure (see text for parameters).

ATE
LMED
8